UNIVERSITEIT ANTWERPEN

Faculteit Wetenschappen

Departement Fysica

A Study of Charged Particle Production in Proton-Proton Collisions at LHC

Een Studie van de Productie van geladen Deeltjes in Proton-Proton Botsingen aan de LHC

Proefschift voorgelegd tot het behalen van de graad van doctor in de wetenschappen aan de Universiteit Antwerpen

Ph.D. Student:
Mohammed Attia Mahmoud

Promotor:
Prof. Albert De Roeck

A STUDY OF CHARGED PARTICLE PRODUCTION IN PROTON-PROTON COLLISIONS AT LHC

By

Mohammed Attia Mahmoud Mohammed
M.Sc of physics (2007)
Faculty of Science

Supervisions committee:

Internal Supervisors:

1. **Prof. Dr. Mohammed Nabil Yasein El-Bakry**
   Professor of Nuclear Physics, Faculty of Science, Helwan University, Cairo, Egypt
   Signature:
2. **Dr. Naglaa Rashed Sayed**
   Ass. professor of Nuclear Physics, Faculty of Science, Fayoum University,El-Fayoum, Egypt.
   Signature: Naglaa Rashed
3. **Dr. Amr Radi**
   Ass. professor of Physics, Faculty of Science, Ain Shams University, Cairo, Egypt.
   Signature: Amr M. Radi
4. **External Supervisor:**
   Prof. Dr. Albert De Roeck
   Physics senior at CERN, Geneva.
   Prof. Of physics, Antwerp University, Belgium.
   Prof. Of physics, IPPP, UK.
   Prof. Of physics, University of California, Davis, USA.
   Signature:

Head of Physics Department

Prof. Dr. Salah Mahrouss

Approval sheet

A STUDY OF CHARGED PARTICLE PRODUCTION IN PROTON-PROTON COLLISIONS AT LHC

By

Mohammed Attia Mahmoud Mohammed

This thesis for PhD degree in Physics has been Approved by:

Prof. Dr. Albert De Roeck
-Physics senior at CERN, Geneva.
-Prof. of physics, Antwerp University, Belgium.

Prof. Dr. Gabor Veres
-Convener of Heavy Ion group, CMS Experiment, CERN, Geneva, Switzerland.
-Eötvös Lorànd University, Budapest, Hungry.

Prof. Dr. Mohamed Nagdy
Prof. of Nuclear physics, Faculty of Science,
Helwan University, Cairo, Egypt.

Prof. Dr. Mohammed Nabil Yasein El-Bakry
Prof. of Nuclear physics, Faculty of Science,
Helwan University, Cairo, Egypt.

ACKNOWLEDGEMENTS

All gratefulness and deepest appreciation to "**ALLAH** ", for all gifts that given to me.

I warmest thanks are extended to Prof. Dr. Albert De Roeck, Professor of Physics, CERN, for his keen supervision, fruitful discussion and continuous encouragement and supporting me in all of my time in CERN .

I would like to express my deepest gratitude to Prof. Dr. Mohamed Nabil Yasein , Professor of Nuclear Physics, Physics Department, Faculty of Science, Fayoum University, for his supervision, and valuable support though out this study.

I would like to express my deepest gratitude to Dr. Naglaa Rashed, Associate Professor of Nuclear Physics, Faculty of science, Fayoum University, for here supervision, fruitful discussion and continuous encouragement.

I would like to express my deepest gratitude to Dr. Amr Radi, Associate Professor of Physics, Faculty of science, Ain Shams University, for here supervision, fruitful discussion and continuous encouragement.

I am deeply indebted to Dr. Gabor Veres (Research Staff in CERN, Geneva, Switzerland) who helped me in all stages in my work; he is helpful, kind and amazing person.

Thanks are also to all members of the Physics Department, Faculty of Science, Fayoum University, for their support throughout this work.

Specially, thanks are also to **my wife**, ***my parents, and my family*** for their encouragement.

Summary

Een studie van de productie van geladen deeltjes in proton-proton botsingen aan de LHC

De "Large Hadron Collider" (LHC) is de grootste and meest energetische proton-proton versneller in de wereld. De energy van deze versneller is 14 TeV maar de data die bestudeerd worden in deze thesis hebben een energie van 7 TeV. Deze versneller is gebouwd door de Europese Organizatie voor Nucleair Onderzoek in Geneve, Switzerland (CERN) over een periode van 10 jaar: van 1998 tot 2008. De LHC heeft vier grote detektoren die de deeltjes bestuderen die geproduceerd worden in deze proton-proton botsingen. Deze experimenten noemen: ATLAS, CMS, ALICE -- voor de studie van botsingen van zware ionen-- en LHCb -- voor de studie van processen belangrijk voor het begrijpen van anti-materie in het Universum--. De twee grootste experimenten, met de beste kansen voor het vinden van nieuwe deeltjes zijn ATLAS and CMS. Dit werk is gebaseerd op data genomen met het CMS (Compact Muon Solenoid) experiment, dat gelokaliseerd is in Cessy, Frankrijk.

In dit werk gaan we op zoek naar zogenaamde 'nieuwe fysica' in de study van zogenaamde minimum bias botsingen. Dit zijn de meest algemene van de proton-proton botsingen, met zeer minimale voorwaarden voor de triggering van het signaal. De trigger is een computercomponent van het experiment die on-line beslist of een botsing interessant is om uitgeschreven en opgeslagen te worden. Met dit sample van -meestal zeer zachte--

botsingen bestuderen we twee verschillende verschijnselen, waarbij we naar de productie van de geladen deeltjes kijken: geladen deeltjes vormen sporen in the centrale sporenkamer van CMS.

1. De study van de maximale spoor-dichtheid in een botsing, ie de dichtheid van geladen deeltjes die in de botsingen geproduceerd worden, in de zogenaamde pseudo-rapiditeit ruimte (pseudo-rapiditeit is een transformatie van de polaire hoek van het deeltje ten opzichte van de bundel richting), in intervallen van 0.1, 0.2 en 0.5 eenheden van pseudo-rapiditeit. Deze resultaten van CMS/LHC worden vergeleken met gegevens van vroegere experimenten bij lagere energieen.

2. De studie van de verhouding van geproduceerde kaon deeltjes -- dit zijn deeltjes die de quark met de eigenschap 'vreemdheid' bevatten-- en pion deeltjes, als functie van de totale deeltjes multipliciteit van de botsing. Hier wordt ook de verbinding besproken met gelijkaardige meetingen in botsingen met zware ionen.

De thesis bevat vijf hoofdstukken: Het eerste hoofdstuk geeft een theoretische inleiding tot het onderwerp, inclusief het zogenaamde Standard Model dat de basis vormt voor het zoeken naar nieuwe verschijnselen. We gaan ook dieper in op de fenomenologie van de korrelaties tussen deeltjes geproduceerd in proton-proton botsingen, en het concept van een nieuwe toestand van de materie die geproduceerd kan worden in botsingen met zware ionen, het zognaamde quark-gluon plasma.

Het tweede hoofdstuk bevat gedetailleerde informatie over de versneller LHC. Het CMS experiment en de sub-detektoren van dit experiment worden evenals in detail beschreven in dit hoofdstuk. Hoofdstuk drie beschrijft de data bestanden die gebruikt werden voor de studie in deze thesis en beschrijven een gedetailleerde studie van de triggers die gebruikt werden om deze data bestanden op te bouwen. Verder worden ook de Monte Carlo programma's voor proton-proton botsingen besproken, die gebruikt worden voor gedetailleerde simulaties van botsingen in de CMS detektor, waarmee de data vergeleken zal worden. De selecties van de botsingen wordt beschreven evenals de selectie van de sporen in de sporenkamer, die gebruikt worden in deze analyse.

Hoofdstuk vier beschrijft de analyse van de maximale deeltjes dichtheid in de proton-proton botsingen. Resultaten worden getoond voor verschillende keuzes van het interval in pseudo-rapiditeit en andere variabelen. De data volgt een exponentieel afvallende funktie voor stijgende spoor-densiteit. In detail is deze funktie verschillend van diegene die voorspeld wordt door de Monte Carlo programma's die we voor proton-proton botsingen ter beschikking hebben. Speciale aandacht gaat naar de uiteinden van de verdeling, voor de hoogste waarden van de spoor densiteit, waar we eventueel botsingen zouden kunnen vinden met een zeer hoge abnormaly dichtheid. Helaas hebben we geen zulke botsingen gevonden in onze data, en hebben we dus ook geen evidentie voor nieuwe fysica in deze analyse gevonden.

ABSTRACT

Large Hadron Collider (LHC) is the world's largest and highest-energy particle accelerator. It was built by the European Organization for Nuclear Research (CERN) over a ten year period from 1998 to 2008. LHC has four detectors to study the particles produced from the collision. ATLAS, CMS, ALICE (study of heavy ions), and LHCb (study of antimatter). The two biggest experiments are ATLAS and CMS. This work is based on CMS experiment. CMS is the general propose experiment, and it is located in Cassy, France.

The aim of this work is searching of new physics by the different methods:

1- Study the maximum track density per event inside small windows with width 0.1, 0.2, and 0.5 with respect to pseudorapidity and rapidity, and making comparison between the present work and previous work in different experiment.

2- Study the relation between multiplicity and kaon/pion ratio. The aim of this point is trying make connection between hadron-hadron collision and heavy ions collisions.

This thesis consists of five chapters; the first chapter is related to some theoretical concepts for standard model of particles, the correlation of track density, and the quark gluon plasma and how we can search about it.

The second chapter contains some information about LHC and its experiments. Compact Muon Solenoid (CMS) is studied

in some details and its subdetectors. Chapter three is concerning to the dataset, MC, some information about triggers were used in the present work, Events selections, and Track selections.

Chapter four is concerning to the study of maximum track density. We gave review about the previous work in that point in some details in the first section. After that, we showed the results, unfolding and systematic errors. The studying the kaon to pion ratio is presented in last chapter, chapter 5 also with some historical review for this work in heavy ions and hadron-hadron collisions.

Contents

Contents

Chapter 2

LHC and CMS Experiment

Chapter 3

Dataset, MC, Events and track selections

Chapter 4

Maximum Track Density

Chapter 5

Kaon to pion ratio

List of figures

List of Figures

List of tables

List of tables

Chapter 1

Theoretical Aspects

(1.1) Introduction:

What is the matter made of? This is the important and basic question in particle physics. From the beginning of the mankind, the man searches the answer of that question. Democritus in the fifth century B.C proposed that everything is composed from individual particles called “atoms”. In the early of 19th century John Dalton formulated his atomic theory, it stated that the elements consisted of tiny particles called atoms and all atoms of an element were identical and that in particular they had the same mass. J.J. Thompson discovered the electron in his research on cathode rays, an entirely new field of physics was born. His interpretation of these findings led to the plum pudding model, which proclaimed atoms to consist of positively charged matter, in which the negatively charged electrons are embedded.

In 1909**,** Hans Geiger and Ernest Marsden under the direction of Ernest Rutherford at the Physical Laboratories of the University of Manchester, preformed one of the famous experiments named the Geiger–Marsden experiment (also called the Gold foil experiment or the Rutherford experiment). This experiment disproved plum pudding model. When he exposed a thin gold foil to alpha rays from a radioactive source, he discovered that many of the alpha particles could traverse the foil without any distraction, while some were scattered even backwards. Analyzing the angular distribution of the outgoing particles, Rutherford concluded that the atom consists of point mass with positive charge and electrons with negative charge move around it.

In 1932, James Chadwick discovered the neutron, a neutral particles with a mass is similar to proton. Otto Hahn, Lise Meitner and Fritz Strassmann showed the result of the first experiment of nuclear fission. In 1950s, the improvement of particle accelerators and particles detectors allowed scientists to study matter at high energies.

The Standard model of particle physics was developed to explain the properties of sub-atomic particles and the forces that govern their interactions. Sheldon Glashow, 1960, put the first step towards the Standard Model by combining the electromagnetic and weak interactions. 1967, Steven Weinberg and Abdus Salam incorporated the Higgs mechanism into Glashow's electroweak theory, giving it its modern form. The predictions of the Standard Model have been tested with many precise measurements. In 1983, the W and Z bosons were discovered at CERN, also their masses were found as predicted in Standard Model. The first observation for gluons was in 1979 at DESY, Hamburg. In 1995 in FermiLab, the top quark was discovered.

(1-2) Standard Model of Particle Physics:

The Standard Model of Particle Physics is currently the best description of fundamental interactions and one of the most precisely tested theories in all of science. The Standard Model is a combination of quantum field theories that describe the observed fundamental particles and their interactions. The gauge symmetry group of the SM is the

$$SU(3)\times SU(2)\times SU(1) \tag{1.1}$$

group in which the SU(3) is the group of strong interaction described by the QCD and SU(2) ×U(1) is the group of electroweak interaction described by Electroweak Theory.

There are four forces in nature; strong force, this force is responsible for the interaction between hadrons and is the source of nuclear power; weak force which governs the transition from one quark flavor to another and the interaction between neutrinos and other elementary particles; the electromagnetic force is the force that occur between electrically charged particles; finally the gravitational force, the weakest of the four interactions, which is responsible for falling the things like apple, also this force is not described in Standard Model.

According to the Standard model, the building blocks of matter are point-like particles, which carry a spin of 1/2. They are usually grouped into three families; each family consists of two quarks and two leptons. The properties of these elementary particles are summarized in Table (1.1). For each particle, there is an associated antiparticle with the same mass but opposite quantum numbers. Quarks have fractional electric charge values — either 1/3 or 2/3 times the elementary charge, depending on flavor, as show in table 1.1. Quarks carry "color charges", which means that quarks also participate in the strong interaction. Color charges are the strong interaction version of charges, which have no relation to the real colors of daily life. There are three color charges, usually denoted by blue (B), red (R) and green (G). Experimentally, all particle states observed in nature are "colorless" or "white". This is called the color confinement. The quarks cannot appear freely and have to group together in the form of hadrons, which are colorless. Hadrons are divided into two categories, fist one is known as Baryons, which consist of three quarks such as proton and neutron. The colors of the quarks inside a baryon are RGB (R + G + B = white), the second one is known as mesons, these mesons consist of two quarks (quark and antiquark) The colors of the quarks inside a meson are $B\overline{B}$, $R\overline{R}$, or $G\overline{G}$ also the net color in mesons will be white because color and anticolor.

The forces between particles arise from the exchange of other particles, called force carriers or mediator. These types of particles are called bosons. The forces and the mediators are summarized in Table. 1.2. The strong force between hadrons is mediated by gluons, which is described by Quantum Chromodynamics (QCD). The photons are responsible for the electromagnetic interaction between charged particles, which is formulated as Quantum Electrodynamics (QED). The weak interactions, mediated by the $W^{\pm}$ or Z^{0} bosons, are described by the electroweak theory. The graviton is thought to be mediating the force of gravitation.

Before the Higgs mechanism was implemented into the Standard Model all force mediating-particles had to be massless. The problem with this old concept is that W and Z bosons of the weak interaction indeed have masses of m_W = 80.399 ± 0.023 GeV and m_Z = 91.1876 ± 0.0021 GeV [1]. To solve this problem, Peter Higgs proposed a mechanism that leaves the concept of local gauge invariance untouched by introducing a new gauge

Generation	Quarks				Leptons			
	Name	*Symbol*	*Charge*	*Mass*	*Name*	*Symbol*	*Charge*	*Mass*
First	Up Down	u d	+2/3 -1/3	1.5 - 4.5 MeV 5.0 - 8.5 MeV	Electron Electron neutrino	e^- υ_e	-1 0	0.511 MeV $2\text{x}10^{-6}$ MeV
Second	Charm Strange	c s	+2/3 -1/3	1.0 – 1.4 GeV 80 – 155 MeV	Muon Muon neutrino	$\mu -$ υ_μ	-1 0	105.7 MeV <0.19 MeV
Third	Top Bottom	t b	+2/3 -1/3	174.3 ± 5.1 GeV 4.0 – 4.5 MeV	Tau Tau neutrino	e^- υ_τ	-1 0	1777 MeV <18.2 MeV

Table 1.1: The properties of quarks and leptons. [1]

	Strong	Electromagnetic	Weak	Gravitational
Mediator	Gluon (g)	Photon (γ)	$W\pm, Z$	Graviton
Spin-parity	1^-	1^-	1^- , 1^+	2^+
Range [m]	10^{-15}	∞	10^{-18}	∞
Relative Strength	1	10^{-2}	10^{-13}	10^{-38}

Table 1.2: The fundamental forces carriers and properties

symmetry breaking mechanism, called after its inventor Higgs mechanism. With this new mechanism masses can be assigned to all elementary particles that actually have a mass, especially to the W and Z boson for which it was not possible before. This mechanism introduces a new measurable particle, the Higgs boson, which is the only particle of the Standard Model that has not been discovered yet. Nevertheless, precision measurements of the Standard Model indicate its existence with a mass m_h most probably in the range of 115 GeV < m_h < 158 GeV. Higgs was (basically) discovered on July 4, 2012. Its mass is around 125 GeV.

(1.3) Hadrons: Mesons and Baryons

Hadrons are strongly interacting particles which are composed of quarks. Their constituents, together with gluons and sea quarks (virtual quark-anti-quark pairs) are called partons. There are two types of hadrons, namely baryons and mesons which are distinguishable by their so-called baryon quantum number, B. Compounds of three quarks carry a baryon number of 1 and are simply called baryons whereas compounds of one quark and one anti-quark are denoted as mesons with a baryon number of 0. There are some theories which predict compounds of more than three quarks, e.g. so-called penta-quarks, which are not discussed here. Since mesons consist of an even number of elementary fermions they act as bosons on particle level, whereas baryons act as fermions. The discovery of the Δ^{++} resonance, which is a baryon composed of three up quarks in the same state, required the introduction of a further quantum number, otherwise the Pauli exclusion principle would have been violated. This quantum number is called color charge with the three possible values red, green and blue and their corresponding anti-colors. Each observed particle provides a neutral color charge which can only be achieved by e.g. three particles of different colors or a particle and an anti-particle with color and anti-color, respectively. The fact that no isolated quarks are allowed is denoted as confinement of color charged particles. Gluons, as mediators of the strong interaction, are color charged particles as well.

(1.4) Quantum ChromoDynamics:

Quantum Chromodynamics (QCD) [2, 3], is the theory of strong interactions that describes the interaction of colored quarks and gluons. The QCD theory is a non-Abelian gauge theory of SU (3) symmetry group. Quarks carry a color charge (red, blue or green) and antiquarks have anti-color. Gluons exchanged between quarks hold the quarks together. The gluons interact themselves, unlike the photons or the vector bosons of weak interaction. It makes the QCD theory very different from Electroweak theory which has the symmetry of the SU(2) ×U(1) gauge group.

(1.4.1) The QCD Lagrangian and the Running Coupling:

A theory of the properties of quarks and their interaction has to be able to describe and contain the following features that have just been discussed [4]:

Hadrons are composed of quarks with fractional charges.

- Quarks are spin-1/2 fermions.
- They carry one of three possible color charges.
- There is evidence that color charges exhibit an SU(3) symmetry.
- Quarks are subject to a strong interaction.
- Besides quarks, additional partons are contained in hadrons.
- Those partons do not interact via the electro-magnetic or weak force.

The mathematical description of quantum chromodynamics relies on similar principles as the electro-weak theory. The QCD Lagrangian can be written with implied summation over repeated indices as

$$L_{QCD} = \sum_q \bar{q}_i \left(i\gamma^\mu D_\mu - m_q\right)_{ij} q_j - \frac{1}{2} F^a_{\mu\nu} F^{\mu\nu} \tag{1.2}$$

The quark field $q_i$are in the triplet representation of the colored group, (i = 1, 2, 3) and D is the covariant derivative.

The tensor of field strength and the covariant derivatives are given by:

$$F^a_{\mu\nu} = \partial_\mu A^a_\nu - \partial_\nu A^a_\mu - g f^{abc} A^b_\mu A^c_\nu \tag{1.3}$$

$$\left(D_\mu\right)_{ij} = \delta_{ij}\partial_\mu + i g_s T^a_{ij} A^a_\mu \tag{1.4}$$

$$\left(m_q\right)_{ij} = m_q \delta_{ij} \tag{1.5}$$

Where, the indices *a*, *b*, and *c* run over the eight color degrees of freedom of the gluon field, A_{μ}^{a} are the gluon fields, g_s the gauge coupling, $f^{abc}(a, b, c = 1, 2, \dots .8)$ is the structure constant, and T_{ij}^{a} is the generators of the Lie group. From the expression of the gluon field and completely anti-symmetric structure constant f^{abc}, the nonabelian gluon-gluon interactions become calculable.

A coupling constant determines the strength of an interaction. As in the case of Quantum Electrodynamics (QED), strong coupling constant is defined as following.

$$\alpha_s = \frac{g_s^2}{4\pi} \qquad (1.6)$$

The only other free parameters in the Lagrangian are the fermions masses. Taking into account the SU (3) nature of QCD, the eight generators of the symmetry transformation can be expressed using the Gell-Mann matrices that can be found elsewhere [4]. From the couplings it becomes apparent that only three kinds of basic QCD processes are observable along with the propagators of free quarks and gluons: Gluon radiation from a quark and three as well as four gluon vertices. The Feynman graphs of these processes are shown in figure (1-1).

Gluon self-coupling accounts for potential energy build-up, when the quarks are separated. Between the quark pair, a gluon string is formed, which breaks apart once enough energy is stored to create a new quark-antiquark pair at the rupture. This explains the absence of free colored particles in nature. The break-up happens at distances of about 1 fm, which is about the

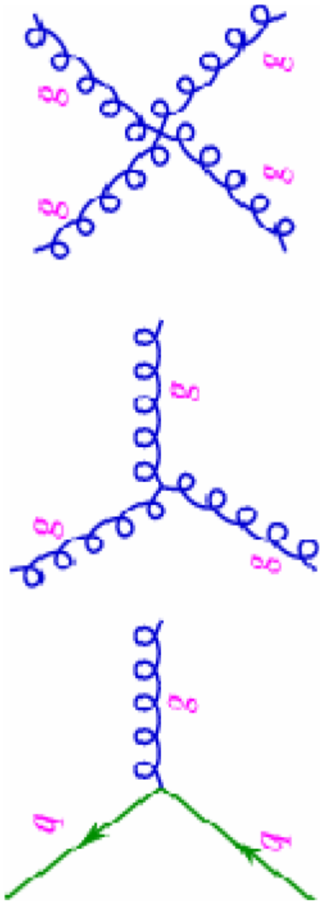

Figure (1-1): Feynman graphs of the basic QCD interactions size of a proton, explaining the short range of the strong interaction despite its massless force carriers. The observation that rather than extracting partons from a proton, one destroys the proton in scattering experiments and creates new particles is called color confinement. On the other hand, when the momentum transfer Q^2 is large enough in collider experiments, quarks can be assumed as quasi-free particles, a principle that is called *asymptotic freedom* [5] and is successfully applied in theory calculations, since it allows the application of perturbative techniques.

In contrast to electromagnetic interactions, where screening effects lead to an increasing coupling for small distances and growing energies, asymptotic freedom can be interpreted as anti-screening In the low energy regime, the coupling diverges which makes it impossible to calculate low-Q2 QCD in the mathematical framework of perturbation theory. In order to deal with divergent terms that arise from gluon self-coupling, renormalization techniques have to be applied, that absorb the problematic terms. It is however necessary to restore gauge invariance by rescaling all involved fields.

(1.5) Track Density correlations:

In the recent years, some of remarkably intense experimental and theoretical activity in search of scale invariance and fractality in multi-hadron production processes, this called “intermittency”. These studies cover all types of reactions ranging from e^+e^- annihilation to nucleus-nucleus collisions, up to the highest attainable energies. The creation of soft hadrons in these processes, a major fraction of the total cross section, relates to the strong-coupling long- distance regime of Quantum Chromodynamics (QCD), at present one of the least explored sectors in the whole of high-energy particle physics.

History shows that studies of fluctuations have often triggered important advances in physics. In the present context, it was the observation of "unusually large" particle density fluctuations, reminiscent of intermittency spikes in spatio-temporal turbulence, which prompted the pioneering suggestion to investigate the pattern of multiplicity fluctuations in multihadron events for ever decreasing domains of phase space. Scale-invariance or fractality would manifest itself in power-law behavior for scaled factorial moments of the multiplicity distribution in such domains. It is important to stress here that, in practice, one deals with the problem of evolution of particle number distributions for ever smaller bins and intermittent behavior implies that, for small phase-space bins, the distributions become wider in a specific way. The same problem can be stated as an increasing role of correlations within a small phase-space volume.

(1.5.1) Correlations for particles of different species

Considering two particle species a and b, the two-particle pseudorapidity correlation function is of the form:

$$C_2^{ab}(\eta_1,\eta_2) = \rho_2^{ab}(\eta_1,\eta_2) - f\rho_1^{a}(\eta_1)\rho_1^{b}(\eta_2) \tag{1.7}$$

Where

$$\rho_1^a(\eta_1) = \frac{1}{\sigma_{inel}} \frac{d\sigma^a}{d\eta_1}; \qquad (1.8)$$

$$\rho_2^{ab}(\eta_1, \eta_2) = \frac{1}{\sigma_{inel}} \frac{d\sigma^{ab}}{d\eta_1 d\eta_2} \qquad (1.9)$$

η_1 and η_2 are the c.m. pseudorapidity, σ_{inel} the inelastic cross section and a, b represent particle properties, e.g. charge.

The normalization conditions are

$$\int \rho_1^a(\eta_1) d\eta_1 = \langle n_a \rangle; \; \iint \rho_2^{ab}(\eta_1, \eta_2) d\eta_1 d\eta_2 = \langle n_a(n_b - \delta^{ab}) \rangle,$$

$$(1.10)$$

$$\iint C_2^{ab}(\eta_1, \eta_2) d\eta_1 d\eta_2 = \langle n_a(n_b - \delta^{ab}) \rangle - f \langle n_a \rangle \langle n_b \rangle$$

$$(1.11)$$

Where $\delta^{ab} = 0$ for the case when a and b are particles of different species and $\delta^{ab} = 1$ for identical, and n_a and n_b are the corresponding particle multiplicities.

Most experiments use

$$f = 1 \qquad (1.12)$$

so that the integral over the correlation function (equal to the ratio $\bar{n}^2/k$ of the negative binomial parameters [6]) vanishes for the case of a Poissonian multiplicity distribution. Other experiments use

$$f = \langle n_a(n_b - \delta^{ab}) \rangle / \langle n_a \rangle \langle n_b \rangle \qquad (1.13)$$

to obtain a vanishing integral also for a non-Poissonian multiplicity distribution.

To be able to compare the various experiments, E.A. De Wolf, I.M. Dreminb, W. Kittel used [7] both definitions and denote the correlation function $C_2^{ab}(\eta_1,\eta_2)$ when following definition (1.12) and $\acute{C}_2^{ab}(\eta_1,\eta_2)$ when following definition (1.13). We, furthermore, use a reduced form of definition (1.13),

$$\hat{C}_2^{ab}(\eta_1,\eta_2) = \acute{C}_2^{ab}(\eta_1,\eta_2)/\langle n_a(n_b - \delta^{ab})\rangle \qquad (1.14)$$

The corresponding normalized correlation functions

$$K_2^{ab}(\eta_1,\eta_2) = C_2^{ab}(\eta_1,\eta_2)/\rho_1^a(\eta_1)\rho_1^b(\eta_2) \qquad (1.15)$$

follow the relations

$$\acute{K}_2 = \left(\frac{1}{f}\right)\ (K_2 + 1) - 1, \qquad (1.16)$$

And $\widetilde{K}_2$ is defined as $\widetilde{K}_2 = \acute{K}_2$. These are more appropriate than C_2 when comparisons have to be performed at different average multiplicity and are less sensitive to acceptance problems.

The relation between inclusive and semi-inclusive correlation functions has been carefully analysed in [8]. Let σ_n be the topological cross section and

$$P_n = \sigma_n / \sum \sigma_n \qquad (1.17)$$

The semi-inclusive rapidity single- and two-particle densities for particles a and b are defined as

$$\rho_1^{(n)}(\eta_1) = \frac{1}{\sigma_n}\frac{d\sigma_n^a}{d\eta} \quad and \quad \rho_2^{(n)}(\eta_1,\eta_2) = \frac{1}{\sigma_n}\frac{d\sigma_n^{ab}}{d\eta_1 d\eta_2} \qquad (1.18)$$

The inclusive correlation function $C_2(\eta_1,\eta_2)$ can then be written as

$$C_2(\eta_1,\eta_2) = C_S(\eta_1,\eta_2) + C_L(\eta_1,\eta_2) \qquad (1.19)$$

where

$$C_S(\eta_1, \eta_2) = \sum P_n C_2^{(n)}(\eta_1, \eta_2), \tag{1.20}$$

$$C_L(\eta_1, \eta_2) = \sum P_n \, \Delta\rho^{(n)}(\eta_1) \, \Delta\rho^{(n)}(\eta_2) \tag{1.21}$$

With $C_2^{(n)}(\eta_1, \eta_2) = \rho_2^{(n)}(\eta_1, \eta_2) - \rho_1^{(n)}(\eta_1) \, \rho_1^{(n)}(\eta_2)$ and $\Delta\rho^{(n)}(\eta_1) = \rho_1^{(n)}(\eta) - \rho_1(\eta)$. In (1.20) C_s is the average of the semi-inclusive correlation functions (often misleadingly denoted as "short-range") and is more sensitive to dynamical correlations. The term C_L (misleadingly called "long-range") arises from mixing different topological single-particle densities.

A normalized form of C_s can be defined as

$$K_S(\eta_1, \eta_2) = \frac{C_S(\eta_1, \eta_2)}{\sum_n P_n \, \rho_1^{(n)}(\eta_1) \, \rho_1^{(n)}(\eta_2)}$$

$$= \frac{\sum_n P_n \rho_2^{(n)}(\eta_1, \eta_2)}{\sum_n P_n \rho_1^{(n)}(\eta_1) \, \rho_1^{(n)}(\eta_2)} - 1 \tag{1.22}$$

$\acute{C}_S$ and $\tilde{C}_S$ and their normalized forms $\acute{K}_2$ and $\tilde{K}_S$ are defined accordingly, with average $\langle n \rangle$ and $\langle n_a(n_b - \delta^{ab}) \rangle$ replaced by $n_a(n_b - \delta^{ab})$, respectively.

(1.5.2) Rapidity Correlations

The study of correlation effects in particle production processes provides information on hadronic production dynamics beyond that obtained from single-particle inclusive spectra. Correlations in rapidity *y* have been studied in various experiments on e^+e^-, lepton-nucleon, hadron-hadron, hadron-nucleus and nucleus-nucleus collisions. Strong rapidity (y) correlations have been observed in all experiments in one form or another, depending on the specific form of the correlation function, type of interaction, kind of particles, the kinematic region under consideration, etc. The key conclusions were (for early reviews see [10-11] :

1. Two-particle correlations are strong at small interparticle rapidity distances $|y_1 - y_2|$ (see Figure (1-2)).
2. They strongly depend on the two-particle charge combination.

Rapidity correlations are now being studied with renewed attention. One reason is that their structure at very small rapidity distances is directly related to self-similar particle-density fluctuations (intermittency).

(1.5.3) Correlations in hadron-hadron collisions

In Figure (1-3) the pseudo-rapidity correlation function $C_2(\eta_1, \eta_2)$ is given for η_1 = 0, as a f unction of $\eta_1 = \eta$, for the energy range between 63 and 900 GeV [12]. Whereas $C_2(0, \eta)$ depends on energy, the short-range correlation Cs defined in (2.36) does not strongly depend on energy and has a full width of about 2 units in pseudo-rapidity. The function CL is not a two-particle correlation, but derives from the difference in the single-particle distribution function for different multiplicities. As can be seen in Fig. (1-3) b, CL is considerably wider than Cs and increases with energy (the 63 GeV data are from [13]).

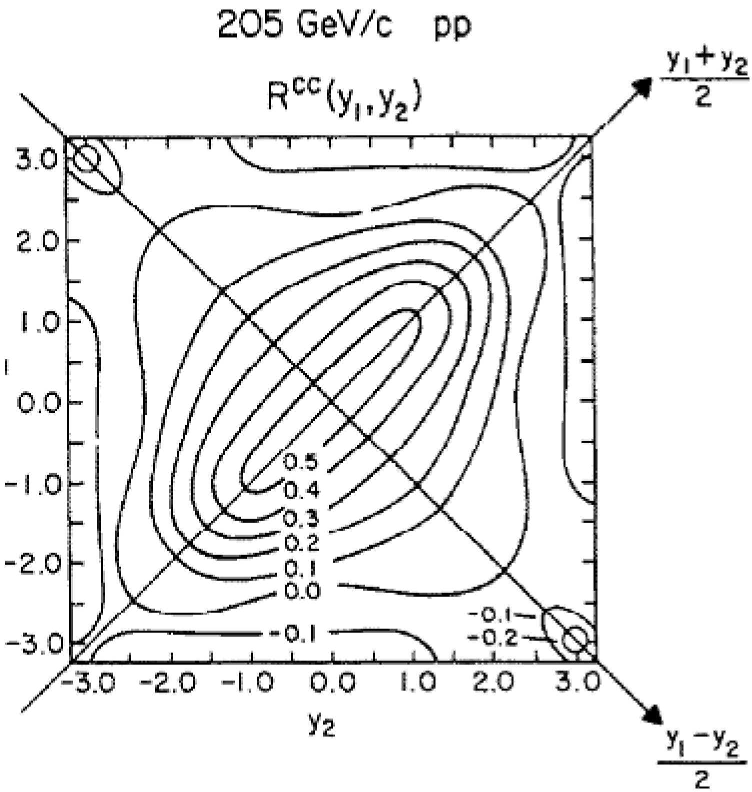

Figure (1-2): Contours of the two-particle correlation function, $R^{cc}(y_1, y_2)$, from 205 GeV/c pp interactions [9].

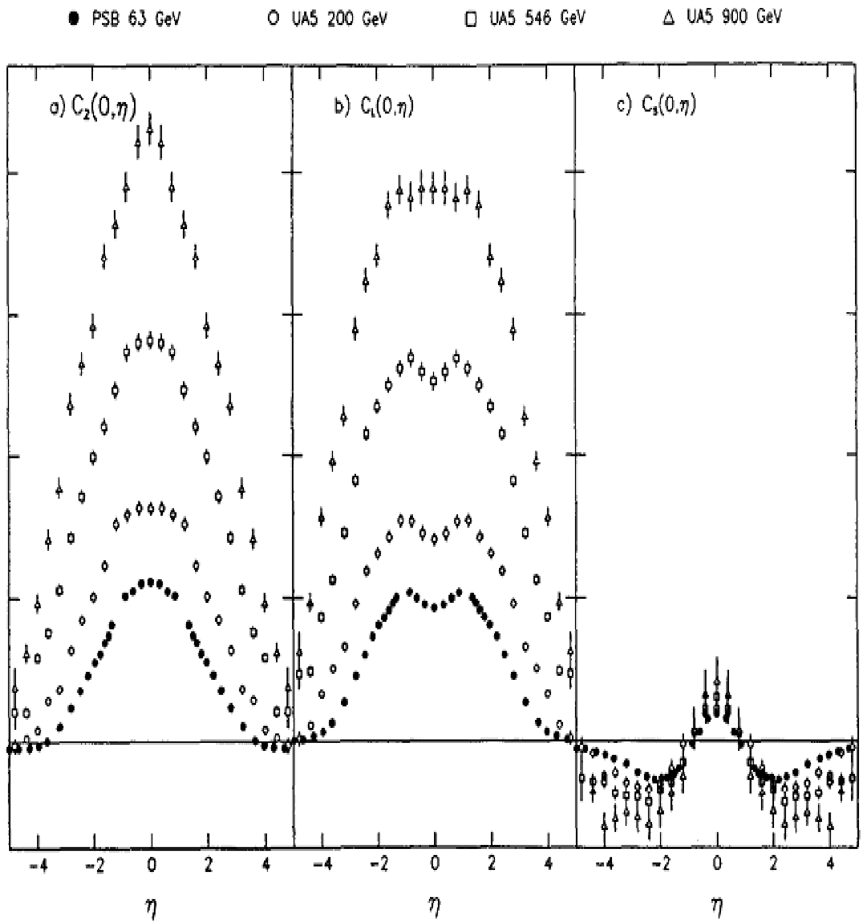

Figure (1-3): (a) The charge correlation function $C_2(\eta_1,\eta_2)$ plotted for $p\bar{p}$ collisions at fixed $\eta_1 = 0$ versus η_1 at 63,200,546 and 900 GeV, (b) the "long-range" contribution C_L and (c) the short-range contribution C_s [12].

In Figure (1-4), the semi-inclusive correlation $C_2^{(n)}(\eta_1, \eta_2)$ for pp collisions at 900 GeV [14] is compared to the UA5 Cluster Monte Carlo (MC) GENCL [15], as well as to the FRITIOF 2 [16] and PYTHIA [17] Monte Carlos, for charge multiplicity $34 \leq n \leq 38$. The Cluster MC is designed to fit just these short-range correlations, but also FRITIOF 2 is doing surprisingly well.

At lower energy, the NA23 Collaboration [18] has studied the short-range correlation of charged particles in pp collisions of $\sqrt{s}$ = 26 GeV in terms of $K_2(y_1, y_2)$ defined in (1.15). Only events with charge multiplicity n >6 are used. The positive short-range correlations are in agreement with those found earlier at $\sqrt{s}$ = 53 GeV [19].

The NA23 data are compared to single-string LUND [20] and to a two-chain Dual-Parton Model (DPM) [21] in Figure (1-5). The one-string model (without gluon radiation) does not at all describe the short-range rapidity correlation in the data. The two-chain model does better, but remains unsatisfactory. Somewhat better but still insufficient agreement is obtained by renormalizing the MC events to the experimental multiplicity distribution (not shown). The effect of Bose-Einstein correlations in the (+ +) and (- -) data is found to be insignificant, as may be expected for data integrated over transverse momentum p_T and azimuthal angle φ. Obviously, more chains, possibly with higher p_T, are needed to explain short-range order with fragmentation models, even below $\sqrt{s} \approx 30$ GeV.

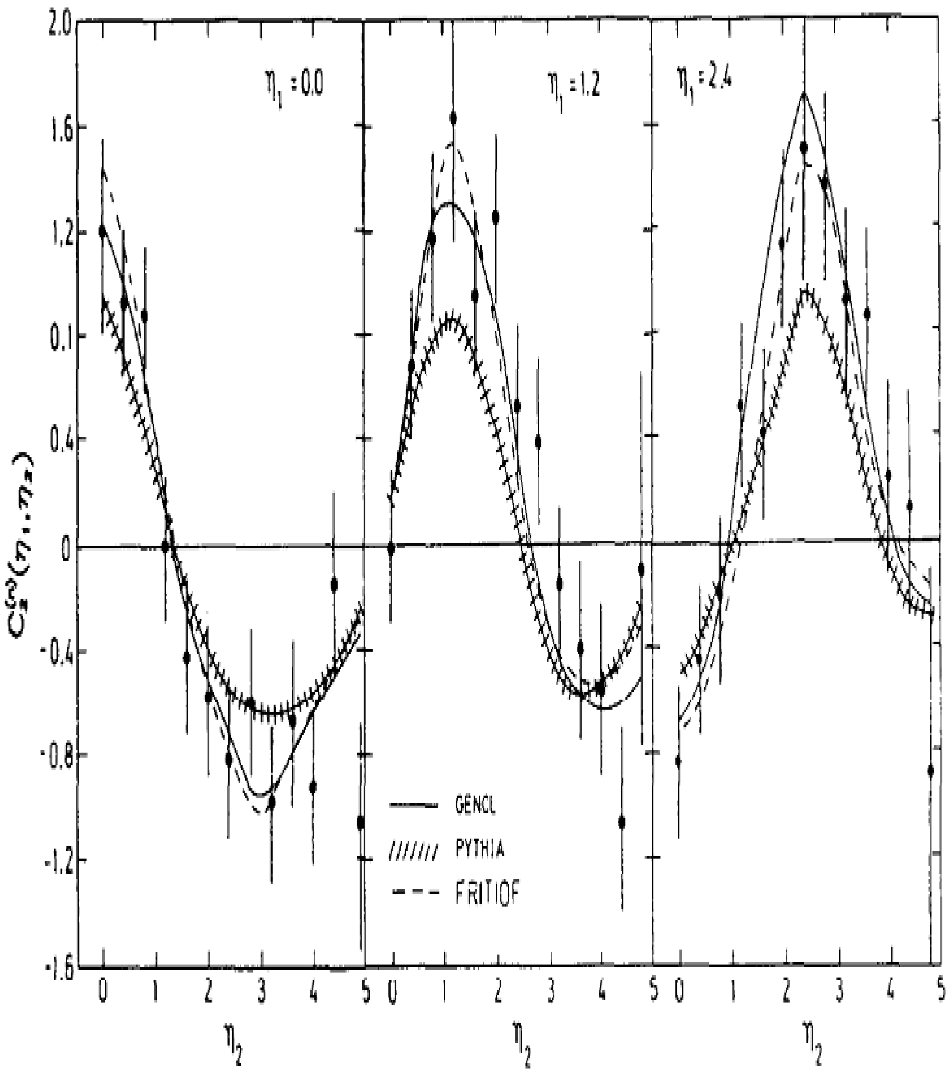

Figure (1-4): The semi-inclusive correlation function $C_2^{(n)}(\eta_1, \eta_2)$ for 34 < n < 38 $p\bar{p}$ collisions at 900 GeV, compared to the UA5 Cluster MC, PYTHIA and FRITIOF 2.0 [14].

NA22 results for $C_2(0, y_2)$ and $\tilde{C}_2(0, y_2)$ (Eqs. (2.25) and (2.30)) for π^+p and K^+p collisions at $\sqrt{s}$= 22 GeV [22] are compared with FRITIOF 2, a two-string DPM and QGSM [23] predictions in Fig. (1-5) a and b. FRITIOF and two-string DPM largely underestimate the correlation. QGSM reproduces $C_2^{--}(0, y_2)$ very well and even overestimates $C_2^{++}(0, y_2)$ and $C_2^{+-}(0, y_2)$. It has been verified that the differences between QGSM and FRITIOF or DPM are not due to the different treatment of tensor mesons.

In Figure (1-5) c, FRITIOF and QGSM are compared to the NA22 data in terms of the short-range contribution $\tilde{C}_2(0, y_2)$. The (+ -) short-range correlation is reproduced reasonably well by these models. For equal charges, however, the strong anti-correlation predicted by FRITIOF is not seen in the data. QGSM contains a small equal-charge correlation due to a cluster component, but still underestimates its size. Similar discrepancies are also observed in semi-inclusive (fixed multiplicity) data for each charge combination (not shown here). They are even larger than in the inclusive data, also in the QGSM model.

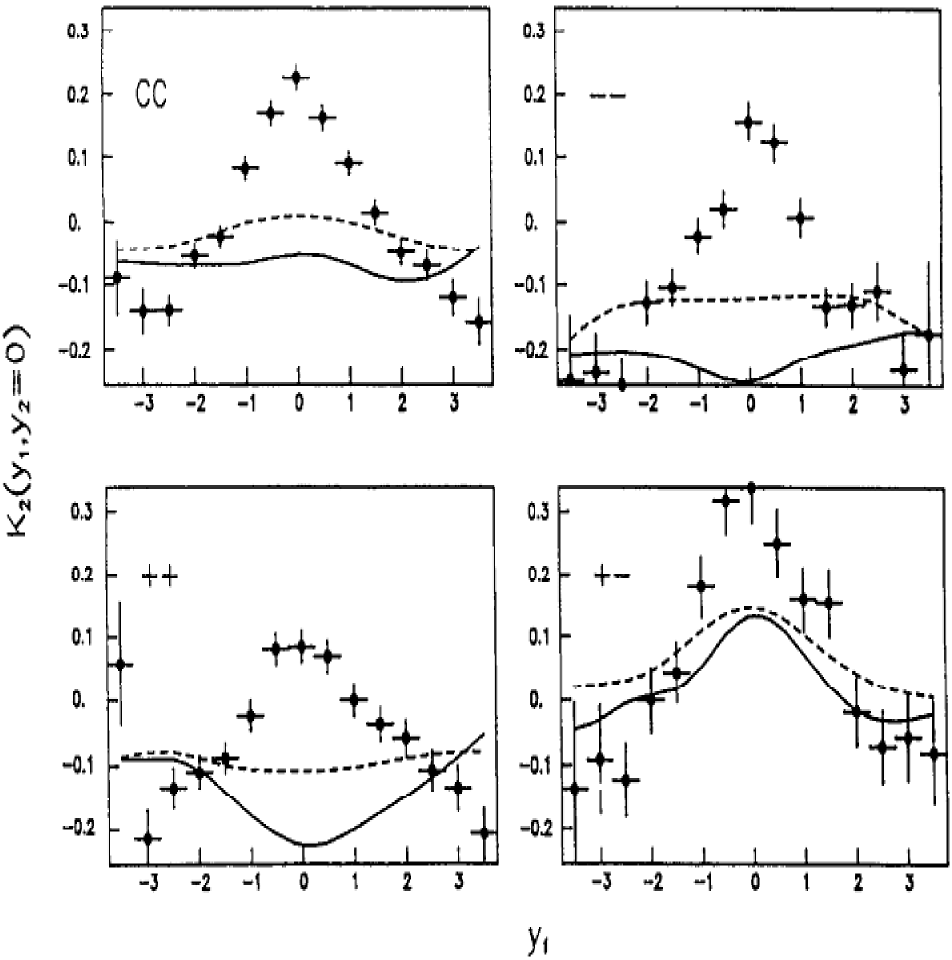

Figure (1-5): Normalized correlation function $K_2(y_1, y_2 = 0)$ for (CC), (- -), (+ +) and (+ -) combinations in n > 6 pp collisions at 360 GeV/c, compared to predictions from single chain LUND and a two-chain DPM [18].

(1-6) Phase Transition in QCD

According to the Big Bang cosmological theory, a few microseconds after the Big Bang the early Universe was very hot plasma of deconfined quarks and gluons. It evolved to its present state rapidly expanding and cooling, traversing a series of phase transitions predicted by the Standard Model. In these transitions, quarks and gluons became confined and the global features of our Universe, like the baryon asymmetry and the galaxy distribution, were originated. Today, the deconfined quarks and gluons are likely present in the core of the neutron stars, even if at lower temperature and higher density than in the early Universe. The main task of the relativistic heavy-ion experiments is to generate the deconfined phase colliding heavy ions at very high energy.

For understanding how the new phase forms, we can consider at first this picture, shown in Figure (1-6): composite nucleons with a finite spatial extension and made up of point-like quarks, if compressed, start to overlap above a critical density until each quark eventually finds within its immediate vicinity a considerable number of other quarks. It has no way to identify which of these had been its partners in a specific nucleon in the previous state at lower density. Therefore beyond a certain condition of high density, the concept of a hadron loses its meaning. At extreme densities, a medium constituted of unbound quarks forms [24].

In relativistic thermodynamics, higher densities can be obtained either by increasing the net baryon number, or by

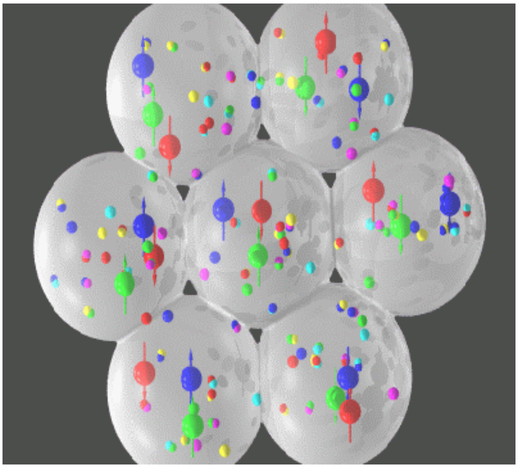

(a)

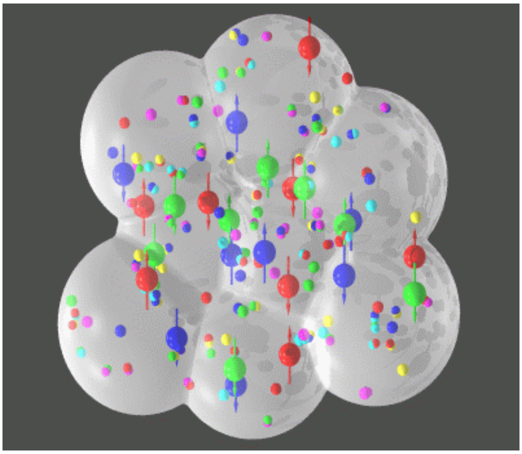

(b)

Figure (1-6): Pictorial view of the compression of the nuclear matter: the composite nucleons, with their finite spatial extension, are packed together (a); if compressed above a critical density they start overlapping and the quarks cannot identify their previous partners (b); the matter is thus deconfined. [25]

"heating" the system, so that collisions between its constituents produce further hadrons. This leads to the phase diagram shown in Figure (1-7): for low values of temperature T and baryon density ρ_B, we have confinement and hence hadronic matter; for high T and/or ρ_B, deconfinement sets in and we get a particular phase of the matter called the Quark Gluon Plasma (QGP) [26-28].

Compressing the nuclear matter at T = 0, its properties can be understood in terms of a degenerate Fermi quark gas. By increasing T at low, we are heating matter until it becomes a quark gluon plasma. Strong interaction thermodynamics thus predicts the existence of new, deconfined state of matter at high temperatures and densities. In the following paragraphs, the creation of this state and its main features will be described.

(1.7) Probing QGP

Since it is impossible to directly observe this short lived (~ some fm/c) QGP system, the experiments like CMS take the challenge to study the different behavior of observables to infer on the existence and on the properties of this matter phase. The signatures of the QGP can be divided in different categories, related to the different stages considered by the evolution picture described before: the deconfined medium (QGP), a possible interacting hadronic medium, and the final hadronic state [29]. The main direct hard probes of the creation of the QGP phase are:

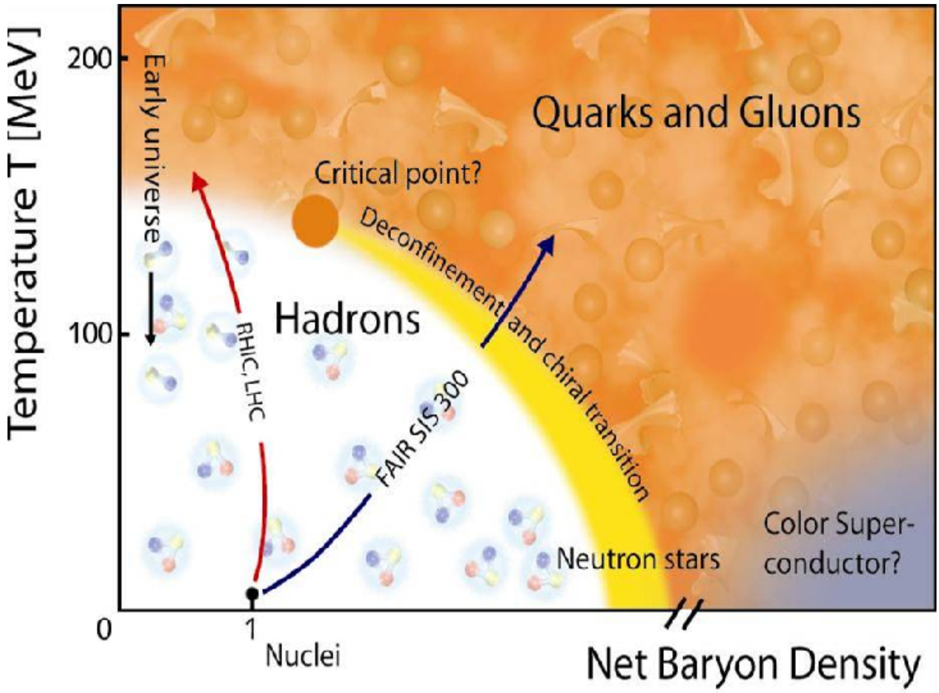

Figure (1-7): The phase diagram of QCD. For low temperature and baryon density the matter is in the ordinary nuclear conditions. Rising the density and/or the temperature a phase transition to the Quark Gluon Plasma should occur. The red arrow shows approximately the range of temperature and density that are studied by the RHIC and LHC experiments.

- **Hard emission of thermal dileptons and photons**. These are a sort of internal probe: they are produced by the QGP itself and are not affected by the subsequent states of the medium, since they undergo only weak and electromagnetic interactions after their formation; therefore, they bear the imprints of the bulk properties of the early stages of the interaction and can be used as a thermometer of the medium, since they are produced also by the confined matter. However, this is also the main drawback of this study: it is very difficult to separate thermal dileptons and photons from the abundant hadronic production; moreover, the presence of a prompt component produced by early hard parton interactions in the primary and pre-equilibrium stages, has to be taken into account and separated as well.
- **Production of quarkonium states** (J/ψ, Υ) in the primary parton collisions. These states are produced before the existence of any medium but their dissociation is possible in a deconfined medium; their observed behavior indicates therefore whether the subsequent medium was deconfined or not, resulting in a sort of external probe.
- **Jet quenching**. The energy loss of partons passing through the hot deconfined medium is expected to be larger than through the hadronic matter.

Information about the evolution of the hadronic system, in particular about its last stage, where the hadrons are still interacting, can be provided by:

- **In-medium modifications of resonances observable in their decays**. The changes of their masses or widths can originate from the large rescattering cross section in the medium, where the final state interactions influence in particular the hadronic decays. The study of these changes should be useful to distinguish between different expansion and freeze-out scenarios.
- **The expected QGP probes produced in the hadronization phase**, the so called soft probes, which appear when the density of the medium has dropped sufficiently to allow the existence of hadrons, are:
  - **I.** **Strangeness enhancement**. A hot QGP should contain the different quark species in almost equal amounts, which, if preserved up to hadronization, should result in more abundant strangeness production than observed in p-p interactions, where the strange quark abundance is suppressed.
  - **II.** **Collective flow and transverse momentum broadening**. Compared to pp interactions, a hot initial QGP could lead to more pronounced expansion and specific expansion patterns.

(1.7.1) Energy loss

Travelling through the QGP, a parton loses energy mainly because of collisional and radiative energy loss [30]. The quantity of energy transferred by radiative energy loss from a parton to the medium depends on the medium properties. According to the BDMPS [31, 32] model it can be expressed as

$$\Delta E \propto \alpha_s C_R \hat{q} L^2$$

In this formula C_R is the *Casimir factor*, which depends on the color charge of the parton (4/3 for quark–quark scattering and 3 for gluon–gluon scattering), $\hat{q}$ is the medium transport coefficient, proportional to the gluon density, and L is the distance travelled in the medium. Then if really there is a QGP medium we expect high p_t hadrons to be formed near the fireball border, because partons created in the centre of the fireball will lose too much energy before escaping the fireball, as shown in figure (1-8). This means that while in p–p collisions jets are produced back to back, in heavy ions collisions we anticipate the away side jet to be likely absorbed in the medium. This was observed at RHIC, as in figure (1-9) showing the jet distribution for Au–Au; d–Au and p–p collisions. The same effect is also observed at the LHC. The asymmetry ratio A_j

$$A_j = \frac{(p_{t,1} - p_{t,2})}{(p_{t,1} + p_{t,2})}$$

in the momentum of reconstructed jets measured at the CMS experiment [33], as shown in figure (1-10). The increase of the asymmetry with the centrality of the collisions shows that if the centrality of the collision increases, the away side jets lose more energy to the medium. The energy of the away side jet is finally recovered when increasing the radius used to reconstruct the jet momentum. A similar behavior was also observed by the ATLAS experiment [34].

If the partons energy loss in the medium the p_t distribution for the produced particles will be softer. This effect can be quantified by using the nuclear modification factor R_{AA}, this factor is defined as the ratio between the p_t distributions for produced particle in nucleus-nucleus and proton-proton collisions divided by the average number of binary collisions in the case of nucleus-nucleus collisions N_{coll} (centrality).

$$R_{AA}(p_t) = \frac{1}{\langle N_{coll} \rangle} \left[\frac{dN_{AA}/dp_t}{dN_{pp}/dp_t} \right]$$

If $R_{AA} = 1$, this happens if a nucleus-nucleus is only the superposition of N_{coll} proton-proton collisions. According to the wounded nucleon model [35], the number of particles produced in a nucleus-nucleus collision is expected to be proportional to the number of participants at low p_t and to the number of nucleon-nucleon collisions at high pt. If the QGP does created, the expected value for R_{AA} will increase from 1/6 to a value close to 1 with increasing p_t. The first is of this relation (at low p_t) is known as *the Cronin enhancement,* discovered at FermiLab in proton–nucleus collisions. For p_t larger than 2 GeV it was observed the value of R_{pA} (proton–nucleus collisions instead of nucleus–nucleus) was bigger than 1. The explanation of this effect is that before suffering the inelastic collision the partons in the projectile proton undergo some elastic scattering with some partons of the target acquiring a small transverse momentum component. In this way when the hard scattering occurs, particles will be produced with a small momentum contribution k_t that is, on average, different from zero. A second effect that needs to be estimated is the modification of parton distribution functions for

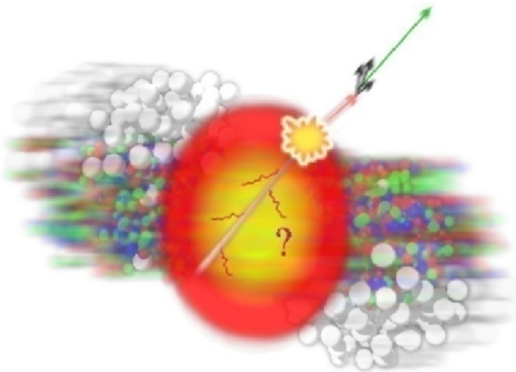

Figure (1-8): Jet creation in the medium

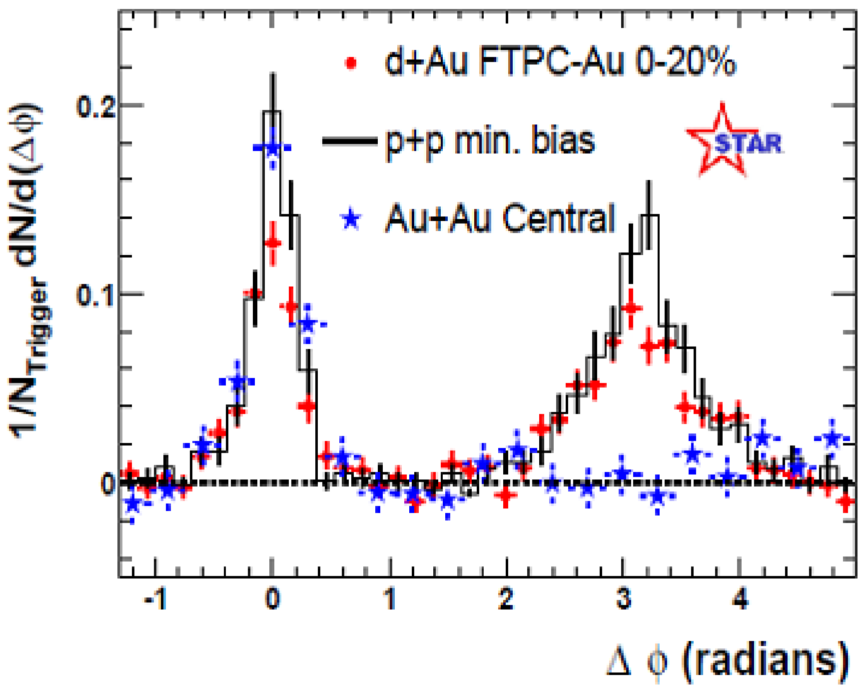

Figure (1-9): Azimuthal distribution of particles with respect to leading particle (jet) at STAR (RHIC) in p–p, d–Au and Au–Au collisions. The away side jet distribution is clear for p–p and d–Au systems, but it disappears in Au–Au collisions.

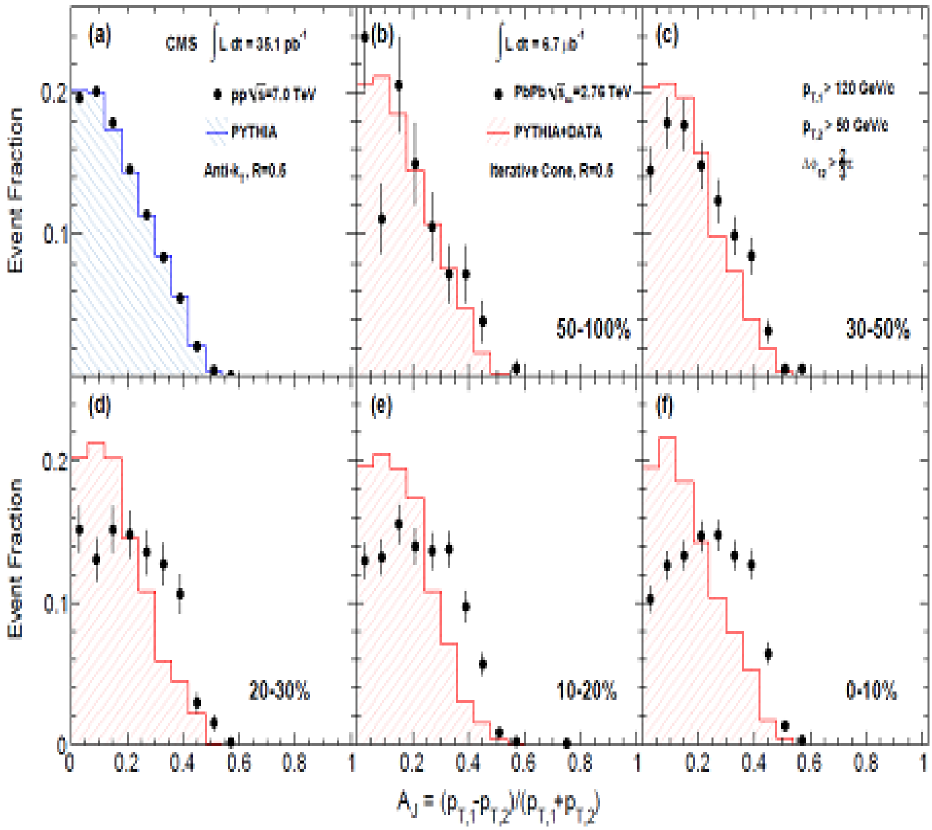

Figure (1-10): Di-jet asymmetry ratio in Pb-Pb events at $\sqrt{s_{NN}}$= 2.76 TeV with the CMS experiment [33]. Selected events have a leading jet with $p_{t,1}$ > 120 GeV/c and subleading jet with $p_{t,2}$ > 50 GeV/c and a separation between the two jets of $\Delta\phi_{12}$>2π/3. Panel (a) show the p-p reference data at $\sqrt{s}$= 7 TeV compared to PYTHIA simulations. Panels from (b) to (f) show Pb-Pb data in different centralities compared to true Pb-Pb events with embedded PYTHIA events. A clear increase of the asymmetry between the two jets while going towards central collisions is visible.

nucleons in a nucleus. The nuclear modification factor as a function of p_t observed for charged hadrons is visible for results from RHIC in figure (1-11) and from ALICE in figure (1-12). A final state effect pointing to the QGP creation is visible. The R_{AA} value goes asymptotically to the ratio between participants and collisions. An interesting possible interpretation of this feature is the following: the number of participants is proportional to the volume of the interaction region (i.e. to the volume of the fireball) while the number of collisions goes like $N_{part}^{4/3}$. So

$$\frac{N_{part}}{N_{coll}} \propto \frac{V}{V^{4/3}} \propto \frac{1}{R_{fireball}}$$

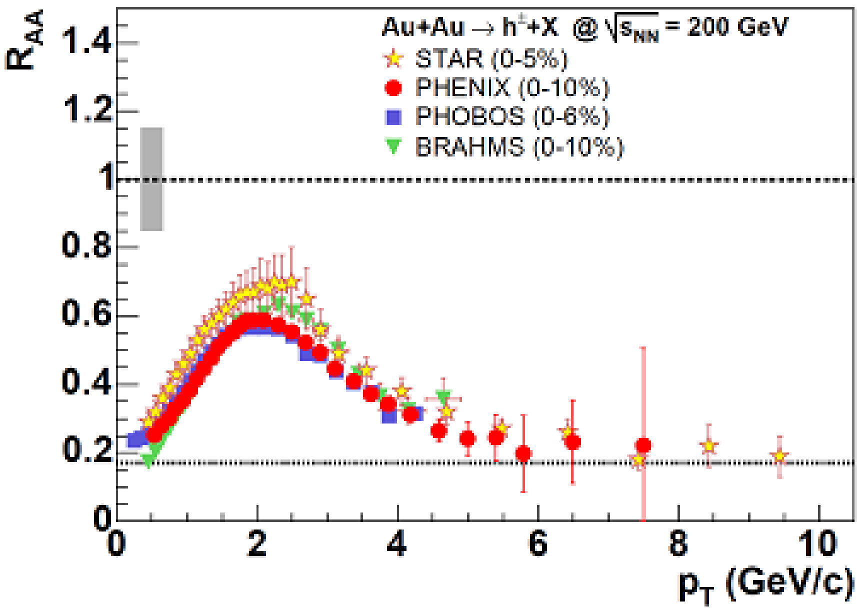

Figure (1-11): Inclusive charged hadron R for central Au–Au collisions at RHIC

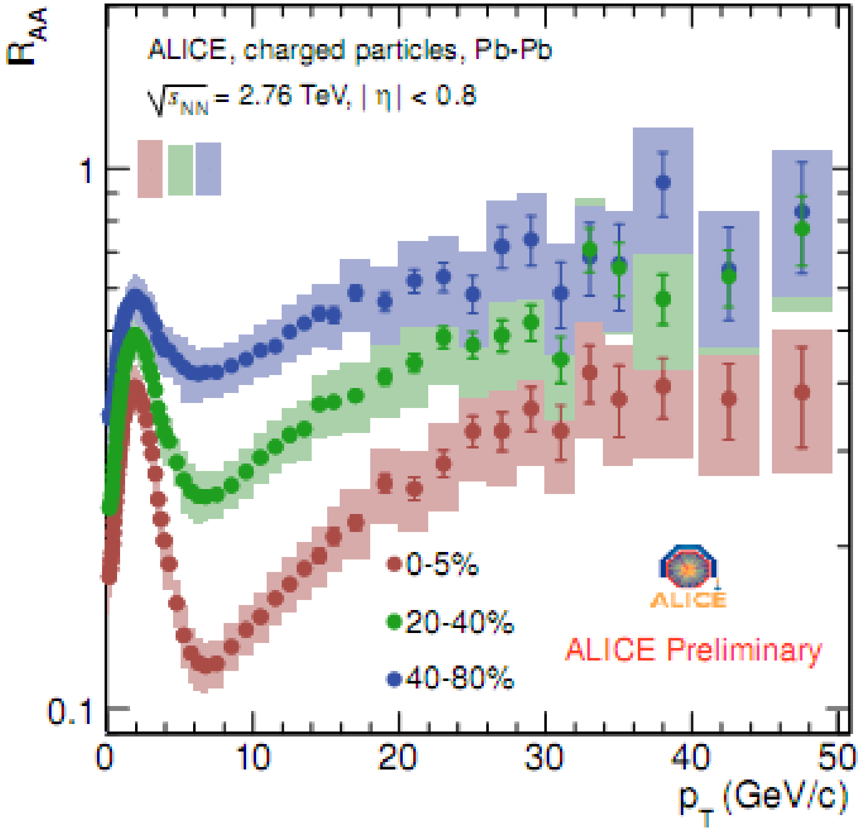

Figure (1-12): Nuclear modification factor of charged hadrons in ALICE as a function of p_t for three different centralities.

(1.7.2) J/ψ Suppression:

In 1986, Matusi and Satz argued that a sign of QGP creation would be the disappearance of quarkonia states like the J/ψ [36]. These quarkonia states are bound systems formed by $c\bar{c}$ (charm and anti-charm quarks). According to Lattice QCD calculations, above critical temperature T_c the heavy- quark potential is effectively screened the QGP, this means $c\bar{c}$ bound states melt in the medium. This melting produces a suppression of final $c\bar{c}$ states and also increases an open charm particle production.

In NA50, this Collaboration studied Pb-Pb collisions at the CERN-SPS, with incident energy $\sqrt{s_{NN}} = 158$ GeV, the collaborators in that experiment showed that the ratio of measured J/ψ spectrum to expected is one when only ordinary nuclear absorption is taken into account as shown in figure(1-13) [37,38,39]. Suddenly, this ratio change when the energy density is larger than twice the critical energy. This ratio is less than one which means a suppression for J/ψ production. This suppression effect can be understood as a result of formation of QGP. The suppression scenario could change at higher energies that available at RHIC (Relativistic Heavy Ions Collider) and LHC (Large Hadron Collider), because the production of charm quarks will be large and the recombination of $c\bar{c}$ pairs could lead even to an enhancement of their expected production [40].

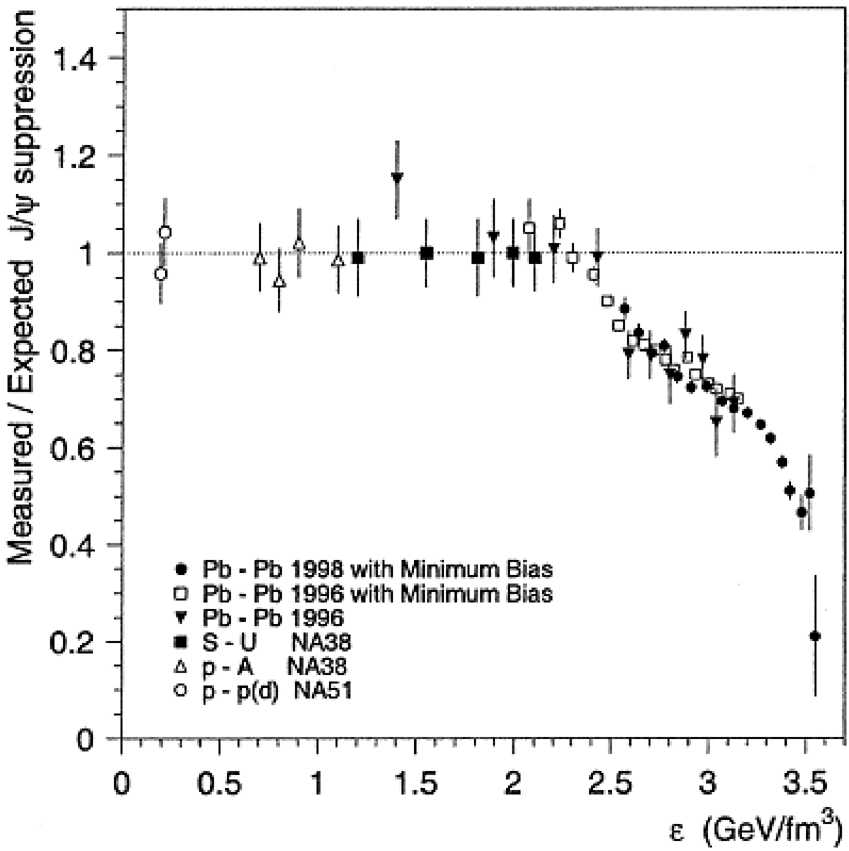

Figure (1-13): Measured J/ψ production yields normalized to the expected yields assuming that the only source of suppression is the ordinary nuclear absorption [38].

(1.7.3) Strangeness enhancement

One of the possible implications of the phase transition is the restoring of the chiral symmetry. If that happens then strange quark mass should reduce from ~ 500 MeV/c^2 to about 150 MeV/c^2. This makes more favorable the production of $s\bar{s}$ pairs in gluon fusion processes. The observation of strangeness enhancement per se would not be a sufficient condition to claim a medium effect. In fact, even in a hadron gas processes like

$$\pi + \pi \rightarrow K + K$$

$$or \quad \pi + N \rightarrow \Lambda + K$$

enhance the strangeness content. What is important is therefore the relative enhancement of strangeness for particles with different strange content. We can define the enhancement of the particle of species Y as

$$E(Y) = \frac{\left(N_Y/\langle N_{part}\rangle\right)_{AA}}{\left(N_Y/\langle N_{part}\rangle\right)_{PP}}$$

The mechanism for strange quark-pair production can be described by thermal reactions in the plasma such as gluon fusion ($gg \rightarrow s\bar{s}$), which turns out to be the dominant process of $s\bar{s}$ pair production, as shown in figure (1-14). In the same figure (b), the Feynman diagrams for such reactions are illustrated [41].

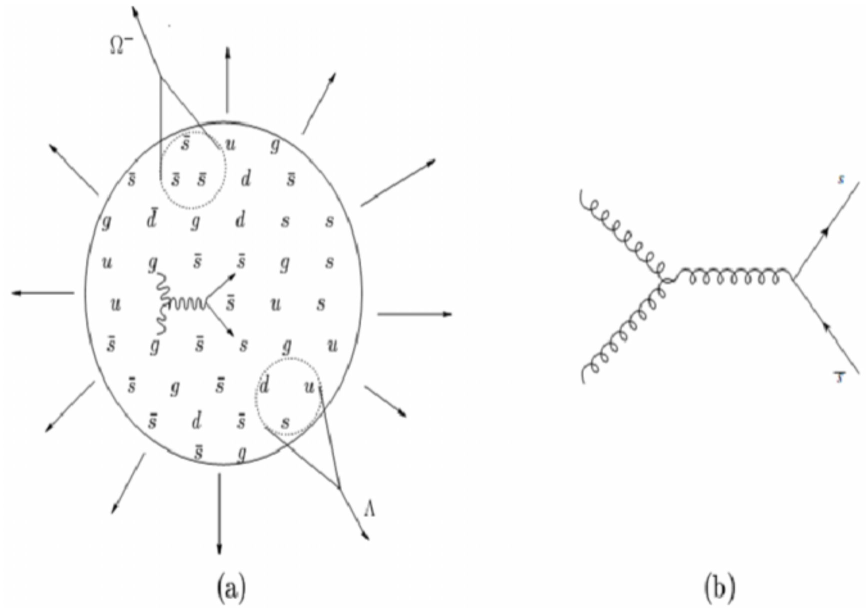

Figure (1-14): (a) Mechanism of strange hadron formation from the QGP: inserts show gluon fusion creating strangeness, followed by QGP recombinant hadronization, (b): Feynamn diagram for thermal gluon fusion [41].

(1.7.4) Elliptic flow:

In the early stage of collisions, pressure gradient can be produced leading to the expansion of the system [42]. It was found that for non-central heavy-ion collisions, an overlapping area was observed in the reaction region, as shown if figure (1-15). It turns out that the overlapping area have an elliptic shape; the re-scattering processes among particles are thought to be responsible for transferring this spatial deformation onto the observed anisotropic transverse momentum distributions of the measured hadrons. Elliptic flow is defined to be the second Fourier coefficient of the azimuthal distributions expansion of anisotropic flow, its notation is ν_2 [43]. The first coefficient is known as directed flow. The harmonic number can be defined as:

$$\frac{dN}{d\varphi} = \frac{\nu_0}{2\pi} + \frac{\nu_2}{\pi}\, cos2\varphi + \frac{\nu_4}{\pi}\, cos4\varphi + \;\ldots\ldots..$$

The sin terms (odd coefficients) do not contribute to the anisotropic terms as reflection symmetry with respect to the reaction plane makes them go to zero. So, the coefficient of elliptic flow can be calculated as:

$$\nu_2 = \langle \cos\,(2(\phi - \psi_R \rangle$$

Where $\phi - \psi_R$ is the azimuthal angle around the beam measured relative to impact parameter, as shown in figure (1-16); the brackets indicate an average over the single particles distribution $(dN/dp_t d\phi)$. The study of elliptic flow has been developed considerably at RHIC energies [44]. Some models

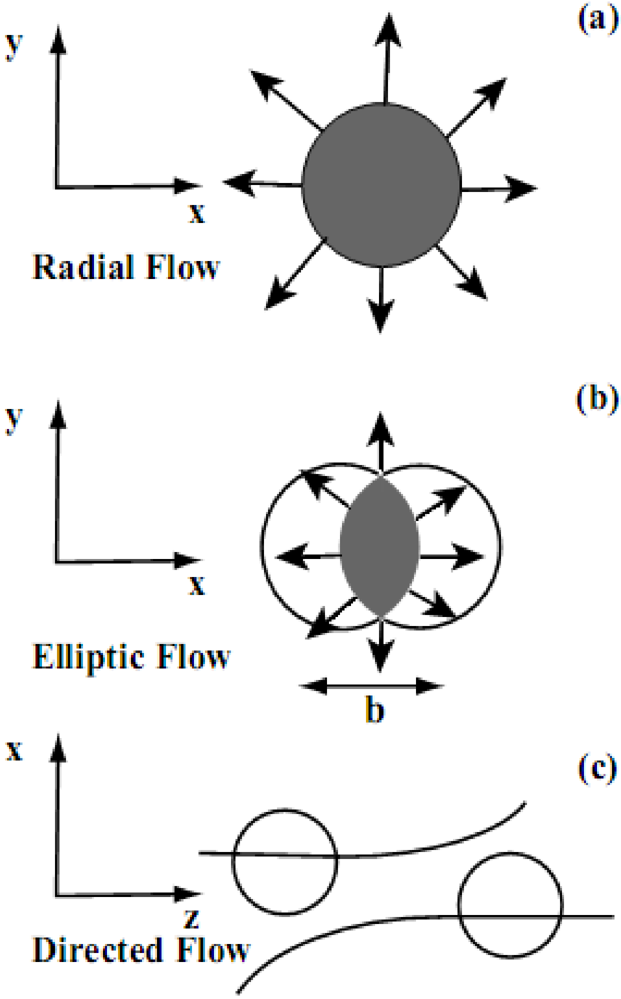

Figure (1-15): Illustration of the three most common flow phenomena.

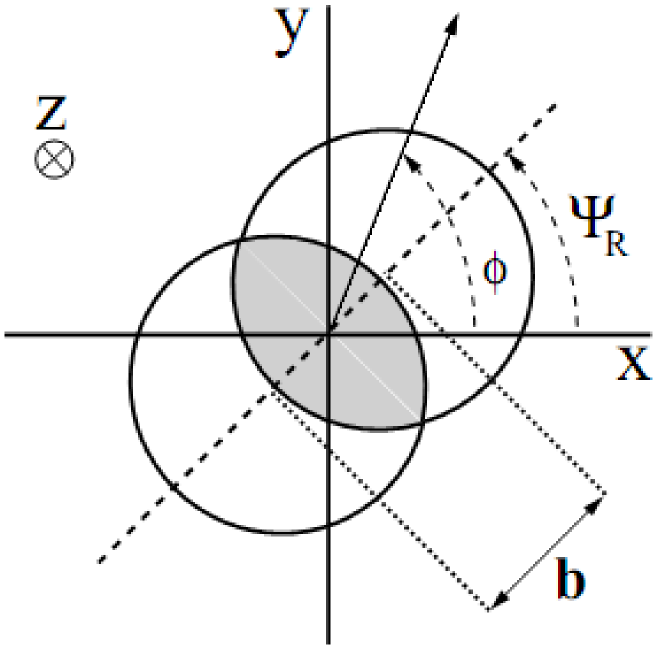

Figure (1.16): Definition of the coordinate system.

based on relativistic hydrodynamics tried to describe the flow. They attempt to study the evolution of the system assuming a continuous flow of particles from the produced high energy collisions. This is so at high energy densities where the mean free path of various particles has been measured at RHIC. Calculations based on hydrodynamical model have been compared to data. Two different behaviors are observed for the low and high transverse momentum region. For particles with $p_t < 2\ GeV/c$, the elliptic flow can be modeled by hydrodynamics [45], whereas for high p_t particles, a significant deviation was observed relative to such calculations. Furthermore, it was found that there is a mass dependence that was unexpected at high transverse momentum before the RHIC results. What this suggests is that hydrodynamic calculations cannot provide a complete description of this phenomenon [46].

Chapter 2

LHC and

CMS Experiments

(2-1) Large Hadron Collider:

The Large Hadron Collider (LHC) at CERN, Geneva, Switzerland, is located about 100 m underground near the French-Swiss border. It started to produce collisions in the autumn of 2009.

LHC is housed in the tunnel of the former Large Electron-Positron Collider (LEP1) [47], LHC is the most powerful particle accelerator ever built. To achieve the goal of increasing the production rate of rare particles both the center-of-mass energy and the luminosity of the LHC are unprecedented among hadron colliders.

The main motivation for constructing the LHC is to establish the nature of electroweak symmetry breaking for which the Higgs mechanism is the presumed main candidate. Additions to the Standard Model (supersymmetry, extra dimensions) can also show up at the TeV scale.

New physics is expected to explain the nature of dark matter, dark energy, and could possibly pave the way toward a unified theory via extra-dimension, which requires modification of gravity at the TeV scale.

The physics goals of the LHC also include B-physics and CP violation. Previous experiments have already observed a small CP violation effect, but it’s not enough to account for the apparent matter-antimatter imbalance in the Universe. LHC is designed to accelerate and collide proton bunches at a centre of mass energy of 14 TeV and heavy ion (lead) bunches at 5.5 TeV per nucleon pair. Currently the LHC is running at half of the nominal energy, providing proton-proton collisions at $\sqrt{s} = 8$ TeV and Pb-Pb collisions at $\sqrt{s_{NN}} = 2.76$ TeV. Proton-ion collisions are also in the capabilities of the LHC and the first p-A collisions are expected for January 2013. LHC is allowing us to further extend the study of QCD matter under extreme conditions of temperature, density, and parton momentum fraction (low-x). Hence, there are many compelling reasons to investigate the TeV energy scale with the LHC.

The Large Hadron Collider measures about 27 km in circumference and is installed underground between 45 and 170 meters below the Swiss-French border area near Lake Geneva near the Jura Mountains and the Alps. An overview of the general layout of the accelerator complex can be seen in Figure (2-1). The protons are produced in a duoplasmatron, where hydrogen is ionized, and injected in the LINear ACcelerator 2 (LINAC2) which increases their energy up to 50 MeV. The protons exiting from the LINAC2, grouped in bunches with a one third the speed of light, start a stage where they go through several circular- shaped accelerators which lead them to the LHC ring. The first one is the Proton Synchrotron Booster (PSB) a four ring accelerator, leading to protons with energy of 1.4 GeV and to 190 ns bunches. After that the protons are injected in the Proton Synchrotron (PS) which accelerates them up to 25 GeV and further divides them in more compressed bunches:

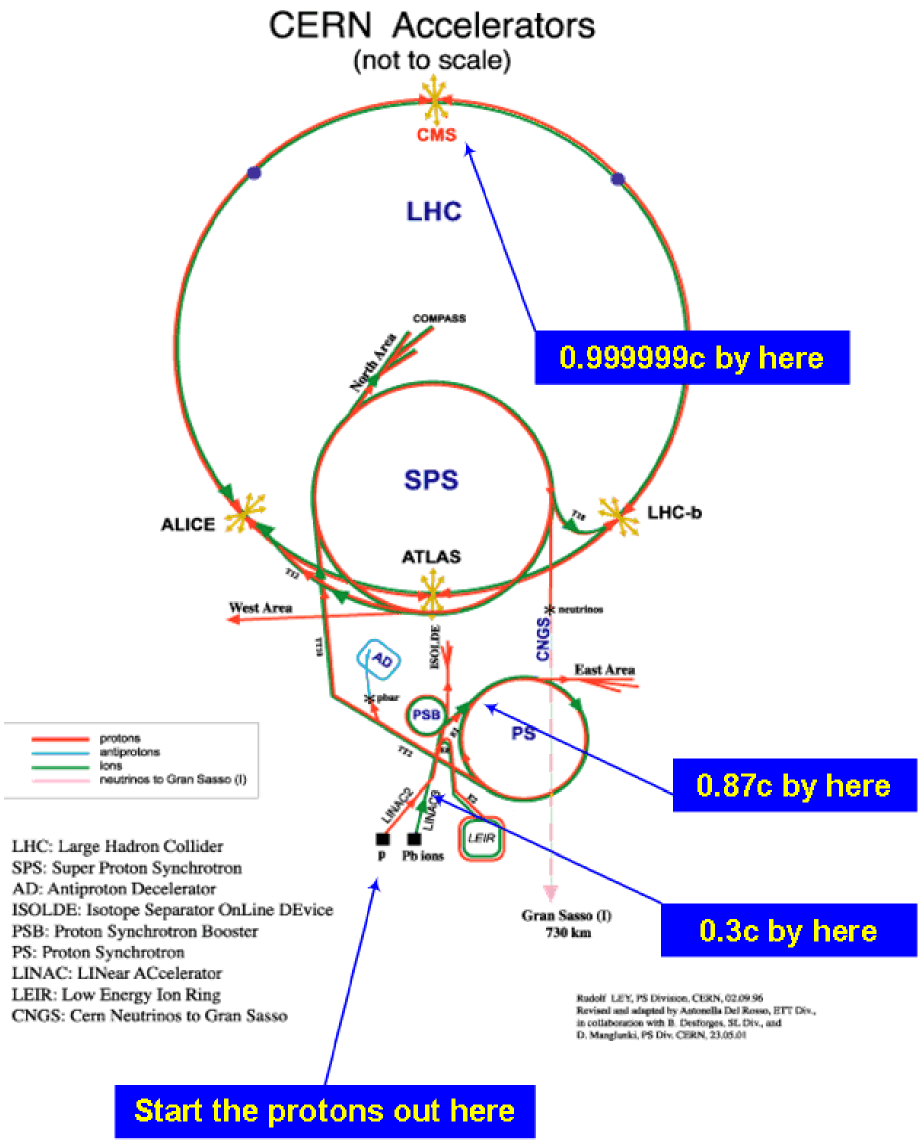

Figure (2-1): Schematic view of the LHC accelerator complex with its four main experiments.

the separation time is 24.95 ns and the long is less than 4 ns. The proton bunches are injected in the Super Proton Synchrotron (SPS) where undergo an acceleration up to 450 GeV. The proton bunches are now ready (many high intensity bunches with small transverse and well defined longitudinal emittance) to be injected in the LHC accelerator.

In the LHC the two beams circulating in opposite directions are accelerated in different vacuum chambers separated by 194 mm in the horizontal plane, and at about 100 m before the interaction points the two pipes join into one. Since the installation space in the LEP tunnel is limited a twin-bore (two-in-one) magnet design has been adopted for almost all of the LHC superconducting magnets. Figure (2-2) shows the division of LHC in eight regions [48], giving rise to the eight octants, sectors and interaction Points (IP).

Two Radio Frequency (RF) cavity structures are hosted in the 4th octant; each one is dedicated to one beam. At IP6 the dump insertion is situated. It is a combination of horizontally deflecting fast-pulsed magnets and vertically-deflecting magnets which serve to vertically extract the beams from the machine. The 3rd and 7th octants house collimators needed to remove halo particles with large transverse and longitudinal oscillation amplitudes respectively.

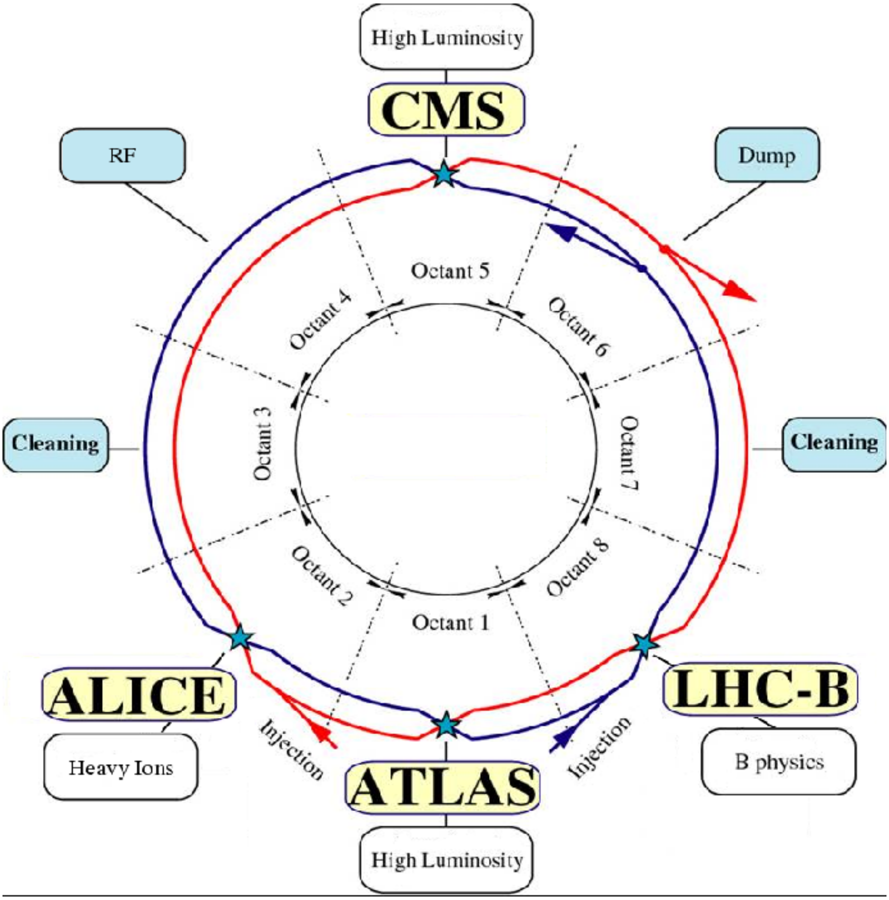

Figure (2-2): A schematic view of the Large Hadron Collider showing the positions of the main experiments. The beam switches magnet bores at these four points, allowing collisions to take place. The two general purpose detectors, CMS and ATLAS, are located diametrically opposite each other at the high luminosity interaction points. The other two interaction points, for LHCb and ALICE, are shared with the injection systems for the two beams.

Four main experiments are installed around the crossing points of the two proton beams:

- ALICE (A large Ion Collider Experiment) [49], a detector designed to investigate collisions of lead nuclei at center of mass energy of 5.5 TeV per nucleon when LHC beams energy is14 TeV for protons. Under these extreme conditions, a new state of matter, called quark-gluon plasma can be studied. The high particle density in heavy ion collisions requires extreme radiation hardness of detector components especially close to the interaction point and track reconstruction suitable for thousands of particles in a single event.

- LHCb (LHC beauty) [50], the only asymmetrical detector at the LHC, specializes in investigating the production and decay of particles containing b-quarks. The central focus lies on providing the best possible resolution of secondary vertices along the beam-line which are a typical signature of b-quark decays.

- ATLAS (A Toroidal LHC Apparatus) [51] and CMS (Compact Muon Solenoid) [52, 53] are two multi-purpose detectors with different construction principles and magnetic field designs. Both have a broad physics program including Standard Model and new physics. The main goals of the experiments are:

    1. To explore particle physics cross-sections in the

TeV scale.

2. Discover the Higgs boson, the scalar boson particle thought to be responsible for giving mass to particles.

3. Look for evidence of supersymmetry.

4. Search for extra dimensions, showing up as missing transverse energy [54].

5. Using Pb nuclei, study heavy ion collisions.

6. Make more accurate measurements of already discovered particles, such as, the top quark.

ATLAS and CMS are located vis-à-vis at Access Point 1 and 5 respectively, while ALICE is housed in Point 2 and LHCb in Point 8.

The maximum energy of LHC collisions is dictated by the radius, R, of the existing LEP tunnel which houses the collider and the integrated magnetic field around the ring. The integrated field is given by the magnetic field generated by the dipoles and the effective 'bending radius' of the magnets. The LHC uses superconducting NbTi magnets, cooled to 2K, which generates a nominal field of 8.33 T with $R_{bending} = 2803.95\ m$. These parameters then allow to accelerate a proton up to a proton momentum $7 TeV c^{-1}$:

$$p = eBR_{bending} = 3\text{x}10^8 x 8.33 x 2803.95 \text{ eV} = 7.00\ TeVc^{-1}$$

The rate of events expected, R_{event}, is the product of the luminosity and the cross section for that event:

$$R_{event} = L\sigma_{events} \tag{2.2}$$

The study of rare processes therefore requires a high luminosity. For example, a promising discovery channel for a low mass Higgs boson is $H \to \gamma\gamma$, yet for $m_H = 125$ GeV, the predicted $\sigma(pp \to H).\ BR(H \to \gamma\gamma)$ ~ 100 fb leads to a rate of only 10^{-3} Hz at $L = 10^{34} cm^{-2} s^{-1}$.

The protons of the LHC beams are bunched, with a separation of 25 ns (designed value) between these bunches, but now the separation between bunches is 50 ns. The luminosity is related to the number of protons per bunch, n_b ; the number of bunches in each beam, N_b and the revolution frequency of these bunches, f_{rev} . γ_r is the Lorentz factor; ε_n the normalized transverse emittance; β, the Betatron function at interaction point and F, the geometric luminosity reduction factor arising from the crossing angle at interaction points.

$$L = \frac{N_b n_b f_{rev} \gamma_r}{4\pi\varepsilon_n \beta} F \tag{2.3}$$

The machine parameters needed to obtain the design luminosity are shown in Table (2.1).

Table (2.1): Important LHC working parameters. [55]

Parameter	Value	Unit	Symbol
Proton energy	7	[TeV]	
Number of bunches	2808		n_b
Number of particles per bunch	1.15×10^{11}		N_b
Stored energy per beam	362	[MJ]	
RMS beam size at CMS	16.7	[μm]	
Peak luminosity at CMS	1×10^{-34}	[$cm^{-2}S^{-1}$]	
Interactions per bunch crossing	19.02		
RMS bunch length	7.55	[cm]	
Luminosity life time	14.9	[h]	
Revolution frequency	11.245	[kHz]	f_{rev}
Relativistic gamma	7461		γ_r
Geometric luminosity reduced factor	0.836		F
Minimum turnaround time	1.2	[h]	
Approximated turnaround time after 10 years of running	7	[h]	

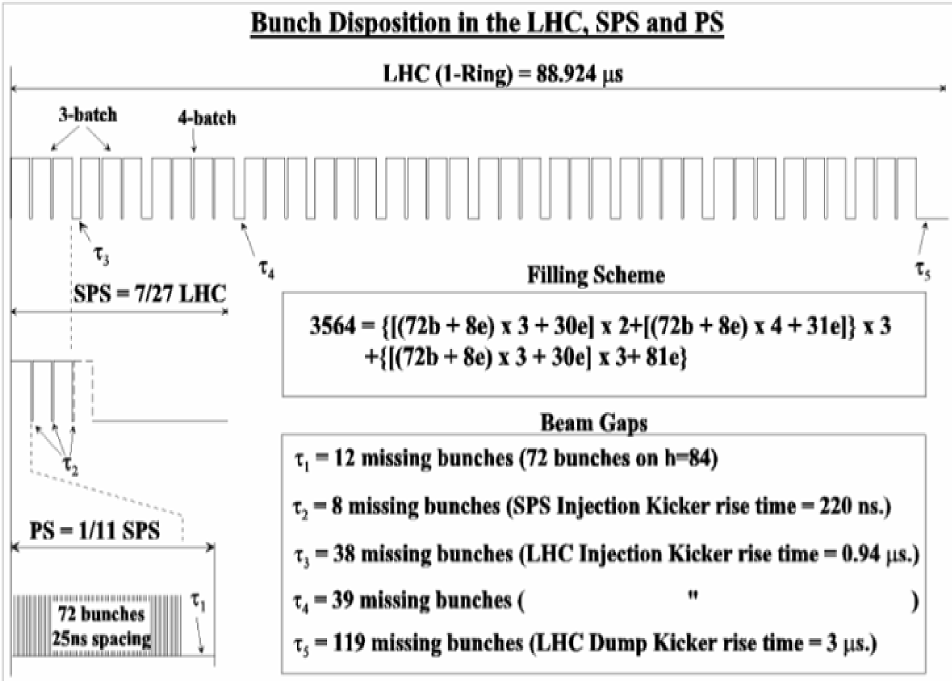

Figure (2-3): The proton synchrotron produces six batches of 72 bunches of 25 GeV protons, with 25 ns bunch spacing. Three or four of these batches are injected into the Super Proton Synchrotron and accelerated to 450 GeV, before injection into an LHC beam. This procedure is repeated twelve times, leaving 119 missing bunches at the end of bunch train to ensure safe ejection. [52]

There is a pattern of proton bunches – “filled” bunches – and intervals with no proton bunches- referred to as “missing” bunches. These empty bunches are due to the system of injecting bunches into the LHC from the preceding accelerators and to ensure a safe ejection of beam at the end of a run. The pattern is illustrated in Figure (2-3). In total, there are 3564 bunches; both filled and empty, in LHC fill.

The collision of two protons bunches with nominal parameters causes approximately 20 inelastic events, as can be seen using equation 2.2 and 2.3:

$$R = L\sigma$$

$$N = \frac{L}{n_b f_{rev}} \sigma$$

$$= \frac{1\text{x}10^{34}}{2808 \times 11245} 6\,\text{x}\,10^{-26}$$

$$= 19$$

The most of these will be soft, “pile-up” events, which may be obscuring interesting interactions which have a much lower cross-section.

(2-2) CMS (Compact Muon Solenoid) detector

CMS stands for Compact Muon Solenoid: compact because it is “compact” for its enormous weight for its size, muon for one of the particles it detects, and solenoid for the coil inside its huge superconducting magnet. It is a high-energy physics experiment located in Cessy, France, part of the Large Hadron Collider (LHC) at CERN.

The Compact Muon Solenoid (CMS) Experiment is one of the two experiments aiming for a wide range of physics results. The main scope is to discover new phenomena, since the LHC will provide an environment with physics conditions which have never been explored before. The experiments at LHC can also be exploited to perform measurements on specific physics topics, as precision measurements and non-perturbative QCD physics. The very extensive plan of the multi-purpose experimental apparatuses at P1 and P5, requires several conditions to be satisfied.

The requirements due to the LHC environment are summarized in the following:

- The high cross sections and luminosity which are being reached by LHC require the experiments to have complex triggers and radiation hard detectors.

- The short time between collisions (25 ns) requires fast readout of the high granularity detectors and good synchronization with the accelerator machine.

The detectors features required for the physics results that have been planned in the CMS design are here summarized [52, 53]:

- Good muon identification and momentum resolution over a wide range of momenta and angles, good dimuon mass resolution (~ 1% at 100 GeV/c^2), and the ability to determine unambiguously the charge of muons with p at least up to 1 TeV/c;

- Good charged-particle momentum resolution and reconstruction efficiency in the inner tracker. Efficient triggering and offline tagging of τ's and b-jets, requiring pixel detectors close to the interaction region;

- Good electromagnetic energy resolution, good diphoton and dielectron mass resolution (~1% at GeV/c^2), wide geometric coverage, π^0 rejection, and efficient photon and lepton isolation at high luminosities;

- Good missing-transverse-energy and dijet-mass resolution, requiring hadron calorimeters with a large hermetic geometric coverage and with fine lateral segmentation.

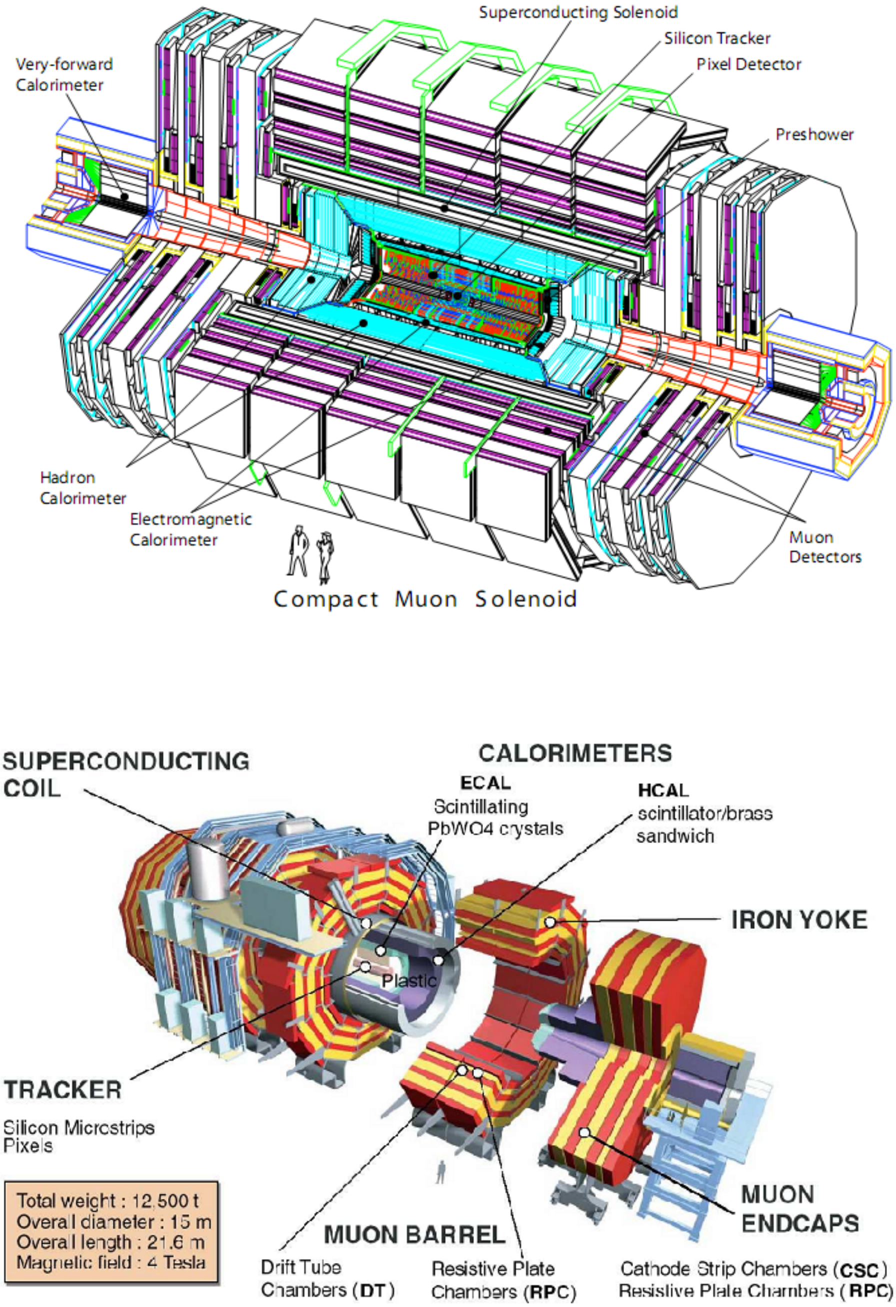

Figure (2-4): A perspective view of the CMS detector [48].

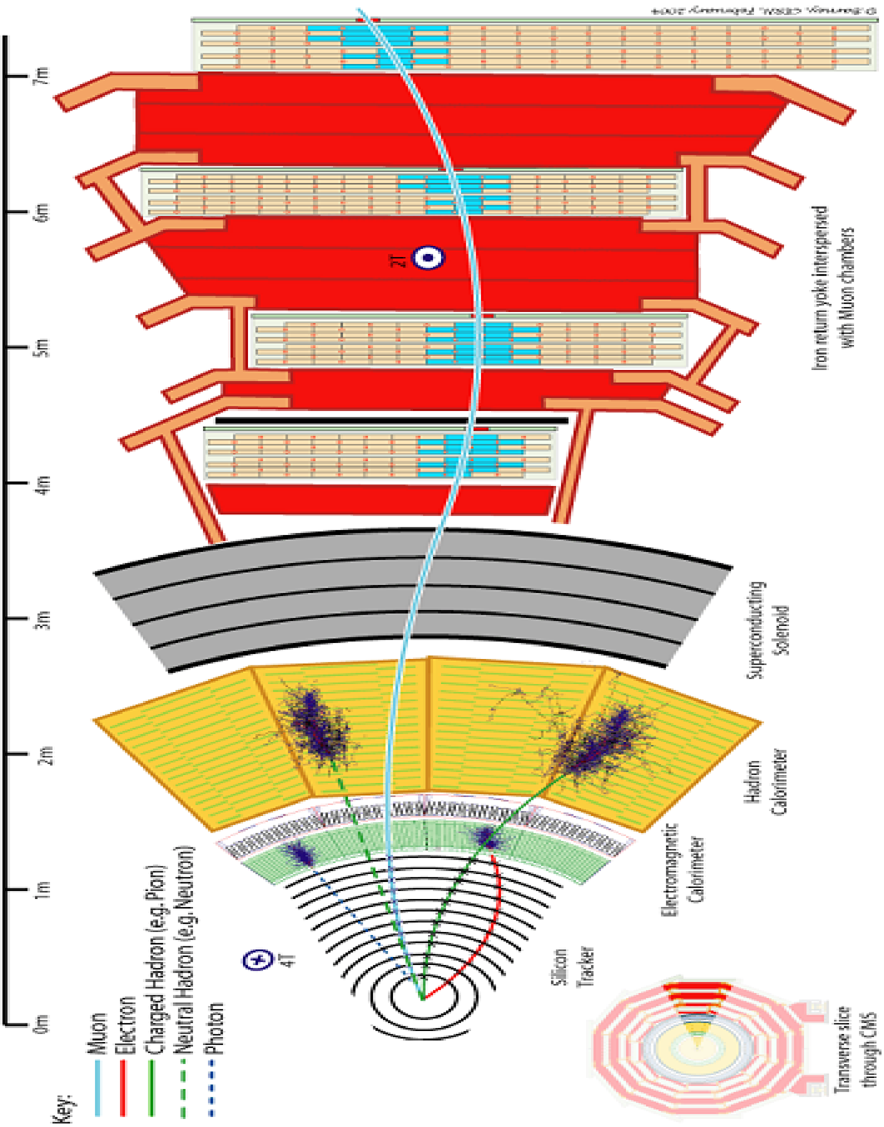

Figure (2-5): Cross section view of the CMS experiment showing the location of the detector systems.

The coordinate system adopted by the CMS Collaboration is as follows. The origin is centered at the nominal collision point, the y-axis points vertically upward and the x-axis point horizontally toward the center of the LHC ring. The z-axis lies along the beam and points toward the anti-clockwise beam direction. The azimuthal φ angle is measured in the x-y plane starting from the x axis, while the polar θ angle is measured from the z-axis toward the x-y plane.

The CMS apparatus has a cylindrical structure with the different sub-systems installed in a concentric shape around the LHC beam pipe at P5. It consists of several layers, each one is specialized to measure and identify different classes of particles. These detector layers are shown in Figures (2-4) and (2-5). The main feature of CMS is a magnet with diameter 6m, inside this magnet the inner tracking system, electromagnetic calorimeter, and hadron calorimeter, and outside is the muon system. In the following sections each sub-detector corresponding to each layer are discussed.

(2-2.1) Inner Tracking System (Tracker):

The CMS tracking system is the largest silicon tracker ever built. The CMS tracker records the paths taken by charged particles by measuring their positions at a number of key points.

The tracker can reconstruct the paths of high-energy muons, electrons and hadrons as well as tracks coming from the decay of very short-lived particles such as beauty or “b quarks”, and also provides a precise reconstruction of secondary vertices.

The inner tracking system surrounds the iteration points and its length 5.8 m and its diameter 2.5 m. CMS magnet provides a homogeneous magnet field 3.8 T over the full volume of the tracker. A schematic drawing of CMS inner tracking system is shown in figure (2-6).

According to the charged particle flux at various radii at high luminosity (Table 2.2), three regions can be delineated:

- Closest to the interaction vertex where the particle flux is the highest ($\approx 10^7$ /s at r $\approx$ 10 cm), pixel detectors are placed. The size of a pixel is $\approx 100 \times 150\ \mu m^2$, giving an occupancy of about 10^{-4} per pixel per LHC crossing.

- In the intermediate region ($20 < r < 55$ cm), the particle flux is low enough to enable the use of silicon microstrip detectors with a minimum cell size of 10 cm ×80 μm, leading to an occupancy of ≈ 2–3%/LHC crossing.

- In the outermost region ($r > 55$ cm) of the inner tracker, the particle flux has dropped sufficiently to allow use of larger-pitch silicon microstrips with a maximum cell size of 25 cm × 180 μm, whilst keeping the occupancy to ≈ 1%.

The closest sub-detector to interaction point is pixel detectors is 4 cm from the interaction point, and occupy the region till 20 cm. It is consisting of in the barrel region from 3

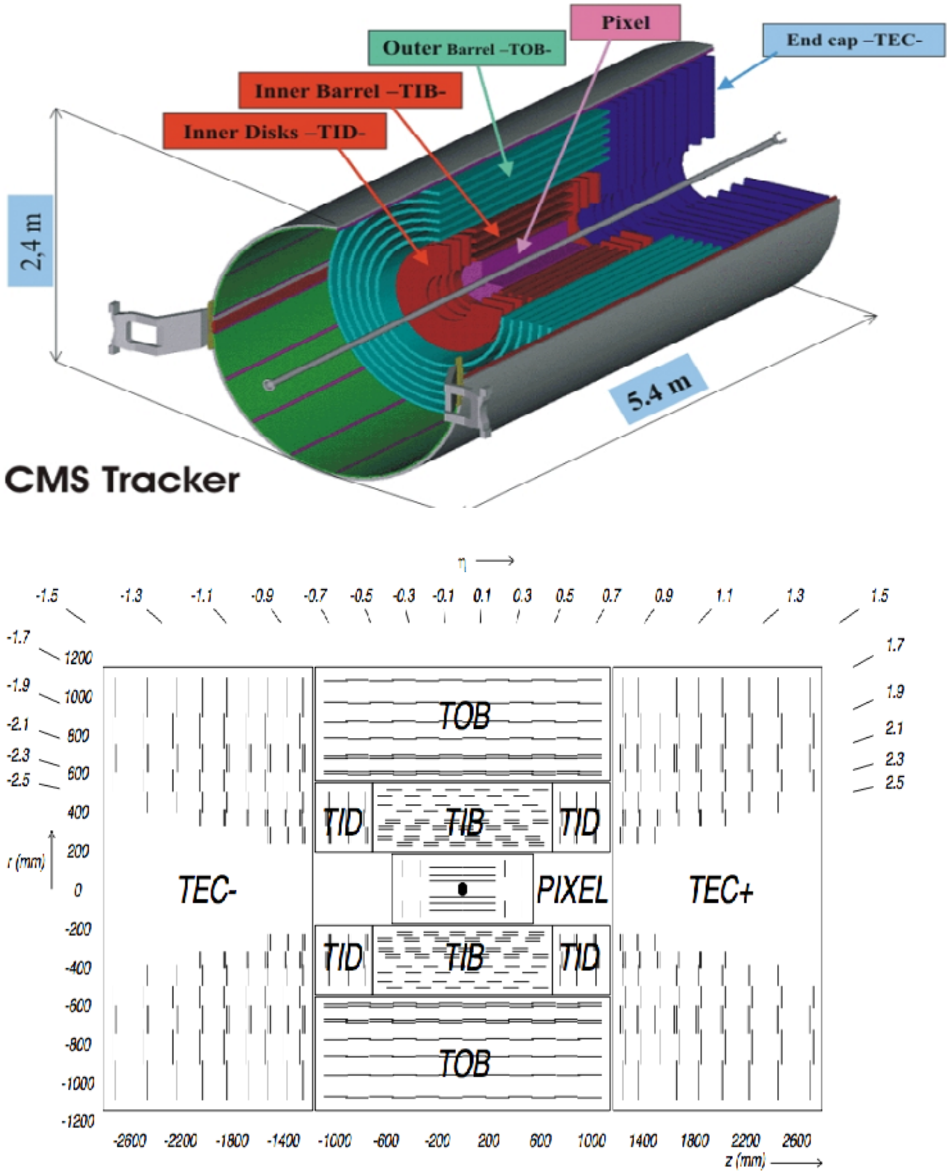

Figure (2-6): schematic drawing of CMS inner tracking system. Where : TIB /TID (Tracker Inner Barrel and Disk), TOB (Tracker Outer Barrel), TEC (The Tracker EndCap).

Table (2.2): Hadron fluence and radition dose in different radial layers of the CMS tracker (barrel part) for an integerted luminosity of 500 fb^{-1} (≈10 years)

Radius (cm)	Fluence of fast hadrons (10^{14} cm^{-2})	Dose (kGy)	Charged Particle Flux (cm^{-2} s^{-1})
4	32	840	10^8
11	4.6	190	
22	1.6	70	6×10^6
75	0.3	7	
115	0.2	1.8	3×10^5

layers of hybrid pixel detector with radii 4.4, 7.3, and 10.2 cm. At radii between 20 and 115 cm the tracking subsystem is constituted by the Silicon Strips detectors. Each system is completed by endcaps which consist of 2 disks for the pixel detector and 3 plus 9 disks for the strip tracker on each side of the barrel, extending the acceptance of the tracker up to a pseudorapidity of $|\eta| < 2.5$.

(2-2.1.1) Pixel detector:

The Silicon Pixel detectors consist of 66 millions of channels its radius extends to 20 cm. The Pixel detector is necessary for secondary vertices reconstruction from b-quark and tau decays and forming seed tracks for the reconstruction of outer track. In order to achieve the optimal vertex position resolution, with a pixel cell size of 100×150 μm^2 emphasis has been put on achieving similar track resolution in both $r-\phi$ and z directions which allows for an occupancy as low as 10^{-4} per pixel and per bunch crossing.

The Pixel detector consists of 3 barrel layers with 2 endcap disks on each side on them as shown in Figures (2-7) and (2-8). The 3 barrel layers have radii, 4.4, 7.3, and 10.3, and have a length of 53 cm and consist of 768 pixel modules arranged into half-ladders of 4 identical modules each. The 2 endcaps, extending from 6 to 15 cm in radius, are placed on each side at |z| = 34.5 cm and 46.5 cm.

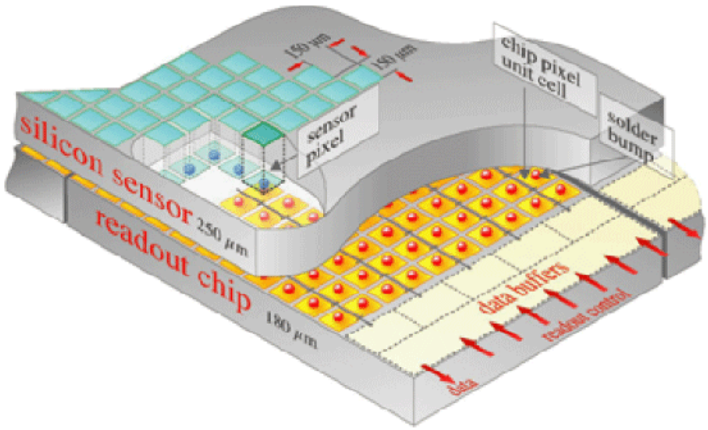

Figure (2-7): Illustration of the CMS pixel sensor and the readout chip, which is directly bump bonded onto the sensor.

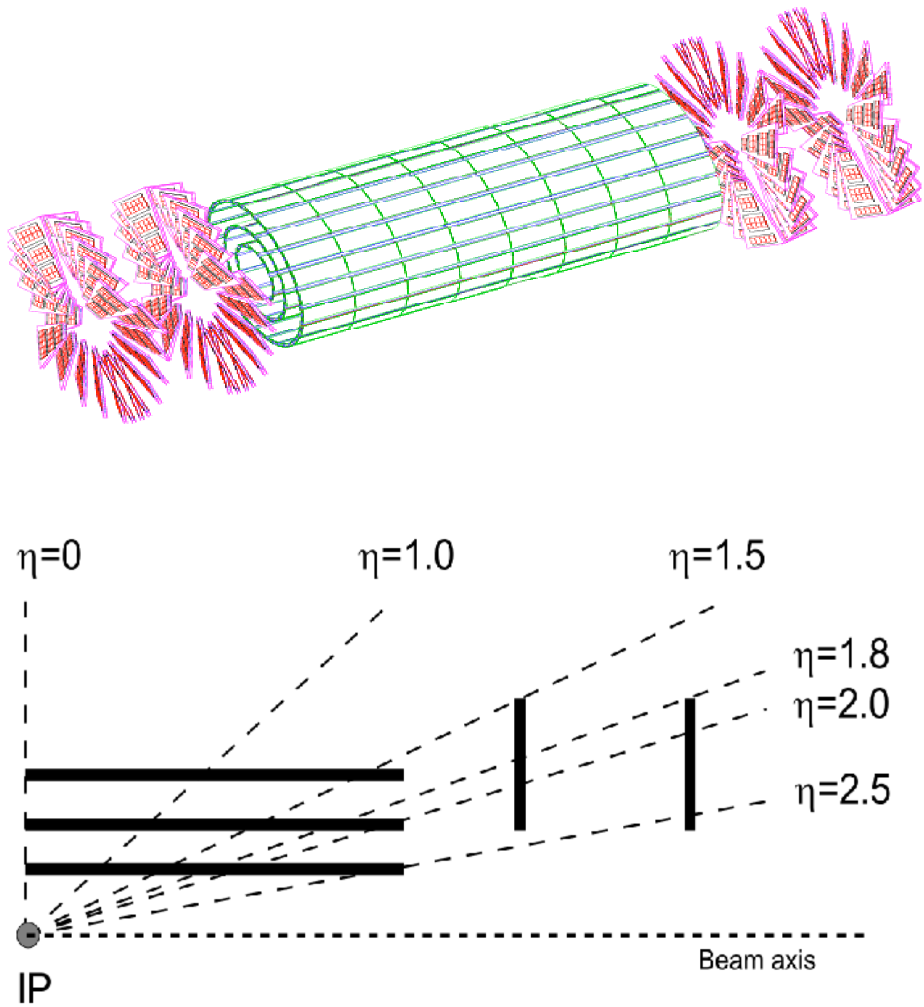

Figure (2-8): readout using approximately 16 000 readout chips, which are bump-bonded to the detector modules. Due to high rate radiation environment in the CMS experiment, the pixel detector will be replaced in the future operation.

The vicinity of interaction region has a very high track rate and particle affluences which require a radiation tolerant design. The endcap disks are assembled in a turbine-like geometry with blades rotated by 20◦ to induce charge-sharing. The endcap disks comprise 672 pixel modules with 7 different modules in each blade.

The spatial resolution is measured to be about 10 μm for the r-φ measurement and about 20 μm for the z measurement. The detector is readout using approximately 16 000 readout chips, which are bump-bonded to the detector modules.

(2-2.1.2) The Silicon Strip Detector:

A radius larger than 20 cm has a lower track density, this means the radiation levels are smaller in this region, and this Silicon Strip detector can be used. The schematic layout of the silicon microstrip detector is shown in Figure (2-9).The silicon strip tracker is composed of 15148 detector modules, it occupies the radial region from 20 cm to 116 cm. The barrel region in the strip tracker is divided in to three different subsystems:

1. **Tracker Inner Barrel and Disk (TIB /TID):** extend in radius towards 55 cm and are composed of 4 barrel layers, supplemented by 3 disks at each end. The thickness of silicon sensors is 320 μm. The first 2 layers are made with “stereo” modules in order to provide a measurement in both r-φ and r-z coordinates. A stereo angle of 100 mrad has been chosen. This leads to a single-point

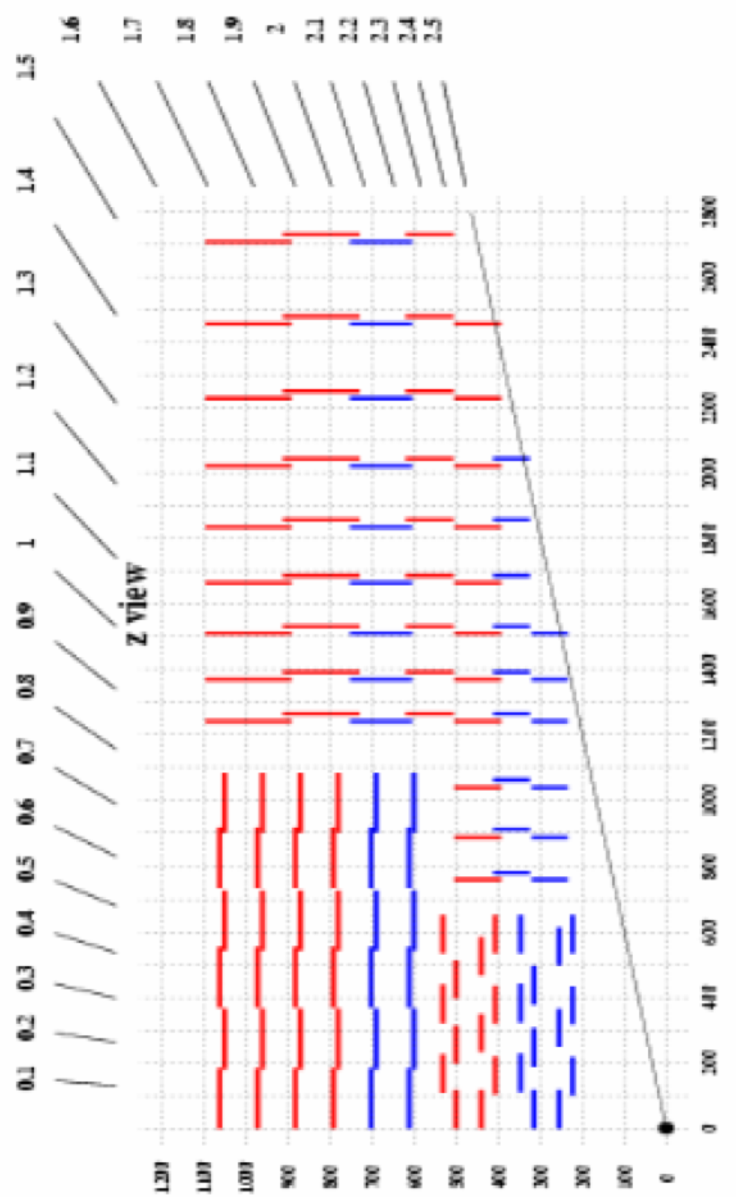

Figure (2-9): Schematic layout of the silicon microstrip detector.

resolution between 23–34 μm in the r-φ direction and 23 μm in z. The strip pitch is 80 μm on layers 1 and 2 and 120 μm on layers 3 and 4 in the TIB, leading to a single point resolution of 23 μm and 35 μm, respectively. In the TID the mean pitch varies between 100 μm and 141 μm.

2. **Tracker Outer Barrel (TOB):** TOB surrounds the TIB/TID, and it has outer radius 116 cm. TOB consists of 6 barrel layers of 500 μm thick micro-strip sensors with strip pitches of 183 μm on the first 4 layers and 122 μm on the layers 5 and 6. The TOB the first 2 layers provide a “stereo” measurement in both r-φ and r-z coordinates. The stereo angle is 100 mrad and the single-point resolution varies from 35–52 μm in the r-φ direction and 52 μm in z.

3. **The Tracker EndCaps (TEC):** TEC+ and TEC- (where the sign indicates the location along the z axis) cover the region 124 cm < |z|< 283 cm and 22.5 cm < |r| < 113.5 cm. Each TEC is composed of 9 disks. The innermost 2 rings and the fifth ring of the TEC have ”stereo” modules. The thickness of the sensors is 320 μm for the 3 innermost rings of the TEC and 500 μm for the rest of the TEC.

The entire silicon strip detector consists of almost 15 400 modules, table (2.3), which are mounted on carbon-fibre structures and housed inside a temperature controlled outer support tube. The operating temperature will be around “-20° C”.

Table 2.3: Detector types in the silicon tracker

part	No. detectors	Thickness (μm)	Mean pitch (μm)
TIB	2724	320	81/118
TOB	5208	500	81/183
TID	816	320	97/128/143
TEC	2512	320	96/126/128/143
TEC(2)	3888	500	143/158/183

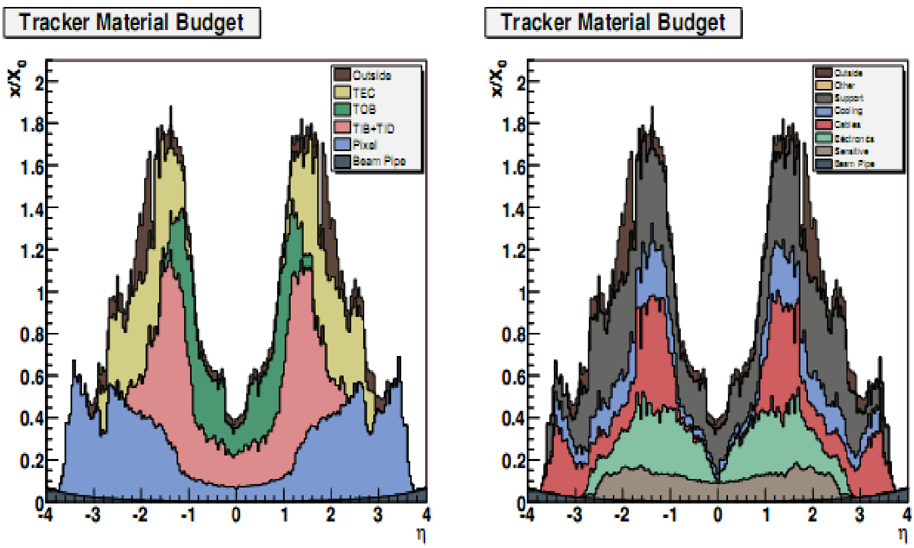

Figure (2-10): Material budget in units of radiation length as a function of pseudorapidity η for the different sub-detector (left panel) and broken down into the functional contributions (right panel). [53]

Figure (2-10) shows the material budget of the CMS tracker in units of radiation length. It increases from 0.4 X_0 at η ≈ 0 to about 1.8 X0 at |η| ≈ 1.4, beyond which it falls to about 1 X_0 at |η| ≈ 2.5.

(2-2.2) Electromagnetic Calorimeter (ECAL):

The electromagnetic calorimeter (ECAL) of the CMS detector is designed to identify and measure the energy of electrons, positrons and photons through their electromagnetic cascades in matter. The ECAL is a hermetic homogeneous calorimeter made of 61200 lead tungstate $(PbWO_4)$ crystals mounted in the central barrel part, closed by 7324 crystals in each of the two endcaps. Each EndCap is divided in two halves, or Dees, which contain 3662 crystals each, and is placed at about 315 cm far from the interaction point.

The pseudorapidity covers the region |η| < 3. The ECAL barrel is coverage the region |η| < 1.479 with a granularity of $\Delta\eta \times \Delta\phi = 0.0174 \times 0.0174$, corresponding to a $(PbWO_4)$ crystal face of 2.2 x 2.2 cm, is equal to Moliere radius of $(PbWO_4)$. The endcaps covers the region (1.48 < |η| < 3.0), and the granularity increases to a maximum value $\Delta\eta \times \Delta\phi = 0.05 \times 0.05$. The length of $(PbWO_4)$of crystal is 23 cm in the barrel and 22 in the endcaps regions. An overview of the CMS ECAL layout is shown in Figure (2-11).

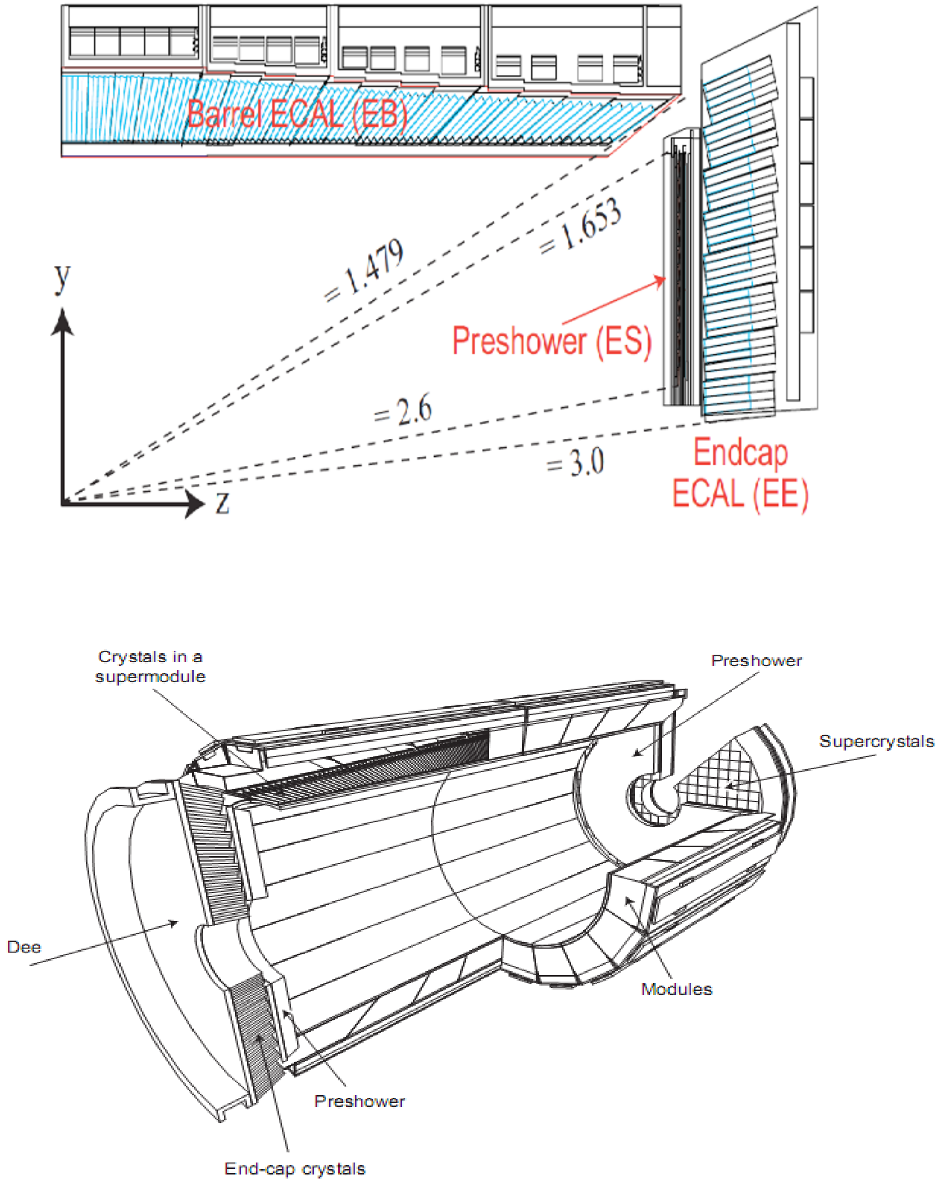

Figure (2-11): Layout of the CMS electromagnetic calorimeter showing the arrangement of crystal modules, supermodules and endcaps, with the preshower in front.

ECAL Preshower

A preshower detector is placed in front of the endcap crystals. Avalanche photodiodes (APDs) are used as photodetectors in the barrel and vacuum phototriodes (VPTs) in the endcaps. The use of high density crystals (8.28 g/cm^3) has allowed the design of a calorimeter which is fast, has fine granularity and is radiation resistant, all important characteristics for the LHC environment.

The main importance of the PreShower detector (PS) is to identify neutral pions via the photon detection, detected in the endcaps in the pseudorapidity region $1.653 < |\eta| < 2.6$. Also, it helps in improving the position measurement of electrons and photons with high granularity, and helps in identification of electron, and provide better separation power between electrons and photons. The total thickness of PreShower detector is 20 cm, and consists of a two layer sampling calorimeter: lead radiators initiate electromagnetic showers from incoming electron or photons whilst silicon strip sensors placed after each radiator measure the deposited energy and the transverse shower profiles.

(2-2.3) The Hadron Calorimeter (HCAL):

The hadron calorimeter (barrel and endcaps) put behind the tracker and electromagnetic calorimeters The purpose of the CMS hadronic calorimeter is detecting hadrons that have passed through the ECAL without interaction and the tails of the showers of hadrons that started their shower in the ECAL. The HCAL is consisting of for main parts as shown is figure (2-12), the HCAL Barrel (HB), the HCAL EndCaps (HE), the HCAL Outer (HO) and the forward HCAL (HF).

1. **Hadron Barrel (HB):**

HB is a sampling calorimeter covering the region |η| < 1.3. HB consists of two half barrels sections (HB+ and HB-) each composed of 18 identical azimuthal wedges, resulting in a segmentation of $\Delta\eta \times \Delta\phi = 0.087 \times 0.087$. The wedges are constructed out of flat brass absorber plates aligned parallel to the beam axis. The innermost and outermost plates are made of stainless steel for structural strength. This division is shown in Figure (2-13) (right), each wedge is segmented into four azimuthal angle (ϕ) sectors.

2. **Hadron EndCaps (HE):**

The Hadron calorimeter Endcaps cover the partial pseudorapidity region 1.3 < η < 3. This region contains about 34 % the particles produced in the final state. The hadron calorimeter is located inside the superconducting magnet 3.8T, so the material used must a non- magnet material, also it must have a maximum number of interaction lengths and contain good mechanical properties, and reasonable cost. So C26000 cartridge brass is chosen. The granularity of calorimeters $\Delta\eta \times \Delta\phi = 0.087 \times 0.087$ for |η| < 1.6 and $\Delta\eta \times \Delta\phi = 0.17 \times 0.17$ for |η| ≥ 1.6.

3. Hadron outer (HO):

The hadron outer (HO) is extended outside the solenoid coil with a tail catcher for $|\eta| < 1.3$. The reason is that the combination of the electromagnetic barrel and hadron barrel detectors does not provide sufficient containment for hadron showers. The HO is constrained by the geometry of the muon system. Figure (2-14), shows the position of HO layers in the rings of the muon stations in the overall CMS setup. The HO is used to identify and to measure the late starting shower energy after hadron barrel HB. The HO utilises the solenoid coil as an additional absorber equal to ($1.4/\sin\theta$) interaction lengths and is used to identify late starting showers and to measure the shower energy deposited after HB.

4. Hadron forward calorimeter (HF):

After about 11 m form interaction point, the hadron forward calorimeter is located. The HF covers the pseudorapidity region $3 < |\eta| < 5$. Its design was driven by the very high flux of particles in the forward direction which causes large doses of radiation in this sub-detector. Iron absorber plates and quartz fibers allow the detection of Cerenkov radiation caused a relativistic secondary particles and are sufficiently radiation hard. However they mainly measure the electromagnetic shower component and therefore their energy resolution is not high. The forward calorimeter will experience unprecedented particle fluxes. On average, 760 GeV per proton-proton interaction is deposited into the two forward calorimeters, compared to only

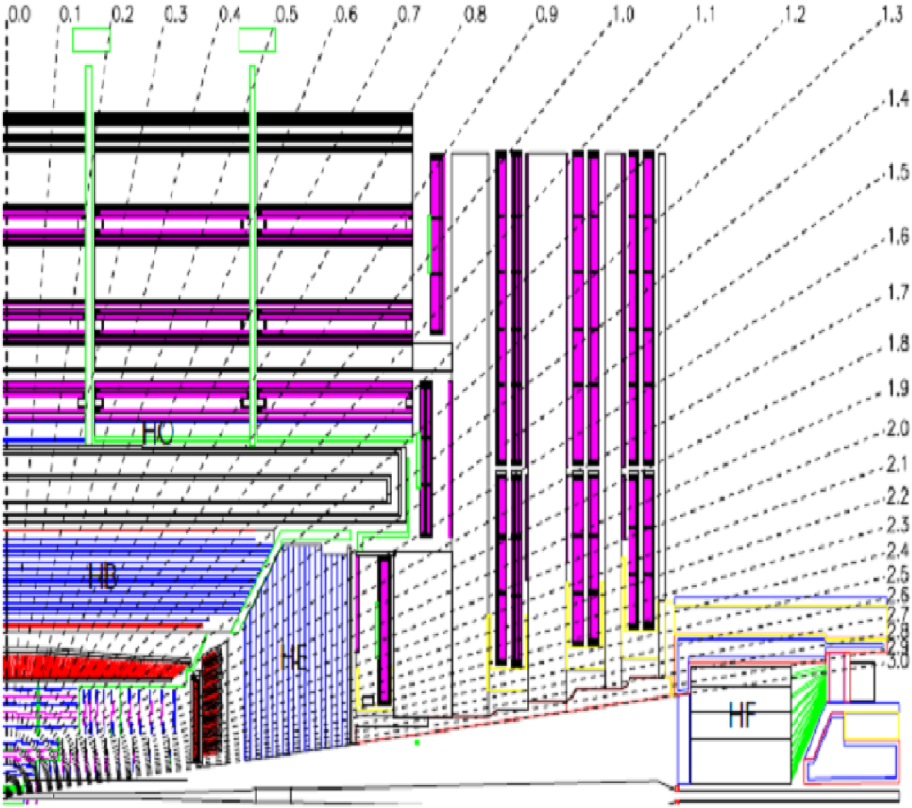

Figure (2-12): Slice through the CMS hadronic calorimeter. It consists of the Hadronic Barrel (HB), the Hadronic Endcap (HE), the Hadronic Outer (HO) detector and the Hadronic Forward (HF) detector.

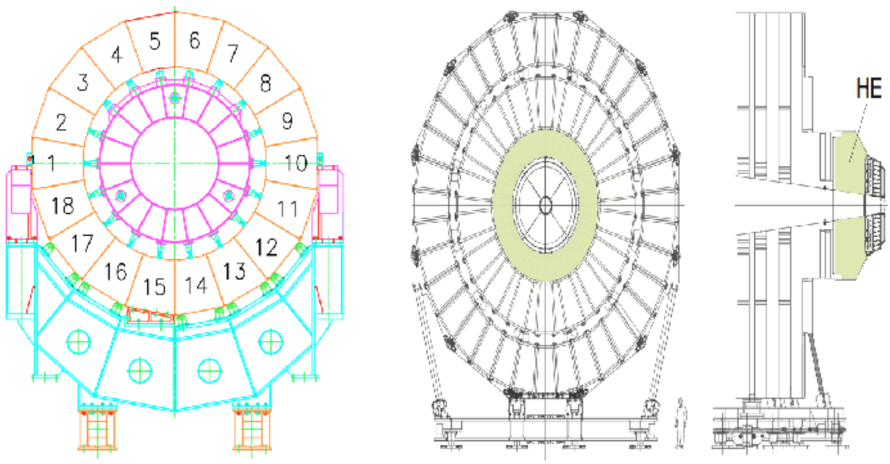

Figure (2-13): Drawing of the r-φ section illustrating the division in wedges of the HB (left). Drawing showing the HE position in the CMS apparatus in the r-φ section (middle) and r-z section (right).

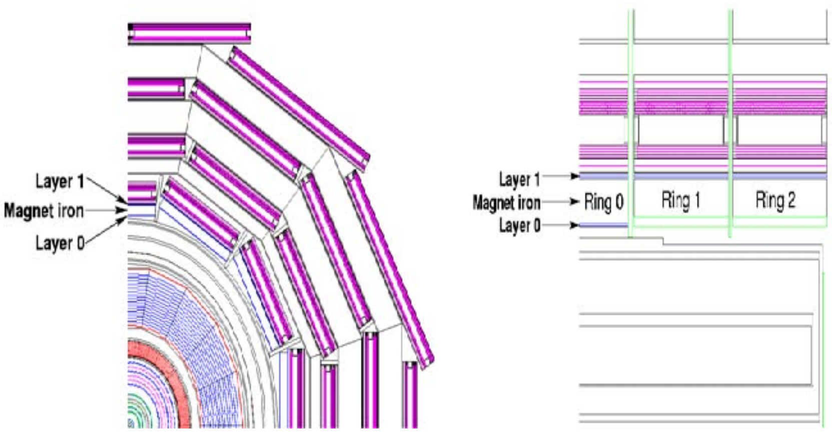

Figure (2-14): Longitudinal and transverse views of the CMS detector showing the position of HO layers

100 GeV for the rest of the detector. Moreover, this energy is not uniformly distributed but has a pronounced maximum at the highest rapidities. At $|\eta| = 5$ after an integrated luminosity of 5 x10^5 pb^{-1}(≈ 10 years of LHC operation), the HF will experience 10 MGy. The charged hadron rates will also be extremely high. For the same integrated luminosity, inside the HF absorber at 125 cm from the beam-line, the rate will exceed 10^{11}per cm^2 [53].

The main importance of the calorimetric system in CMS is the identifications of isolated electrons and photons, and the reconstruction of jets. It also plays a central role in the CMS trigger. The measurement of the overall energy flow in events allows the identification of particles that do not interact with the detector material through an imbalance of the momentum sum of all reconstructed objects, called missing transverse energy (MET). These particles can for example be neutrinos that are produced in weak interactions such as the decay of heavy quarks or bosons. Especially in events that contain supersymmetric particles, large amounts of missing energy are expected.

(2-2.4) Superconducting magnet:

CMS detector uses a superconducting magnet (figure (2-15)) with maximum field 3.8 T. It a free bore with diameter 6 m. At the full operational current of 19.14 kA, 2.6 GJ of energy are stored in the magnetic field. It is constituted of 4 layers of NbTi superconductor, the coil is lying in a vacuum chamber and a cryogenic system keeps it at a temperature of 4.45 K. A return yoke ring surrounds and supports the central magnet, conducts the magnetic flux lines and at the same time is part of the muon system subdetector. The yoke is constituted of five iron rings, each one 1.8 m thick, in the barrel and six disks in the end caps. The yoke layers are spaced by the muon chambers as is shown in Figure (2-4). The main features of superconducting magnet are:

- Due to the number of ampere-turns required for generating a field of 4 T (41.7 MA-turn), the winding is composed of 4 layers, instead of the usual 1 (as in the Aleph and Delphi coils) or maximum 2 layers (as in the ZEUS and BaBar coils);

- The conductor, made from a Rutherford-type cable co-extruded with pure aluminium (the s-called insert), is mechanically reinforced with an aluminium alloy;

- The dimensions of the solenoid are very large (6.3-m cold bore, 12.5-m length, 220-t mass).

If charged particle is placed under influence of magnetic field B, the transverse momentum of charged particle, Pt, in this case is given by

$$Pt = 0.3 \times B\,(\text{Tesla}) \times R(\text{meter}) \qquad \text{GeV}$$

Where, R is the radius of curvature for the charged particle.

The distance between ECAL surface and interaction point is about 1.3 m, the minimum Pt of the charged particle reached ECAL surface is

$$Pt = (0.3 \times 4 \times 1.3)/2 = 0.8 \text{ GeV in CMS detector.}$$

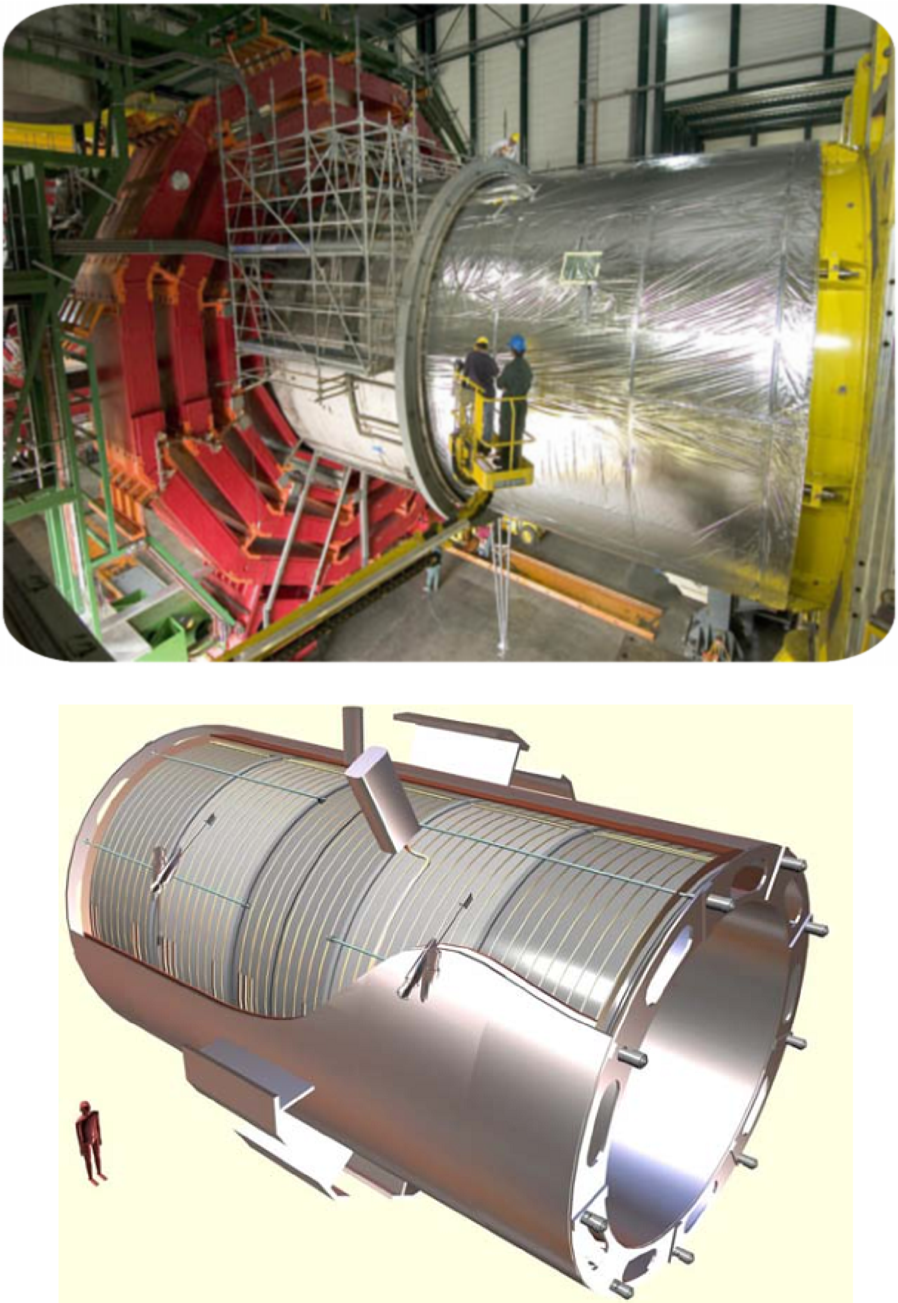

Figure (2-15): CMS detector uses superconducting magnet.

(2-2.5) The Muon System:

The muons are the easiest particles to detect in hadron collider experiments; therefore they play a crucial role in the early stage of LHC. The precise and robust measurement of muons was of central importance from the early stages of the CMS planning. Figure (2-16) show the overview of the outer CMS muon system. The role of the muon system is muon identification, momentum measurement and triggering. So, it is required to have a very quick response of the passage of muons in order to provide information to the CMS trigger system.

Actually, muons produced at the center of the detector are measured two times independently: in the inner tracking system and after the coil in the muon system illustrated in Figure (2-16). Measurement of the momentum of muons using only the muon chambers in one of the 5 wheels.

system is essentially determined by the muon bending angle at the exit of the 3.8 T coil, taking the interaction point as the origin of muon.

Due to the geometry of CMS, the muon system also has a cylindrical barrel section and two endcaps. The system consists of three independent gaseous subdetectors, utilizing different detection technologies which complement each other:

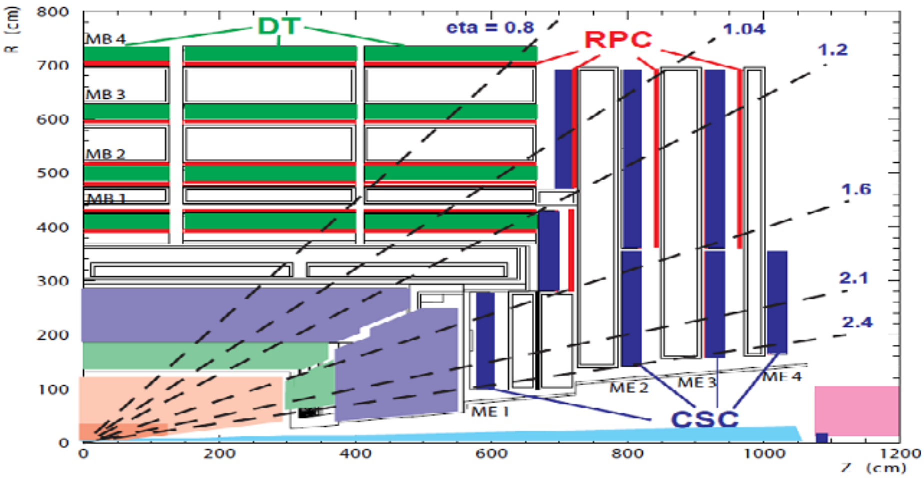

Figure (2-16): Design overview of the outer CMS muon system.

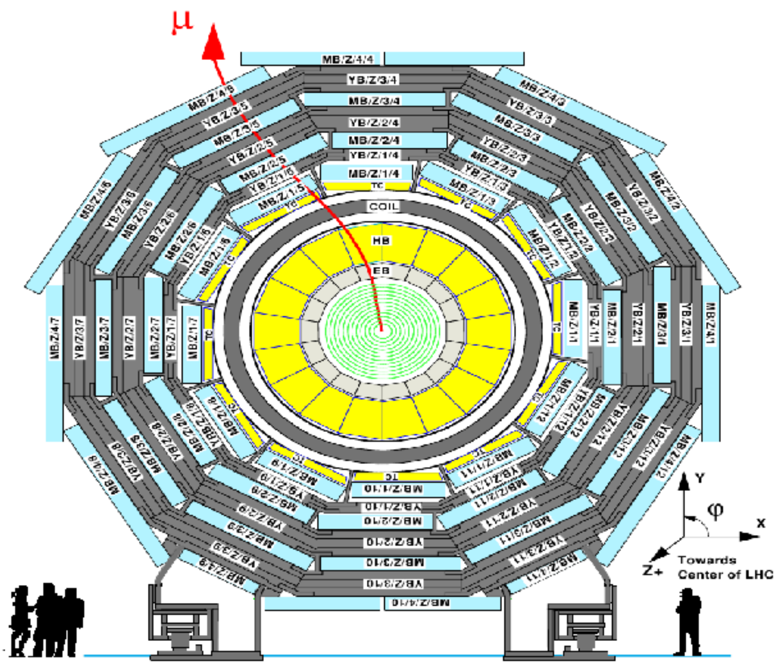

Figure (2-17): Schematic layout of the CMS barrel muon DT.

1. **Drift Tube (DT):**

The DT system is located in barrel region, and covers the pseudorapidity region $|\eta| < 1.2$. This region has some features, the neutron-induced background is small, the muon rate is low, and the 3.8-T magnetic field is uniform and mostly contained in the steel yoke, drift chambers with standard rectangular drift cells are used. This Muon Barrel assemblage is shown in Figure (2-17). The first 3 stations each contain 8 chambers, in 2 groups of 4 and measure the muon coordinate in the r-φ bending plane, and 4 chambers which provide a measurement in the z direction, along the beam line. The fourth station does not contain the z-measuring planes. The 2 sets of 4 chambers in each station are separated as much as possible to achieve the best angular resolution.

2. **Cathode Strip Chambers (CSC):**

In the EndCap region, the rate of muon is high, the magnetic field is large but is not uniform, and the background levels are high, so the muon system uses cathode strip chambers (CSC). The CSC is located in the pseudorapidity range $0.9 < |\eta| < 2.4$. The CSC has some characteristics of such as fast response time, fine segmentation, and radiation resistance. The two endcaps have 4 stations from CSCs in each one, with chambers sited perpendicular to the beam line and interspersed between the flux return plates.

In the region $0.9 < |\eta| < 1.2$, the barrel and endcap overlap, thus both DT and CSC provide the muon detection. In the $1.2 < |\eta| < 2.4$ region the muon detection is provided by 3 or 4 CSC stations.

3. **The Resistive Plate Chambers system (RPC):**

The RPCs is in barrel and EndCap. The RPC are gaseous parallel-plate detectors with the feature to provide, besides a discrete spatial resolution, also a time resolution comparable to the scintillators one. The RPC is able to measure the time of an ionising event with a much better resolution than the interval (25 ns) between two consecutive LHC bunch crossing (BX). For this reason a muon trigger based on RPC has been developed. The RPCs provide a fast, independent and highly-segmented trigger with sharp Pt threshold over a large portion of the rapidity range ($|\eta| < 1.6$) of muon system. Both the DTs and RPCs contribute independently to the L1 trigger system.

(2-2.6) Data Acquisition and Triggering:

The LHC is expected to deliver proton-proton collisions every 25 ns, corresponding to a crossing frequency of 40 MHz. Approximately 10^9 interactions are expected to be produced every second at design luminosity. This event rate is by far not recordable or computable, hence, the trigger system has to achieve a rejection factor of nearly 10^6, leading to a event rate of O(100) which is possible to store and analyzing offline. The reduction of rate is achieved by two steps; Level-1 (L1) trigger and high level trigger (HLT), respectively. The level-1 Trigger consists of custom-designed, largely programmable electronics, whereas the HLT is a software system implemented in a filter farm of about one thousand commercial processors.

1. **Level-1 trigger:**

The L1 trigger is the first step to reducing the number of events by selecting only 50-100 kHz of the most interesting events, using hardware algorithms that can make decisions in less than 3.2 μs. The L1 trigger uses coarsely segmented data from the calorimeters and the muon system to identify photons, electrons, muons, jets and missing transverse energy.

The full detector data is kept in pipeline memories in the detector front-end electronics until the L1 decision is reached; the L1-Accept is then propagated to the various subdetectors through the Timing, Trigger and Control (TTC) system.

The L1 Trigger has local, regional and global components. Trigger Primitive Generators (TPG) identify energy deposits in calorimeter trigger towers and track segments or hit patterns in muon chambers. Regional Triggers use this information to determine ranked and sorted trigger objects. The Global Calorimeter (GCT) and Global Muon Triggers (GMT) determine the highest-rank calorimeter and muon objects across the entire experiment and transfer them to the Global Trigger (GT) which combines the information and decides whether to keep the event or not, Level-1 Trigger architecture. The information flow for the Calorimeter and Muon triggers is shown in Figure (2-18).

Calorimeter trigger

The Trigger Primitive Generators (TPG) makes up the first or local step of the Calorimeter Trigger pipeline. For triggering purposes the calorimeters are subdivided in trigger towers In the region up to $|\eta| = 1.74$, The division in trigger towers has a granularity of each trigger tower has an $\eta \times \phi = 0.087 \times 0.08$. This subdivision is illustrated in Figure (2-19) for a quarter of the r-z section. The TPG electronics and the calorimeter read-out are integrated. The calorimeter trigger TPGs sum the transverse energies measured in ECAL crystals and HCAL towers. The TPG information from 7000 trigger towers are transmitted through high-speed serial links to the Regional Calorimeter Trigger (RCT) which detects signatures of regional electron, photon, tau and jet candidates as well as missing and total transverse energy. The position and transverse energy of these regional candidates are then fed to the GCT which determines the top four highest-rank isolated and non-isolated calorimeter trigger objects across the entire detector, total transverse energy, missing transverse energy, jet counts, jet E_T sums (H_T) and the missing hadronic transverse energy and sends them to the GT.

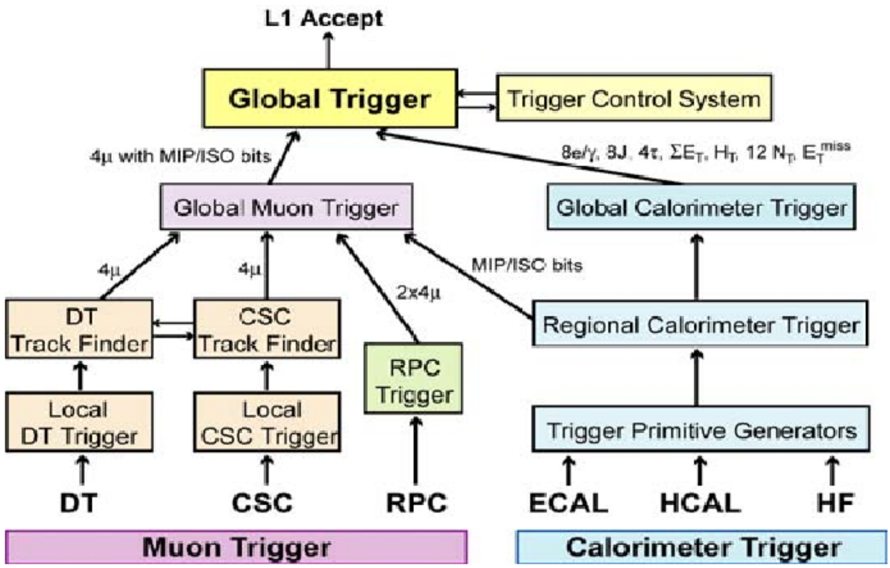

Figure (2-18): Level-1 Trigger architecture. The information flow for the Calorimeter and Muon triggers is shown.

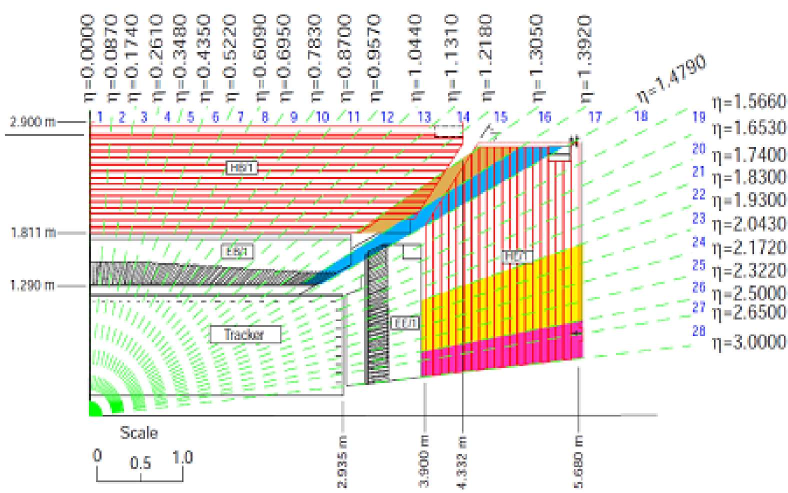

Figure (2-19): Drawing of a quarter of the r-z CMS section showing the division in trigger towers of the calorimeters.

Muon trigger

All sub detectors of muon system (barrel Drift tube (DT), Endcaps Cathode Strip Chamber (CSC), and Resistive plate chamber (RPC)) are using in Level-1 trigger. The Regional Muon Trigger consists of the DT and CSC Track Finders, which join segments to complete tracks and assign physical parameters to them. The RPCs, with their excellent timing resolution, provide an independent source of track candidates and send its hits information to the CSC in order to improve the resolution and possible ambiguities. The initial pseudorapidity is covered by the muon trigger is $|\eta| = 2.1$ at the startup of LHC.

Trigger Control System

The Trigger Control System (TCS) is responsible to controls the delivery of the L1A signals, depending on the status of the sub-detector read-out systems and the data acquisition. The status is derived from signals provided by the Trigger Throttle System (TTS) and from the status of front – end Emulators. The TCS is also responsible for generating synchronization and reset commands, and controls the delivery of test and calibration triggers. TCS partitioning permits groups of subdetectors main components to operate independently during setting-up, test or calibration phases. Local trigger control is foreseen for the subdetector operation in standalone mode (test beam mode). It uses the Timing, Trigger and Control distribution network, which is interfaced to the LHC machine.

Data Acquisition and High Level Trigger

Once the Level-1 Trigger decides to accept an event, the accepted signal is distributed to the Front-End Driver (FED), which copy the data from the buffer into the Data Acquisition (DAQ) system.

The Event Builder subsystem is dedicated to assemble the events which are stored on over 600 FED and distributes them to the HLT processing nodes. The DAQ system also allows the execution of additional analysis modules that perform quality and integrity checks on the processed data, called Data Quality Monitoring (DQM). These provide quick feedback and allow detection of various detector problems without waiting for the process of offline reconstruction.

The HLT is in charge to reduce the event rate 100 kHz of a factor10^3. It is a software system implemented in a filter farm of about one thousand commercial processors. This allows for full flexibility and optimization of the algorithms. Data read from subdetectors are assembled by a builder unit and then assigned to a switching network that dispatches events to the processor farm. The algorithm implementation is fully software; therefore it could be modified and improved without any hardware intervention.

It is organized in three virtual layers: the so called Level2 considers only muon and calorimetry information, the Level 2.5 uses also information coming from the Pixel detector, and Level3 takes information also from the whole tracking system. Each step selects the number of events which are processed by the successive level. The track reconstruction makes the Level3 very time expensive, and since the measurement precision is not required to the trigger, it is performed on a limited number of hits and only in the interesting regions. This layered structure provides reliable algorithms needed to perform the last step of the online selection. Event by event, the HLT code runs on a single processor and has to make a decision in 300 ms, and in order to be efficient it has to manage to reject not interesting events as soon as possible. The data-flow between trigger and data acquisition is depicted in Figure (2-20).

(2-3) The Worldwide LHC Computing Grid

The Worldwide LHC Computing Grid (**WLCG**) project is a global collaboration of more than 170 computing centers in 36 countries, linking up national and international grid infrastructures. The mission of the WLCG project is to provide global computing resources to store, distribute and analyse the ~25 Petabytes (25 million Gigabytes) of data annually generated

by the Large Hadron Collider (LHC) at CERN on the Franco-Swiss border.

The infrastructure built by integrating thousands of computers and storage systems in hundreds of data centers worldwide enables a collaborative computing environment on a scale never seen before.

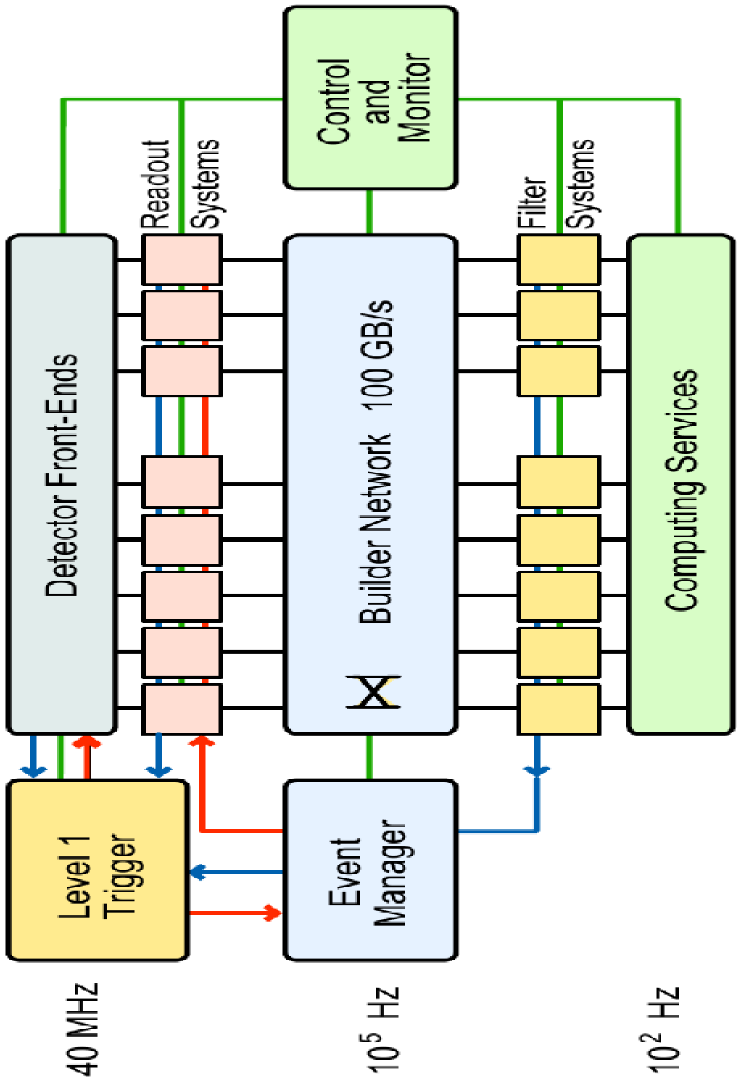

Figure (2-20): Working principle of the trigger and data acquisition system.

WLCG serves a community of more than 8,000 physicists around the world with near real-time access to LHC data, and the power to process it.

The WLCG is now the world's largest computing grid. The WLCG is composed of four levels, or “Tiers”, which are made up of the computer centers. The tiers are called Tier 0, Tier 1, Tier 2 and Tier 3. These tier sites process, store and analyse all the LHC data between them. Figure (2-21) the computing centers available to CMS around the world.

(2-4) CMS Computing:

The CMS application software performs a variety of event processing, selection and analysis tasks. The main concept of the CMS data model is the Event. The Event provides access to the recorded data. The Events are physically stored as ROOT files.

The Event is used by a variety of physics modules which performs a well-defined function of reconstruction or analysis of the Event. The modules execute independently from one another. The CMS Application Framework is illustrated in Figure (2-22).

The CMS computing system has several event formats with differing levels of detail and precision in order to achieve the required level of data reduction.

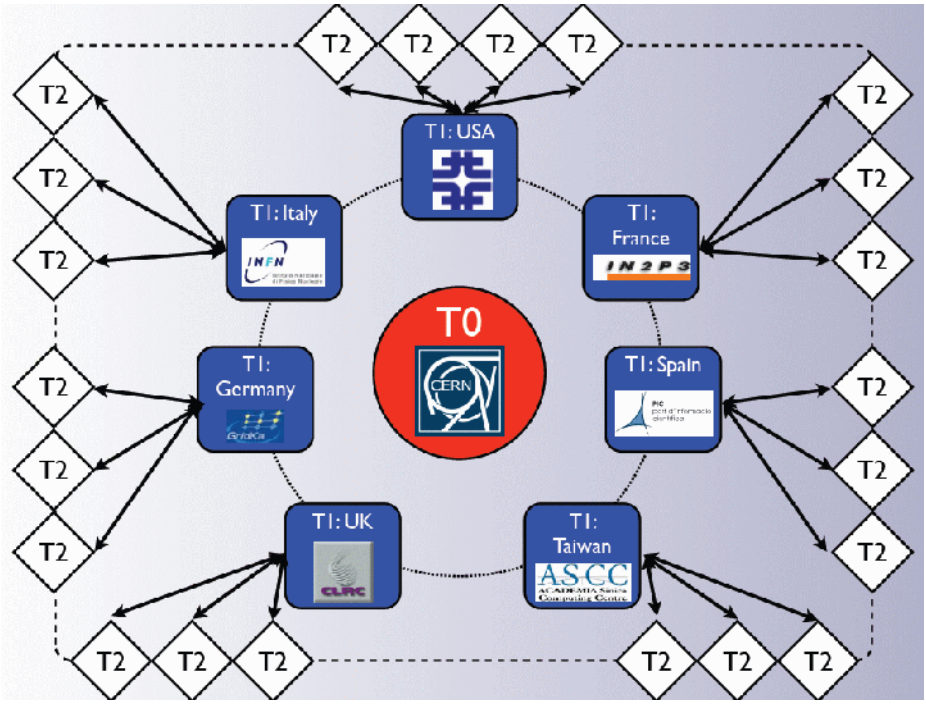

Figure (2-21): The computing centers available to CMS around the world

The RAW format contains the full recorded information from the detector and also a record of the trigger decision. The RAW data is permanently archived in safe storage with size of 1.5 MB/event. The size of simulated events is slightly different is about 2 MB/event. This different comes from Monte Carlo truth information.

Reconstructed (RECO) data is derived from RAW data and should provide access to reconstructed physics objects for physics analysis in a convenient format. Event reconstruction is structured in several algorithms which include detector- specific filtering and correction of the the digitized data; cluster- and track-finding; primary and secondary vertex reconstruction; and particle ID [53]. The resulting RECO events contain high-level

physics objects such as jets, muons, electrons, b-jets, etc. The RECO format is about 250 kB/event.

The Analysis Object Data (AOD) is the compact analysis format and is produced by filtering of RECO data. The AOD data format is about 50 kB/event.

The computing system with such a scale could not be hosted entirely at one site. Thus, the CMS offline computing system is arranged in four tiers. The twoTier-0 centre at CERN and the other one in the Wigner Research Centre for Physics in Budapest, Hungary accepts data from the CMS Online.

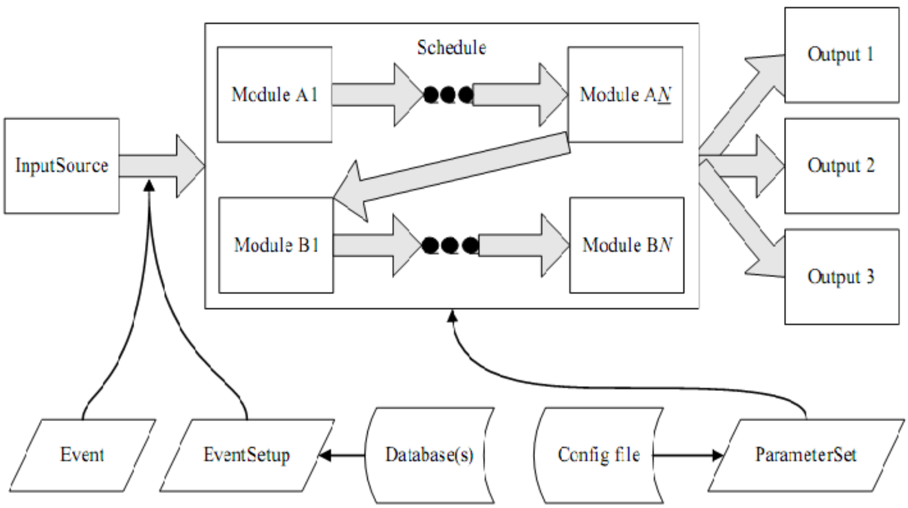

Figure (2-22): The CMS Application Framework with modules.

DAQ System and performs prompt first pass reconstruction. The Tier-0 distributes raw and processed data to a set of large Tier-1 centers in CMS collaborating countries. These centers provide services for data archiving, reconstruction, calibration, skimming and other data-intensive analysis tasks. A more numerous set of Tier-2 centers provide capacity for analysis, calibration activities and Monte Carlo simulation. Tier-3 centers provide interactive resources for local groups and additional best effort computing capacity for the collaboration. The majority of CMS users rely upon Tier-2 or Tier-3 resources as their base for analysis [56]. The data flow between CMS Computing Centers is illustrated in Figure (2-23).

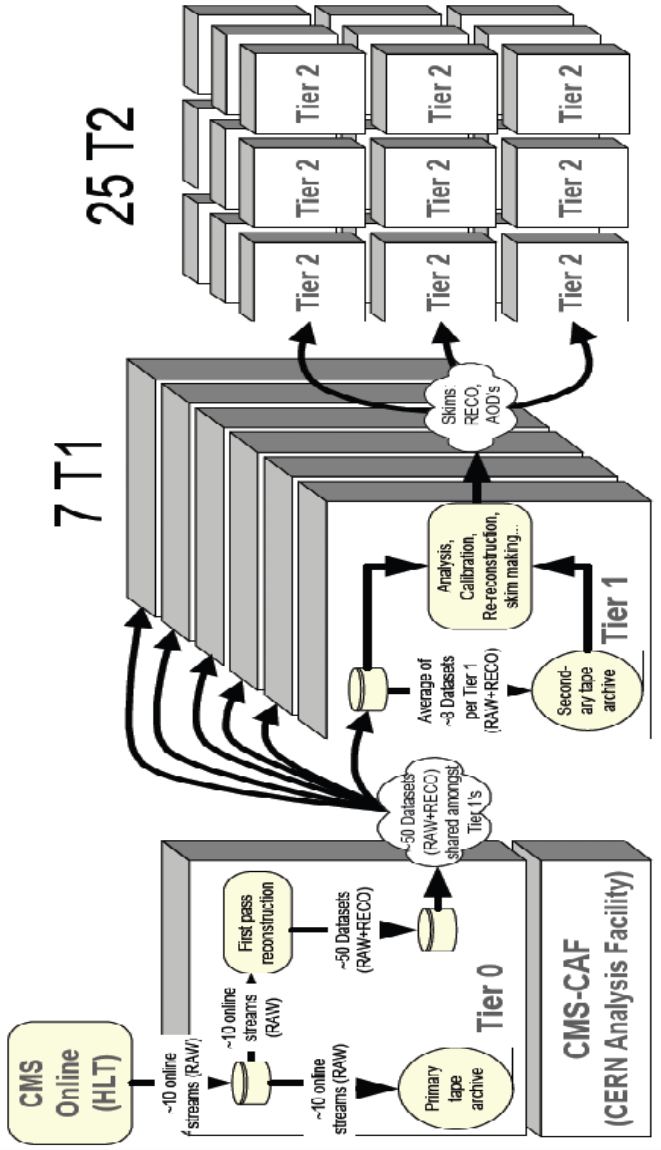

Figure (2-23): the flow of CMS detector data through the tiers.

Chapter 3

Dataset, MC, Events and track selections

(3-1) Introduction:

This chapter is common chapter for all work in this thesis. It contains several sections, the first section is containing the information about data and Monte Carlo (MC) were used in these analyses. After that, we introduce the information about minimum bias trigger and high multiplicity trigger. In the last sections, we summarized the event selections, such as Removal of scraping events, and vertex selection, and also summarized all track selections were used.

(3-2) Data and MC samples

The dataset used in this analysis is:

/MinimumBias/Run2010B-Apr21ReReco-v1/RECO

The runs and luminosity sections used for the analysis have been certified by the corresponding JSON files:

Cert_136033-149442_7TeV_Apr21ReReco_Collisions10_JSON.txt

Where Json file is the file that describes which luminosity sections in which runs are considered good and should be processed. In CMS, these files are in the JSON format. (JSON stands for Java Script Object Notation). To find the most current good luminosity section files in JSON format,

MC Dataset for minbias:

- /MinBias_7TeV-pythia8/Winter10-START39_V8-v1/GEN-SIM-RECO

- /MinBias_TuneZ1_7TeV-pythia6/Summer10-START36_V10_TP-v1/GEN-SIM-RECODEBUG
- /MinBias_TuneD6T_7TeV-pythia6/Winter10-START39_V8-v1/GEN-SIM-RECO
- MinBias_TuneZ2_7TeV-pythia6/Fall11-NoPileUp_START44_V9B-v2/GEN-SIM-RECODEBUG
- /MinBias_Tune4C_7TeV-pythia8/Summer11-NoPU_START42_V11-v1/GEN-SIM-RECO
- /MinBias_TuneZ2star_HFshowerLibrary_7TeV_pythia6/Summer12-LowPU2010_DR42_NoPileUp_START42_V17C-v1/GEN-SIM-RECO

MC- High Multiplicity Events

- /castor/cern.ch/user/m/mohammed/MC_HighMutli_Pythia6_Z2/MC_HighMutli_Pythia6_Z2_new/
- /castor/cern.ch/user/m/mohammed/MinBias_Tune4C_7TeV-pythia8
- /castor/cern.ch/user/m/mohammed/MC_PYTHIA8/

(3-3) Triggering and Event Selection

The analysis of charged particle pseudorapidity distributions integrates over the total cross section of pp collisions. To minimize the bias imposed on such an analysis by the trigger strategy it is essential to optimize the trigger to accept a large fraction of the cross section. Further it is essential to study the relative contributions of single diffractive, double diffractive and non- diffractive collisions as well as the admixture of non-collision background such as beam gas interactions and beam halo.

(3-3.1) Trigger strategy for early collision runs

The trigger strategy of CMS detector for early collisions was significantly different from the nominal configuration. At start up the readout timing of the CMS detector elements and the trigger system has to be aligned. Since this timing has to be verified based collision data, only a limited number of trigger detectors were enabled to produce a L1 accept signal to prevent triggers firing early with respect to the beam crossing signal to start the readout too early and cause the event to be lost due the CMS trigger rules.

(3-3.1.1) Generating L1 Accept

For early collision data taking the CMS readout is triggered by a signal in any of the BSC segments Figure (3-1), coincident with a signal from either BPTX indicating a beam or a bunch crossing the IP.

(3-3.1.2) BPTX and BSC-based triggers

This section contains information concerning the use of the Beam Scintillator Counters (BSC) and the Beam Pick-up Timing eXperiment (BPTX), pickups as triggers for CMS and for this analysis. Signals from the Beam Scintillator Counters are used as minimum-bias triggers (based on the number of segments hit).

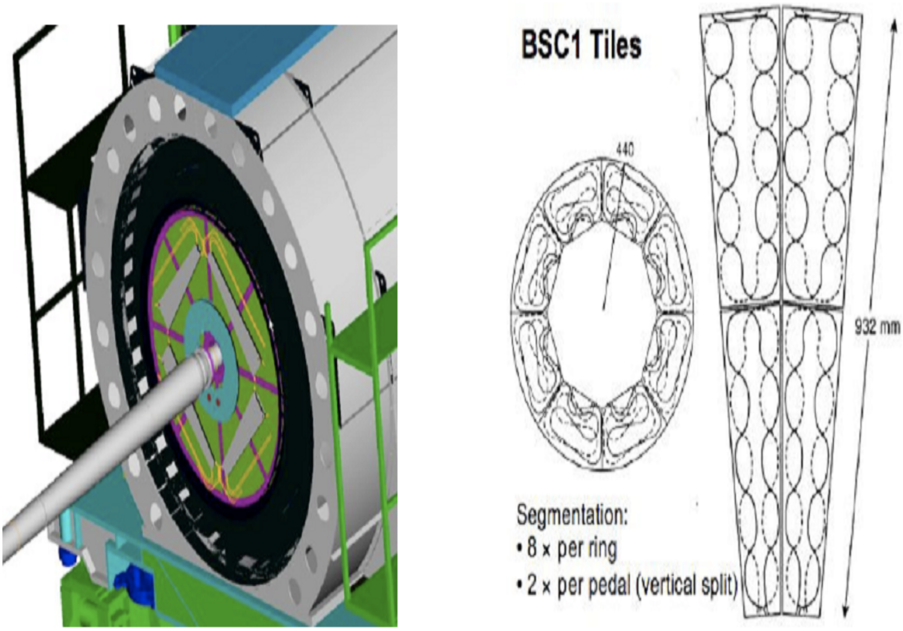

Figure 3.1: Location and schematic of BSC detector.

The most important trigger based on the BPTX is the Zero Bias trigger, which is the crossing of two filled proton bunches. There is also a trigger that requires only one filled and one empty bunch crossing; this is sometimes called ‘empty target’ trigger and will be used for corrections for beam gas and halo.

The main purpose of the BSC system is to provide collision/background monitoring information for CMS. Hence, the responsibility for its installation and commissioning lies with the BRM group. Besides the monitoring goals, signal pulses are also extracted from the readout of the BSC and BPTX detectors for triggering. The Global Trigger (GT) has 64 so-called technical trigger inputs (LVDS) to which simple signals (pulses) from the BSC and BPTX are routed. The required logic (fanning in the 32 individual BSC signals in logical “or”s and “and”s) for these signals before entering the GT is fully implemented. There are 8 technical and 4 extra algo trigger bits from the BSC, and 7 technical and 4 algo bits from the BPTX provided for the General Trigger.

The relevant trigger bits for this analysis are listed in table 1.

The list of L1 bit assignments can be found on the following two webpages:

1. https://twiki.cern.ch/twiki/bin/view/CMS/L1TechnicalTriggerBits
2. https://twiki.cern.ch/twiki/bin/view/CMS/L1ExternalConditions

The scintillators for the BSC1 station are mounted on the inner surface of the HF detectors on both sides of the IP. The flight time between the IP and BSC1 is 36.5 ns. The four segments in each 'outer' petal are grouped to two PMTs (PMT = photo-multiplier tube), providing a segmentation in two halves, one for each end. The scintillator rings provide eight signals on each side. This gives in total $2 * (8 + 8) = 32$ BSC1 channels.

Earlier measurements have shown a time resolution around 3 ns for these scintillators taken from the OPAL mini-plug detector. With the routing of the signal cables to the readout in USC55, a resolution around 5 ns is expected. The scintillators (BC408), read out through photo-multipliers via wavelength shifting fibers, are expected to provide 14 photo-electrons per traversing m.i.p.

The readout of the BSC counters is implemented using commercial electronics located in NIM and VME crates in rack S1E08. Signals from the PMT-s are discriminated and then combined using off-the-shelf logical NIM units (e.g. LeCroy) to implement the required coincidence logic and delays. This requires NIM to LVDS units for signal conversion in the end. The LVDS signals are routed to the GT rack via 4x2 wire commercial Ethernet cables.

Bit number	Bit mane	Description
34	L1Tech_BSC_minBias_OR	There is at least onehit in the BSC
36	L1Tech_BSC_halo_beam2_inter	beam2 halo, inter
37	L1Tech_BSC_halo_beam2_outer	beam2 halo, outer
38	L1Tech_BSC_halo_beam1_inter	beam1 halo, inter
39	L1Tech_BSC_halo_beam1_outer	Beam1 halo, outer
40	L1Tech_BSC_minBias_threshold1	At least one hit in time coincidence
41	L1Tech_BSC_minBias_threshold2	At least one hit in time coincidence

Table (3.1): BSC L1 bit assignments.

Segment	eff. (%)	segment	eff. (%)	segment	eff. (%)	segment	eff. (%)
+D1	97	-D1	97	+P1	96	-P1	97
+D1	97	-D1	95	+P1	98	-P1	96
+D1	97	-D1	96	+P1	95	-P1	98
+D1	97	-D1	95	+P1	97	-P1	97
+D1	96	-D1	97	+P1	99	-P1	98
+D1	96	-D1	97	+P1	99	-P1	99
+D1	95	-D1	97	+P1	97	-P1	98

Table (3.2): Measured efficiencies of the BSC segments. Mean: 96.3%. + and − stands for positive and negative z side from the IP. D and P mean disk (inner ring) and paddles (outer segments).

(3-3.1.3) BSC MIP efficiency measurement

The efficiency of the BSC scintillator segments was measured based on the measurement of the MIP peak in the scintillators. The measurement was done on the 26th and 29th of March, with circulating beams, just before the first collision data taking on 30th of March, 2010. The BSC has a standalone readout based on CAEN VME V1721 8-bit digitizers (called ADC-s in this section). These can measure the pulse shape in 2 ns steps. All the ADC's are calibrated with a known pulse shape, so the ADC counts and the voltage is related to each other with < 1% precision. The ADC's use 6dB attenuators as well, and those are also calibrated using pulse generators and measuring them with oscilloscope, also with < 1% precision.

In the measurement, self-triggering was used with 5 ADC unit threshold. After pedestal subtraction, the peak (-to pedestal) height was measured for each pulse. Part of these pulses are from MIPs crossing the scintillator layer, while other part is from noise (including ambient gamma radiation and cosmics). The ADC's have the BPTX signal connected, so events can be selected off-line where BPTX was firing, giving the MIP distribution. The random coincidences from noise were subtracted carefully (small contribution), using off-time signals with respect to the BPTX signal. The result of the MIP measurement for a typical segment is plotted in Figure (3-2).

The final, subtracted MIP peak was fitted with a convolution of the Landau and Gaussian distribution, see Figure (3-2), and the relative fraction of its area above the

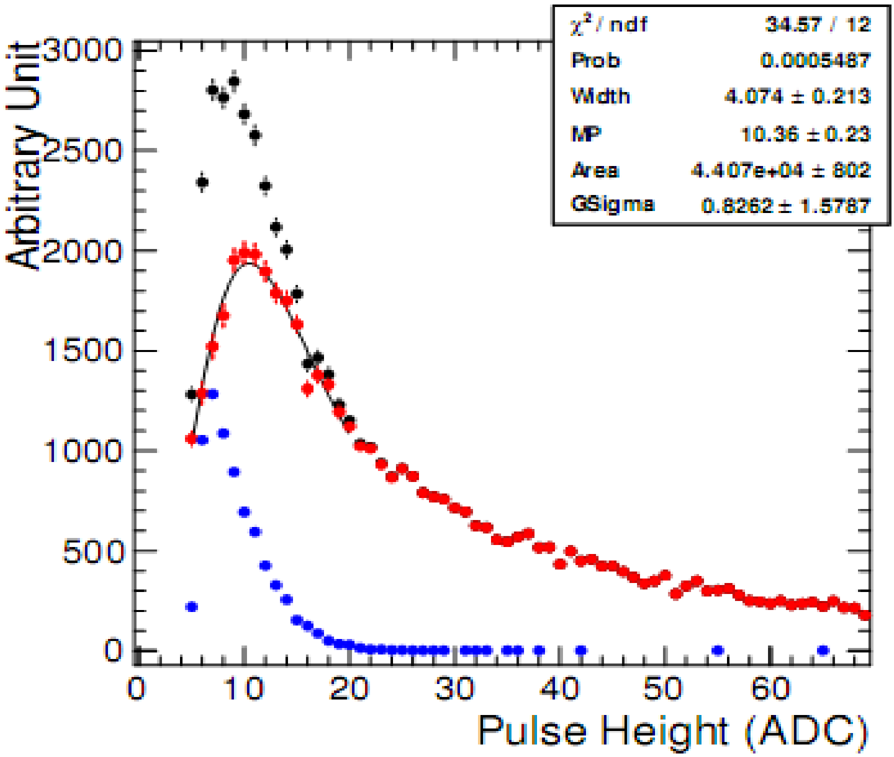

Figure (3-2): MIP peak in the BSC. Black: all signals, blue: background (out-of-time), red: subtracted spectrum, line: Landau Gaussian fit.

hardware discriminator threshold set for triggering, which was 31 ± 1 mV (that was converted to ADC units for each channel separately using the calibration, and the fit function was integrated above this ADC value corresponding to the threshold). The resulting segment efficiencies are given in Table (3.2).

(3-4) Triggering on High Multiplicity Events

With the goal of studying the properties of the high multiplicity pp collisions, a dedicated high multiplicity trigger was designed and implemented into the official pp HLT menu since October, 2009. It aims to capture all the high multiplicity events without any prescale factor at a rate of 1-2Hz. The high multiplicity trigger mainly involves two levels:

1. Level-1: existing L1 seed ”L1 ETT60” (algorithm bit 63) is used to filter out events with scalar sum of total transverse energy (L1 ETT) at L1 over the entire CMS calorimetry (ECAL, HCAL and HF) to be above 60 GeV.

   OR

   existing L1 seed ”L1 ETT100” (algorithm bit 100) is used to filter out events with scalar sum of total transverse energy (L1 ETT) at L1 over the entire CMS calorimetry (ECAL, HCAL and HF) to be above 100 GeV.
2. High-Level Trigger: in the high-level triggering, pixel tracking becomes available that provides us the most precise tracking information possible online. However, naive counting of number of reconstructed pixel tracks would lead to significant contributions from pileup

events, instead of high multiplicity produced from a single collision. Our trigger path proceeds with the following sequences: after reconstructing the pixel tracks with p T > 0.4 GeV/c and track origin within a cylindrical region of 10.5 cm in half length and 0.5 cm in transverse radius, a divisive online pixel vertexing algorithm is executed with pixel tracks as its seeds. The path is then followed by an HLT filter that counts the number of pixel tracks with kinematic cuts of |η | < 2 and p T > 0.4 GeV/c, within a distance of 0.12 cm to the best found pixel vertex (associated with highest number of tracks). zvtx of pixel vertices is also required to be within a range of ±10 cm.

The first high multiplicity trigher path used in CMS was HLT PixelTracks Multiplicity70 . This trigger was enabled to trigger on events with at least 70 online pixel tracks produced without prescale factor. As luminosity increases, in order to maintain a reasonable HLT output rate and not lose any high multiplicity events, a second HLT path HLT PixelTracks Multiplicity85 was added , a third HLT path HLT path HLT PixelTracks Multiplicity100 was added because the change in luminosity.

(3-5) Event Selections

(3-5.1) Trigger

The triggers used in this analysis are:

1. HLT_L1Tech_BSC_minBias
2. HLT_PixelTracks_Multiplicity100

(3-5.2) Base event selection

In order to select real collision events and to clean them from instrumental or beam related noise sources, the following selection has been applied:

(3-5.3) Removal of scraping events

During the LHC commissioning phase, it was observed that in some bunch crossings there was an anomalously large occupancy in the pixel detector, which resulted in a large number of reconstructed fake tracks. These events were identified as being the result of beam particles traversing the pixel detector longitudinally. We reject this type of events by requiring that the fraction of high-purity tracks in all events with more than 10 tracks is greater than 25%.

(3-5.4) Vertex selection

In order to further constrain the event selection to identify the collision events, a selection based on the reconstructed primary vertex properties is implemented. The selection is based on NDF of the vertex, the distance in the x-y plane ρ and the vertex z coordinate.

The official recommendations from the tracking group are applied:

- Reject fake vertices.
- NDF (number of degree of freedom) > 4
- $\rho \leq 2$ cm
- Vertex $|z| \leq 24$ cm.

(3-6) Track Selections

For each selected event the reconstructed track collection needs to be cleaned up from undesired tracks, namely secondaries and background (e.g. combinatorial background and beam halo associated tracks). Fake tracks coming from mis-reconstruction are removed by requiring tracks to pass the highPurity selection. The full track selections are used in this analysis listed below:

- quality mask passes high purity requirement: trk.quality(”highPurity”)
- relative pT uncertainty below 5%: trk.ptError()/trk.pt()< 0.05
- at least 5 hits on the track: trk.numberOfValidHits>= 5
- eta range: |eta| < 2.4
- absolute impact parameter cuts: abs(trk.dz)<0.2 && abs(trk.d0<0.2)
- relative impact parameter cuts: abs(dxy/dxyerror) < 3 && abs (dz/dzerror) < 3
- Minimum track pt cut: Pt > 0.3, 0.4, 0.5, or 0.6 GeV.

In the case of the final selection, d0 and dz refer to the impact parameter calculated with respect to the primary vertex, e.g. trk.d0(vtx.position()). Also, dxyerror and dzerror refer to the sums in quadrature of the transverse and longitudinal track impact parameter uncertainties and the respective uncertainties on the vertex position. Figure (3-3) shows some parameters we are using in track selections. To verify from all above selections, the two dimensions plots between Genparticle and reco tracks should be introduce, Figure (3-4).

To deal with MC at generator level, we have to apply cuts, these cuts are:

1. Charged particle: gen. charge=!0
2. Stable particle: gen. status==1
3. Eta cut: abs(gen.eta) < 2.4

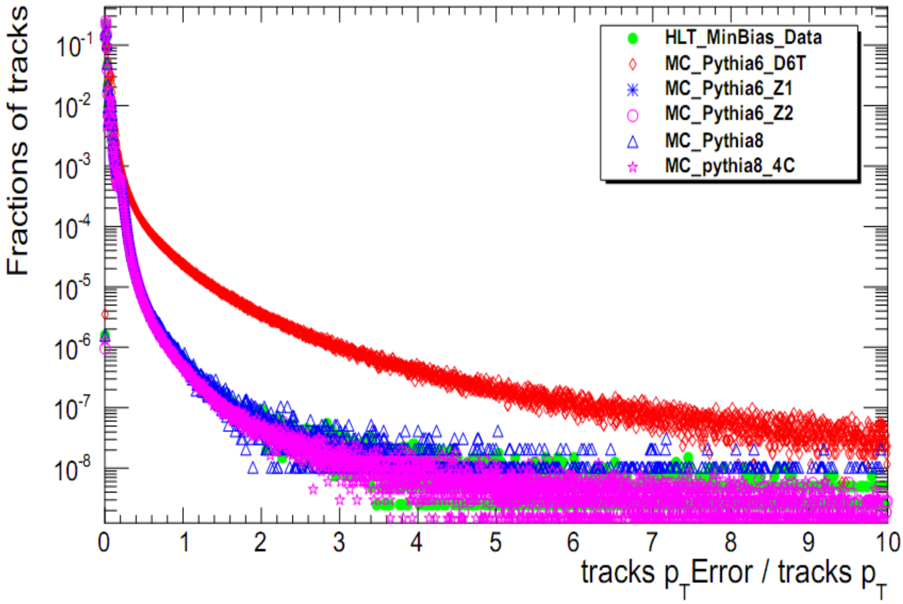
Fractions of tracks
HLT_MinBias_Data
MC_Pythia6_D6T
MC_Pythia6_Z1
MC_Pythia6_Z2
MC_Pythia8
MC_pythia8_4C
tracks p_TError / tracks p_T

(A)

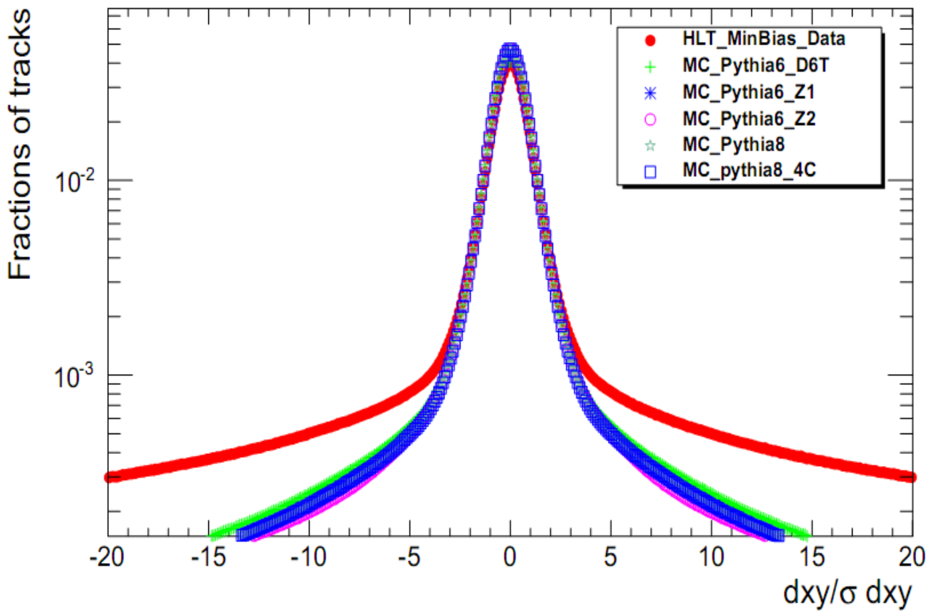
Fractions of tracks
HLT_MinBias_Data
MC_Pythia6_D6T
MC_Pythia6_Z1
MC_Pythia6_Z2
MC_Pythia8
MC_pythia8_4C
dxy/σ dxy

(B)

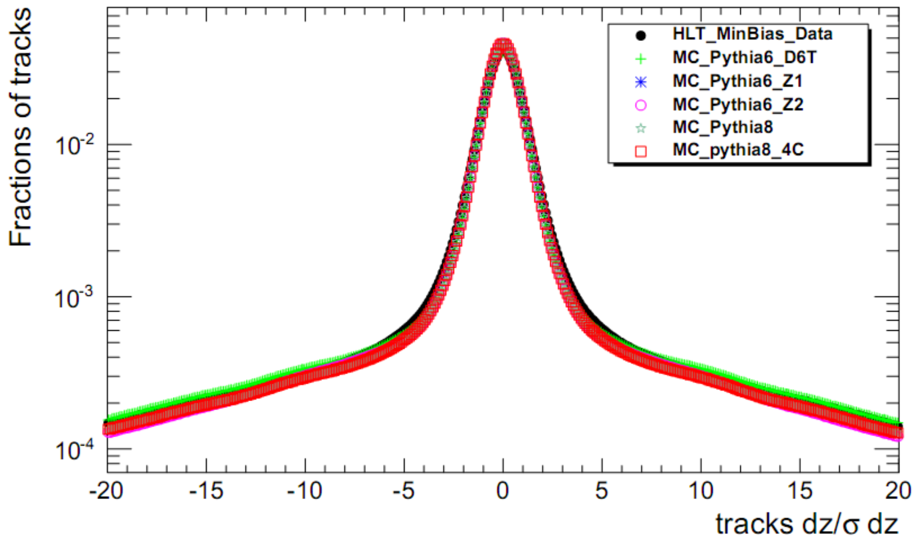

(C)

Figure (3-3): some track parameters, and the selections applied before no applying any cuts for tracks (A, B, C).

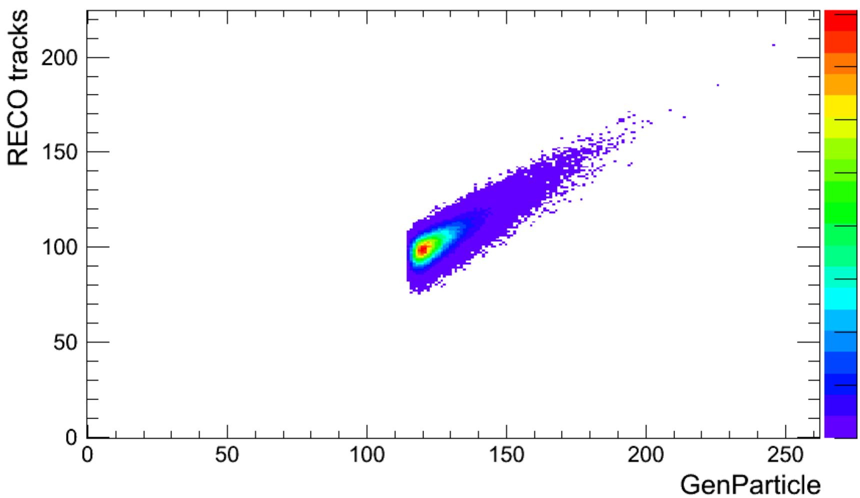

Figure (3-4): two dimensions plots between Generator particle (particle produced at generator level) and reco tracks.

Chapter 4

Maximum Track Density

(4-1) Introduction and previous work:

Events with large number of charged particles in small intervals of (pseudo)rapidity in hadronics collisions have been known from a long time [57-61]. The importance of high density fluctuations in rapidity and pseudorapidity space is increasing when trying to study the connection between the hot hadronic matter and heavy ions collisions.

The events with large fluctuations in small interval with respect to (pseudo)rapidity are called ring-like or spike events, because in a single event many particles tend to be emitted with a similar polar angle, but randomly distributed in azimuthal angle. As a consequence, the event is characterized by a ring of particles in the plane perpendicular to the collision axis. Some early cosmic-ray experiments showed evidence for large concentrations of particles in small pseudorapidity regions of single events.

In the UA5 [62] experiment, operated at CERN proton anti-proton collider at energy E_{CM} = 540 GeV, the collaborators studied events with 15 or more charged particles produced within windows of 0.5 with respect to pseudorapidity. This observation had led to the suggestions that such spikes might be the result of formation in the primary hadron-hadron collisions of a "hot-spot" of matter, possibly in the quark-gluon phase.

In the NA22 collaboration [63] experiment studied the K^+ p, π^+ p and pp collisions at $\sqrt{s} = 22 GeV$. The collaborators in this experiment showed an interesting result on the maximum track density within narrow rapidity interval $\Delta y = 0.1$. Figure (4-1), shows the result of this experiment, the straight line is the fitting for the corresponding data, the fit function was Taken to be $dN/dn = a.e^{-b}$ the values of a, and b are listed in table (4.1). From Figure (4-1) we can see an event at n = 10 and this point is far from the fit line. The collaborator referred to that event as an anomalous event.

Ames –Bologna –CERN –Dortmund –Heidelberg -Warsaw (ABCDHW) Collaboration [71], this experiment studied the collisions between proton - proton at energies $\sqrt{s} = 31.44$ and $\sqrt{s} = 62$ GeV. They studied the maximum track density within narrow windows with different widths 0.1, 0.25, 0.5 and 0.75 with respect to rapidity, Figure (4-2). The main results of that experiment were events with a very high concentration of particles within a small rapidity interval have been observed at ISR, the distributions of these events looks exponential in the range 0.1 to 0.75 units of rapidity for the window size. There seems to be a weak energy dependence of the slopes at fixed window size, and the average quantity $< n^{max} >$ was found to rise linearly with total charge multiplicity.

J.B. Singh and J.M. Kohli, in 1990 [65], studied the maximum track density in the NA23 collaboration. This collaboration studied p-p collisions at energy $\sqrt{s} = 360$ GeV. Figure (4-3a) shows the distribution of events with maximum charged particle density n within a rapidity window $\Delta y = 0.1$. The number of events decreases with increasing n. The experimental

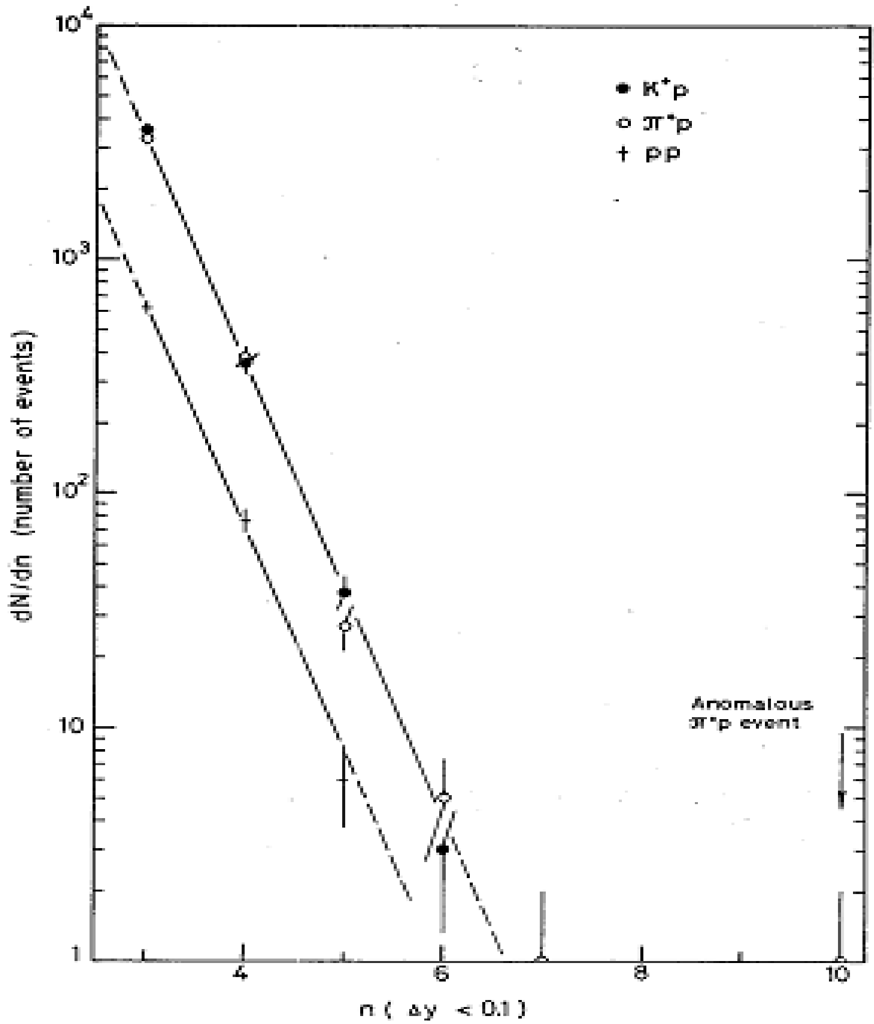

Figure (4-1): The distribution of number N of events with a maximum of charged particles inside 0.1 unit of rapidity (n) for K^+ p, π^+ p and pp collisions at $\sqrt{s} = 22 \ \ GeV$. The straight lines correspond to fits of the π+ p and pp data to exponentials. (NA22 Collaboration) [63]

Table (4.1): the values of fitting parameters a, and b [63].

Collisions	a	b	chi2/ndf
π^+ p	7.77 ± 0.12	1.04 ± 0.01	40/5
K^+ p	8.03 ± 0.11	1.02 ± 0..1	17/5
Pp	8.56 ± 0.30	0.97 ± 0.03	1/5

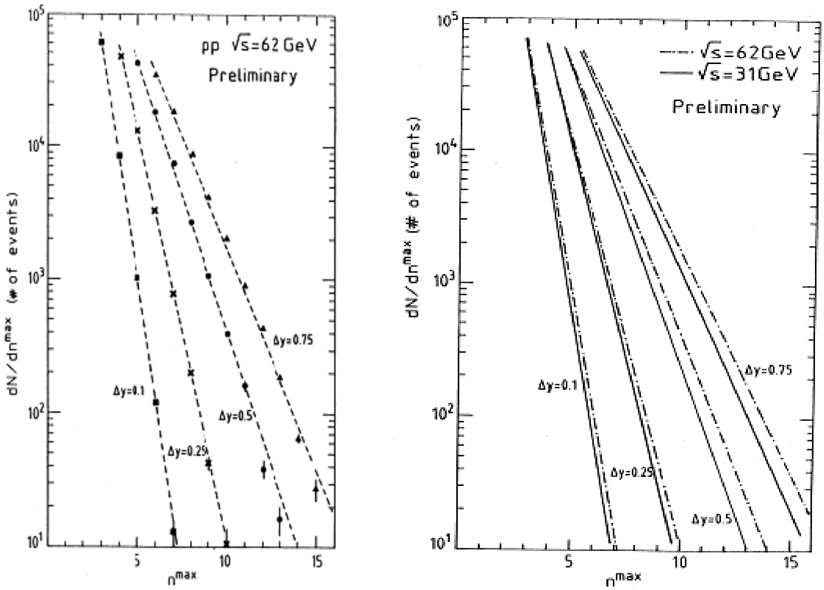

Figure (4-2): (a) The distribution of number N of events with a maximum of n^{max} charged particles inside Δy units of rapidity at $\sqrt{s} = 62$ GeV. **(b)** Comparison between fitted slopes to distributions of the kind shown in fig. (a) for different energies.[64]

results have been fitted with an exponential form dN/dn = a exp(-bn). The value of exponential slope b is 2.13±0.07.

Figures (4-3b), and (4-3c) represent the behavior of dN/dn and a function of n in the case of events having n_{ch} $+n_{ch} + neutral\ particle\ (\pi^{0,s}\ and\ V^{0,s})$. All the events follow the exponential fall of dN/dn with n. No event has been observed showing strong clustering of particles in a rapidity interval as small as Δy= 0.1 beyond the exponential fall. However, the maximum local particle density (charged and neutral) as high as 110 particles per unit rapidity interval has been observed.

The important conclusions of that were; there are no events having very large density fluctuation in a sample of 26100 pp interactions at 360 GeV/c. The average maximum track density in a given rapidity interval (Δy = 0.1 and 0.5) rises linearly with n_{ch} for a large energy range $\sqrt{s} = 22 - 900$ GeV. The maximum particle density within fixed rapidity window is exponential, and no single event with a very large number of tracks in a given rapidity interval has been observed beyond the exponential fall.

EHS/NA22 Collaboration [66], in this experiment, the collaborators made comparison between spike productions in pp and π^+ p / K^+ p collisions at energy 205-360 GeV. They found that, the spike-center pseudorapidity distributions for pp collisions reveal in two prominent peaks, Figure (4-4), and the effect of ring-like events in hadron production is somewhat similar to the ring-like structure of accompanying radiation of short-lived particles (the “dead-cone effect”).

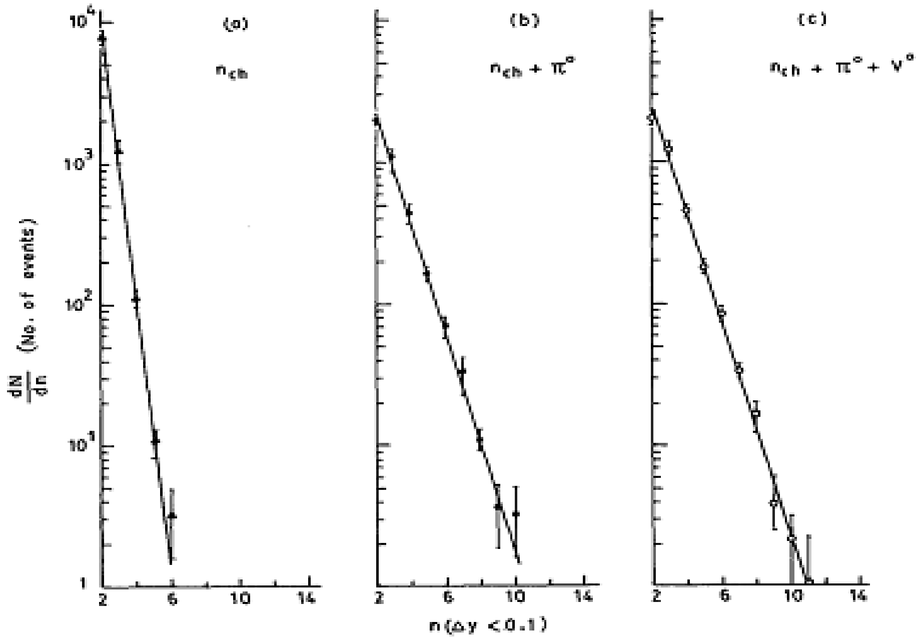

Figure(4-3): The distribution of the number of events N as a function of maximum charged particle density n inside the $\Delta y = 0.1$ window for (a) charged particles, (b) charged particles + $\pi^{0,s}$, (c) charged particles + $\pi^{0,s}$ + $V^{0,s}$ [65]

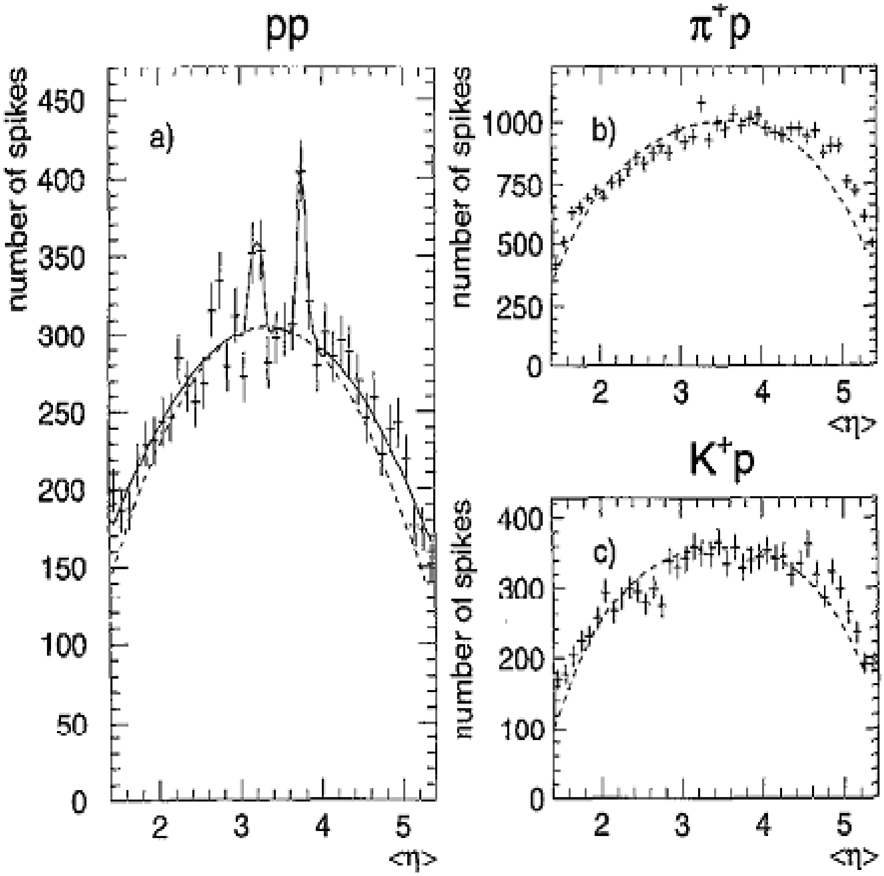

Figure (4-4): Spike-center pseudorapidity distribution for pp interactions at 205, 250 and 360 GeV/c **(Fig. 4-4a),** for π+ p interactions at 250 GeV/c **(Fig. 4-4b)** and for K+p interactions at 250 GeV/c **(Fig. 4-4c).** The solid line in Fig. 4-3a is a result of the fit; the dashed lines are the FRITIOF predictions. [66]

In September 2010, the CMS Collaboration presented to the scientific community one of the most intriguing observations to emerge from the first data running period of the Large Hadron Collider (LHC) [67]. It showed the appearance of a pronounced structure, named the ridge, when studying two-particle angular correlations of proton-proton (pp) collisions with a centre of mass energy ($\sqrt{s}$ = 7 TeV). Interestingly, this effect was not expected as it had not previously been observed in any Monte Carlo simulations. The result was obtained by utilizing the two dimensional $\Delta\eta - \Delta\varphi$ correlation functions, where firstly, $\Delta\eta$ is defined as the difference in pseudorapidity, η, between the two charged particles ($\eta = -\ln(\tan(\theta/2))$), θ is defined as the polar angle with respect to the beam axis). Secondly, $\Delta\varphi$ is the difference between the two charged particles azimuthal angle φ.

Figure (4-5) shows the main, 2-D two-particle correlation plots from the CMS study, with (a) and (b) showing the analysis performed upon minimum bias events, in the transverse momentum range of $p_T > 0.1$ GeV/c and then a specific range of 1 GeV/c < p_T < 3 GeV/c respectively. Plots (c) and (d) on the other hand present the same, but in this case high multiplicity events have been analysed instead of minimum bias, specifically events which had a multiplicity, N, > 110. While plots (a, b & c) showed nothing that deviated from theoretical models, plot (d) clearly displayed an unexpected ridge structure in the long-range, near-side region. It was discovered by studying long-range azimuthal correlations for 2.0 < $\Delta\eta$ < 4.8 and $\Delta\varphi \approx 0$,

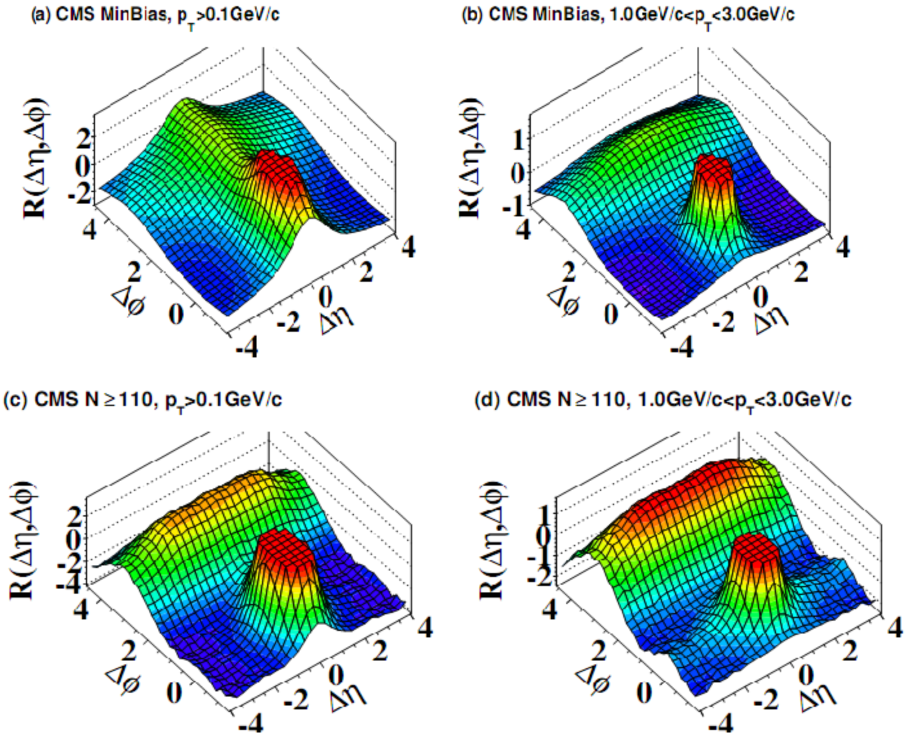

Figure (4-5): 2-D two-particle correlation functions for 7 TeV pp (a) minimum bias events with $p_T > 0.1$ GeV/c, (b) minimum bias events with $1 < p_T < 3$ GeV/c, (c) high multiplicity (and only appeared in these high multiplicity events, in the aforementioned intermediate transverse momentum $1 < p_t < 3$ GeV/c . $N_{track}^{offline} \geq 110$) events with $p_T > 0.1$ GeV/c and (d) high multiplicity ($N_{track}^{offline} \geq 110$) events with $1 < p_T < 3$ GeV/c. The sharp near-side peak from jet correlations is cut off in order to better illustrate the structure outside that region.

This type of correlation had not been observed in pp collisions before, and therefore no physical origin was described by CMS along with the observation. Yet, what made the result very interesting was that it was reminiscent of such a correlation observed in data collected by experiments at the Relativistic Heavy Ion Collider (RHIC); whose main aim is to create and study the state of matter known as Quark Gluon Plasma (QGP): a (locally) thermally equilibrated state of matter in which quarks and gluons are deconfined from hadrons [68-70].

In the present work, we are studying the maximum track density in small intervals vary between 0.1 and 0.5 with respect to (pseudo)rapidity. The data was collected by CMS experiment in 2010 RunB is used in this analysis.

(4-2) Datasets, Monte Carlo, Events and Tracks Selections:

The dataset is using in this analysis:

/MinimumBias/Run2010B-Dec22ReReco_v1/RECO

The runs and luminosity sections used for the analysis have been certified by the corresponding JSON files:

Cert_136033-149442_7TeV_Dec22ReReco_Collisions10_JSON_v4.txt

MC for Minbias

- /MinBias_7TeV-pythia8/Winter10-START39_V8-v1/GEN-SIM-RECO
- /MinBias_TuneZ1_7TeV-pythia6/Summer10-

START36_V10_TP-v1/GEN-SIM-RECODEBUG

- /MinBias_TuneD6T_7TeV-pythia6/Winter10-START39_V8-v1/GEN-SIM-RECO
- /MinBias_Tune4C_7TeV-pythia8/Summer11-NoPU_START42_V11-v1/GEN-SIM-RECO
- /MinBias_TuneZ2star_HFshowerLibrary_7TeV_pythia6/Summer12-LowPU2010_DR42_NoPileUp_START42_V17C-v1/GEN-SIM-RECO

MC- High Multiplicity Events

- /castor/cern.ch/user/m/mohammed/MC_HighMutli_Pythia6_Z2/MC_HighMutli_Pythia6_Z2_new/
- /castor/cern.ch/user/m/mohammed/MinBias_Tune4C_7TeV-pythia8
- /castor/cern.ch/user/m/mohammed/MC_PYTHIA8/

The events are collected by HLT_PixelTrackMultipicity100 and HLT_L1Tech_BSC_minBias, separately. Events containing particles from LHC machine-induced backgrounds, such as beam halo and beam gas, are rejected by requiring that the fraction of high quality tracks be at least 25% in events with more than 10 tracks [64]. Events with more than one vertex, the highest multiplicity vertex is taken. The criteria of selecting vertex is: number of the degrees of freedom (ndof) has to be greater than 4, reconstructed primary vertex (PV) that falls within $\pm$ 24 cm window along the beam axis and a radius of ρ<0.15 cm in the transverse plane relative to the average vertex position over all the events.

For selected events the reconstrued tracks are needed to clean from undesired tracks; secondaries and background (e.g. combinatorial background and beam halo associated tracks). Fake tracks coming from mis-reconstruction are removed by requiring tracks to pass the highPurity [72] selection, minimum transverse momentum 0.4 GeV, minimum number of valid hits 5. Secondary decays are removed by requiring that the impact parameter significance $d0/\sigma(d0)$ and significance of z separation between the track and primary vertex $dz/\sigma(dz)$ each to be less than 3. In order to remove tracks with poor momentum measurement, we require the relative uncertainty of the momentum measurement $\sigma(p_T)/p_T$ to be less than 5%. All parameters $d0$, $\sigma(d0), dz$, and $\sigma(dz)$ are calculated with respect to vertex.

(4-3) Unfolding

In high energy physics, measurements of physical characteristics of produced particles, such as multiplicity, angular distributions, track density, etc are usually distorted and transformed by three effects:

- ***Limited acceptance:*** The probability to observe a given event, the detector acceptance, is less than 1. The acceptance depends on the kinematical variable *x*.
- ***Transformation:*** Instead of the quantity *x* a different, but related quantity *y* is measured. The transformation from *x* to *y* can be caused by the non-linear response of a detector component.

- ***Finite resolution:*** The measured quantity y is smeared out due to the finite resolution (or limited measurement accuracy) of the detector. Thus there is only a statistical relation between the true kinematical variable x and the measured quantity y.

The really difficult effect in the data correction for experimental effects, or data transformation from y to x is the finite resolution, causing a smearing of the measured quantities. So, it is very difficult to make comparisons of the data obtained using different detectors with each other.

For solving this problem, ideally, a two- variable function describing the response of detector is used, so that the actual measured distribution can be considered as a convolution of this function with true one. This in general leads to an integral equation for true distribution. The solving of this integral (unfolding) requires discretization, leading to a system of linear equations.

In high energy physics applications, the above approach is usually replaced by a discrete Monte Carlo simulation of the measurement process, resulting directly in a system of linear equations for the underlying true discrete distribution. In this case all the above difficulties are aggravated by statistical and possibly systematic errors in the response matrix itself.

For avoiding all these difficulties, it is advisable to fold the theoretically predicted true distribution with the estimated response matrix, and comparing the folded theoretical spectrum with the measured one. This method is stable and may be useful in certain cases, but is useless if one want to make a comparison between various experiments, or if the functional form of the distribution is unknown.

Mathematically, the relation between the distribution f*(x)* of the true variable *x*, to be determined in an experiment, and the measured distribution *g(y)* of the measured quantity *y* is given by the integral equation,

$$g(y) = \int A((y, x) f(x)\, dx \qquad (4.1)$$

The above equation called Fredholm integral equation of the first order. Where, the resolution function *A(y, x)* is describing the response of detector. For a given value $x = x_0$, the function $A(y, x_0)$ describes the response of the detector in the variable y for the value x_0. The target is determination the distribution *f(x)* from measured distributions *g(y)* this is called unfolding. Unfolding requires the knowledge of the resolution function *A(y, x)*, i.e. all the effects of limited acceptance, transformation and finite resolution. When we consider the usual case where *x* and *y* are both represented by histograms, the equation (4.1) change to

$$\nu_i = \sum_{j=0}^{M} R_{ij}\mu_j \qquad i = 1, \ldots, N \qquad (4.2)$$

Where $\mu = (\mu_1, \ldots \ldots, \mu_M)$ gives the expectation values for the histogram of y and $\nu = (\nu_1, \ldots \ldots, \nu_N)$ gives the expected number of events in bins of the observed variable *x*. The actual data are given as a vector of numbers n $= (n_1, \ldots \ldots, n_N)$.

The response matrix R has the interpretation as a conditional probability:

$$R_{ij} = P(\,observed\ in\ bin\ i \mid true\ value\ \ in\ bin\ j).$$

For all possible bins observed value *i*,

$$\sum_{i=1}^{N} R_{ij} = R\ (observed\ anywhere \mid true\ value\ in\ bin\ j) = \varepsilon_j \qquad (4.3)$$

This gives the efficiency ε_j which depends in general on the bin *j* of the true of histogram.

Bayes' Theorem

Bayesian Unfolding has been used since 1994 and was introduced by G. D'Agostini [73]. Let's call cause (C_i , $i=1,2,3,\ldots\ldots n_C$) the true generated variable values and effect E_j ($j=1,2,3,\ldots\ldots n_E$) the observed variable values. The migration matrix is thus the probability $P(E_j|C_i)$ that having a certain generated value C_i the observation will be E_j. The Bayes' theorem states that, it is possible to compute, under a certain hypothesis $P_0\ (C_i)$ for the true distribution, the conditional probability $P(E_j|C_i)$ that an observed value E_j is coming from a generated value C_i. Let's call this probability as the smearing matrix:

$$P(C_i|E_j) = \frac{P(E_j|C_i)\ P_0(C_i)}{\sum_{l=1}^{n_C} P(E_j|C_l)\ P_0(C_l)} \qquad (4.4)$$

If one observes $n(E_j)$ events with effect Ej, the expected number of events assignable to each of the cause is

$\hat{n}(C_i) = n(E_j)\, P\left(C_i \middle| E_j\right)$. The estimated true distribution for the cause variable turns out to be $\hat{P}(C_i) = \hat{n}(C_i)/\sum_{l=1}^{nc} \hat{n}(C_l)$. The method is iterative in the search of the solution I for the distribution P(C), using at each step the previous estimated value $\hat{P}(C)$ to recompute the smearing matrix. A remarkable advantage of such method is that it can be immediately generalized to any dimension of the cause and effect space.

In this analysis, the physical quantities *t* is the maximum track density inside a certain interval with respect to (pseudo)rapidity, the measurement *m* is the event by event maximum track density. From the discussion in the last section, one can recognize that *P*(*T*) is the charged hadron multiplicity distribution(*T*) and *P*(*Mm*) is the raw spectrum(*Mm*). *P*(*M*j*Tt*) is the response matrix(*R*) which describes the physics and detector effects. This unfolding procedure contains the following steps:

1. Start with the PYTHIA generator max. track density distribution (or a flat distribution for cross-check) as a prior distribution (P_t), calculate the smearing matrix ($\tilde{R}_{t\,m}$)

$$\tilde{R}_{t\,m} = \frac{R_{mt}\, P_t}{\sum_{t'} R_{mt'}\, P_{t'}} \tag{4.5}$$

2. Calculate the unfolded distribution with the smearing matrix by using the measured max. track density spectrum (M_m):

$$U_t = \sum_m \tilde{R}_{t\,m}\, M_m \tag{4.6}$$

3. Replace the prior distribution P_t by U_t and go back to step 1 for several iterations.

Unfolding for High Multiplicity

The main problem in high multiplicity events, we do not have MC with to do unfolding specially at high maximum track density. We tried to generate MC with high multiplicity events with PYTHIA-8 tune 4C and PYTHIA-6 tune Z2 in addition to MC which was used in ridge paper (MIT group). In all of these MC we faced the same problem; missing MC the region with events have high max. track density. To overcome that problem, we did the following steps:

1. the relation between maximum number of tracks inside window with width 0.1, 0.2 and 0.5 w.r.t eta and rapidity and the ratio between RECO and GEN in y-axis as shown in figure (4-6) and (4-7). The rapidity is define as

   $$y = \frac{1}{2}\, ln\left[\frac{E+p_t}{E-p_t}\right] \qquad (4.7)$$

   we put here the pion mass.

2. Make fitting for each figure, the fitting function in all cases is double exponential function:

   $$\frac{dN}{dn} = -p0\; e^{p1n} + p2\; e^{p3n}$$

   Where, p0, p1, p2 and p3 are the fitting parameters. The values of these parameters are put in each plot.
3. Extrapolate the fitting curve to get the ratio between the number of events with maximum track density (n) in the reconstructed and generated event sample.
4. Divide each data point with its equivalent ratio value to get the correct data value.

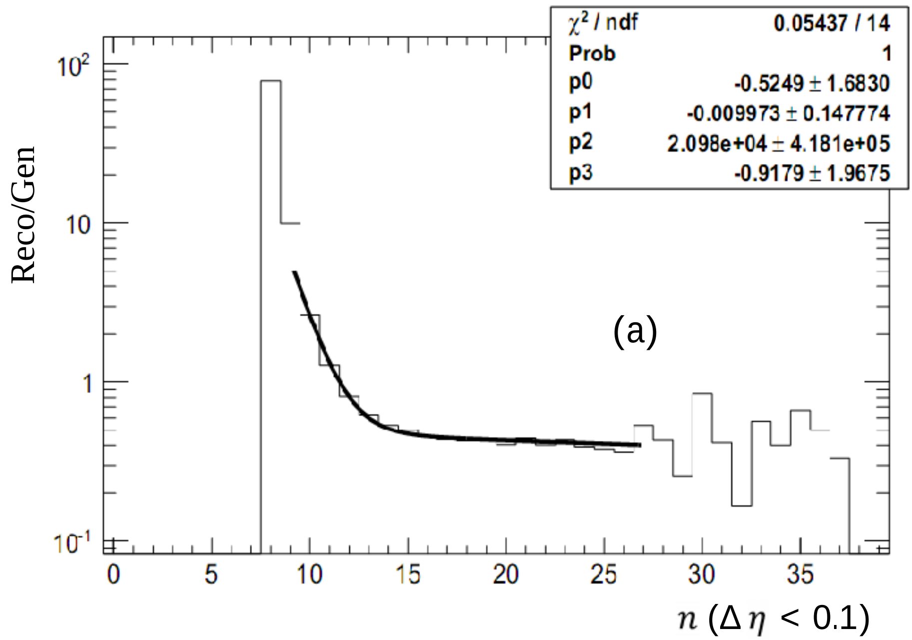
χ² / ndf 0.05437 / 14
Prob 1
p0 -0.5249 ± 1.6830
p1 -0.009973 ± 0.147774
p2 2.098e+04 ± 4.181e+05
p3 -0.9179 ± 1.9675
Reco/Gen
(a)
n (Δη < 0.1)

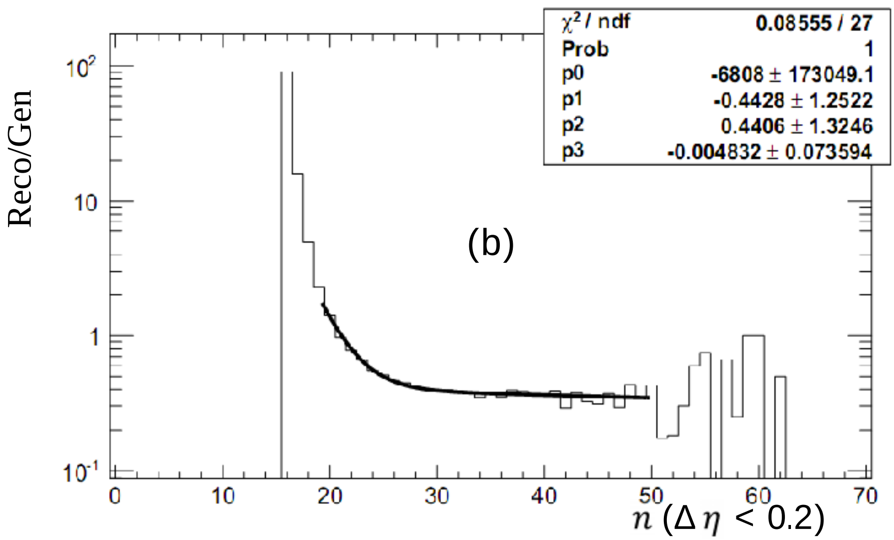
χ² / ndf 0.08555 / 27
Prob 1
p0 -6808 ± 173049.1
p1 -0.4428 ± 1.2522
p2 0.4406 ± 1.3246
p3 -0.004832 ± 0.073594
Reco/Gen
(b)
n (Δη < 0.2)

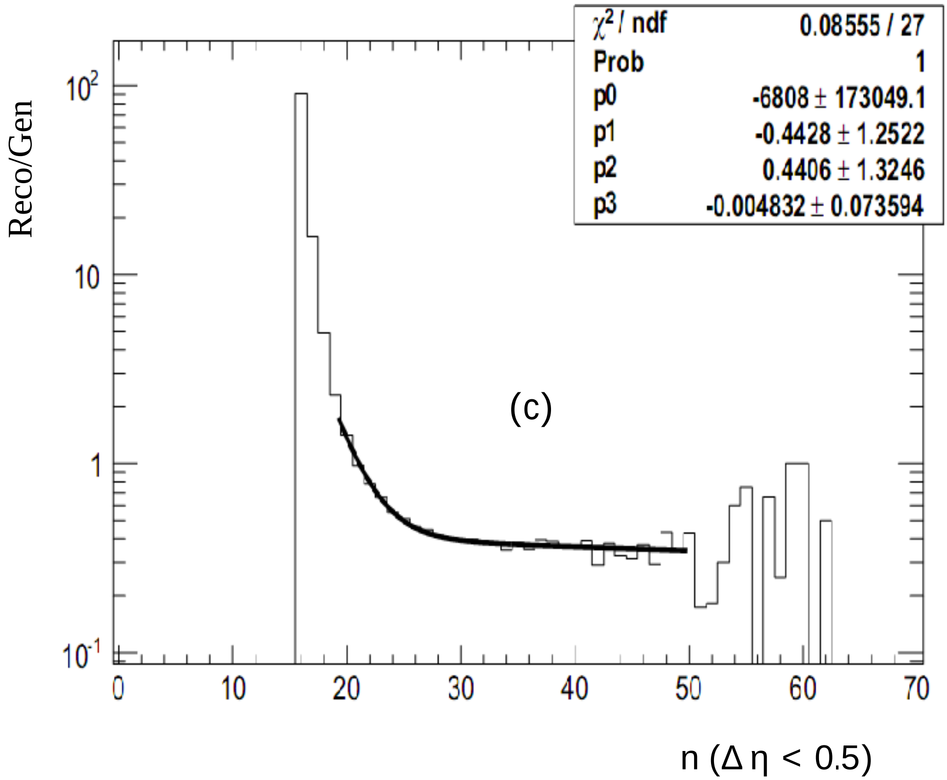

Figure (4-6): The relation between n (number of tracks in side window) and ratio between Reco/ Gen (a) when the window width 0.1, (b) when window width 0.2 and (c) when window width 0.5 all w.r.t η.

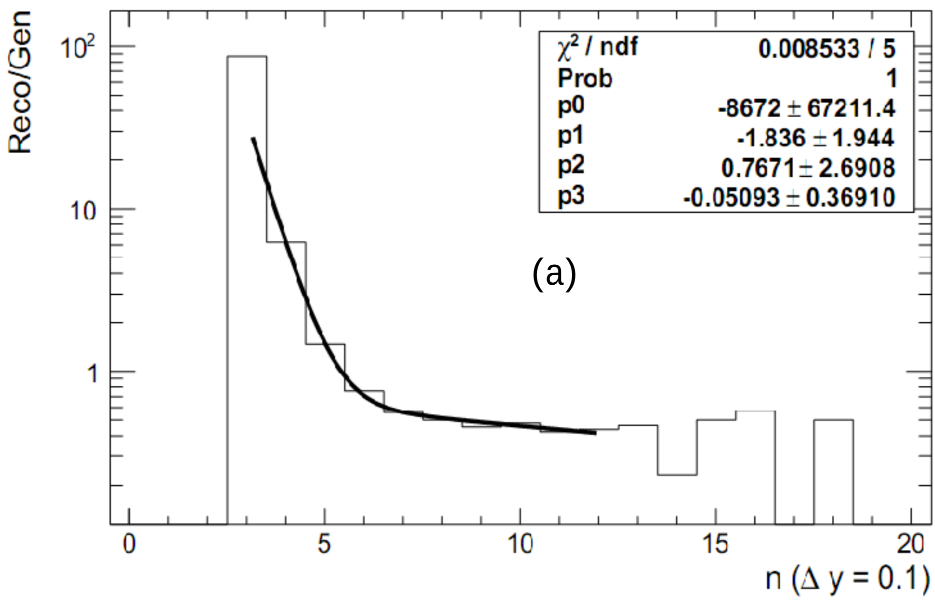

Reco/Gen
10^2
10
1
χ^2 / ndf 0.008533 / 5
Prob 1
p0 -8672 ± 67211.4
p1 -1.836 ± 1.944
p2 0.7671 ± 2.6908
p3 -0.05093 ± 0.36910
(a)
0
5
10
15
20
n (Δ y = 0.1)

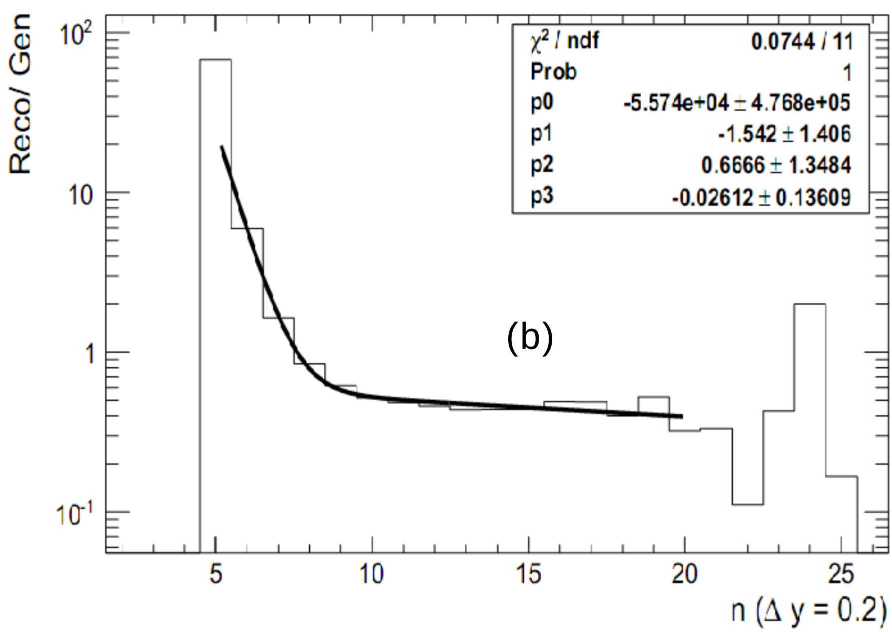

Reco/ Gen
10^2
10
1
10^{-1}
χ^2 / ndf 0.0744 / 11
Prob 1
p0 -5.574e+04 ± 4.768e+05
p1 -1.542 ± 1.406
p2 0.6666 ± 1.3484
p3 -0.02612 ± 0.13609
(b)
5
10
15
20
25
n (Δ y = 0.2)

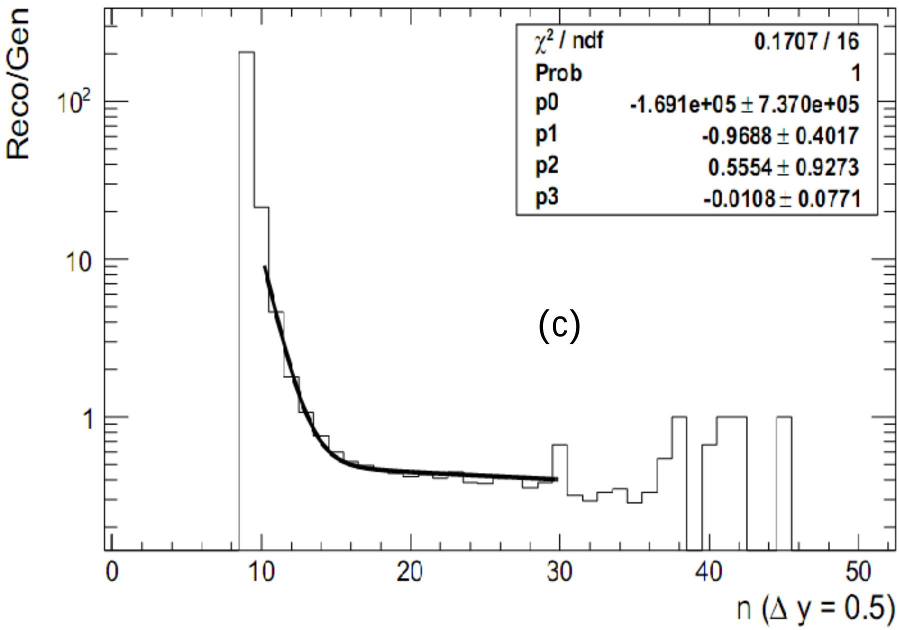

Figure (4-7): The relation between n (number of tracks in side window) and ratio between Reco/ Gen (a) when the window width 0.1, (b) when window width 0.2 and (c) when window width 0.5 all w.r.t y.

(4-4) Systematic Errors:

To estimate the uncertainty from the acceptance and efficiency corrections that comes from the track quality cuts, we test three different modified track quality cuts for the data used and in the MC-based corrections.

- looser primary vertex compatibility: (d0/σd0) and (dz/σdz) max significance cuts from 3 to 5.
- Changing dz (cm) w. r. t. vertex from 0.2 to 0.3.
- Change track quality from HighPurity to tight tracks.
- looser # of hits requirement: minimum numberOfValidHits cut from 5 to 3.
- looser track fit quality: maximum ptError/pt cut from 0.05 to 0.1.
- And change the number of degrees of freedom for vertex from 4 to 3.

Varied quantity	**Variation**	**Variation in the result**
(d0/σd0) and (dz/σdz)	3->5	Less than 1%
Dz	0.2->0.3	Less than 1%
Trackqualilty	HighPurity->Tight	Less than 1 %
#of Valid Hits	5->3	Less than 1%
ptError/pt	0.05->0.1	Less than 1%
NDF	4 ->3	1%

(4-5) Results:

We determine the maximum track density $(dn/d\eta)_{max}$ within event by scanning with a fixed width for small interval w. r. t. (pseudo)rapidity ($\Delta\eta$) across the full tracker η range $|\eta| < 2.5$, i.e only one reading per event was taking in our account, this reading was the maximum track density inside a certain windows. In figures (4-8), (4-9), and (4-10) show the maximum track density inside a certain windows 0.1, 0.2, 0.5 respectively w. r. t. pseudorapidity, for data when we applied HLT_L1Tech_BSC_minBias trigger, and also for MC at generator level (Gen level) and reconstruction level (Reco level). From these figures, we found that see some slighty difference between Gen level and Reco level, that due to missed particles which undetected by detector; the reconstruction efficiency is less than one and also depends on the track pt, and the second reason is the optimum conditions between accelerator and detector which are not well known. So, we have to do unfolding for obtaining data.

Figures (4-11), (4-12), and (4-13), show the fitting for the unfolding data, in the case of studying of the max. track density inside the windows 0.1, 0.2, 0.5, respectively. We are using the same fitting function as in previous work

$$\frac{dn}{d\eta} = p0.\,e^{-p1.n} \qquad (4.8)$$

The fitting parameters in the three different cases and range of fitting are summarized in table (4.2) and figures.

The same thing is done in case of rapidity as shown in figures (4-14), (4-15), (4-16).

Figures (4-17), (4-18), (4.19) show the fitting for unfolding curves of the max. track density inside windows 0.1, 0.2, 0.5 w. r. t. rapidity respectively. The fitting function is similar to that of pseudorapidity.

The fitting parameters a, b and range of fitting are summarized in table (4.3) in the case of studying of max. track density inside three different width 0.1, 0.2 and 0.5 with respect to rapidity.

The main important point from the work in the data HLT_L1Tech_BSC_minBias trigger, is that there is not event behind the fitting line.

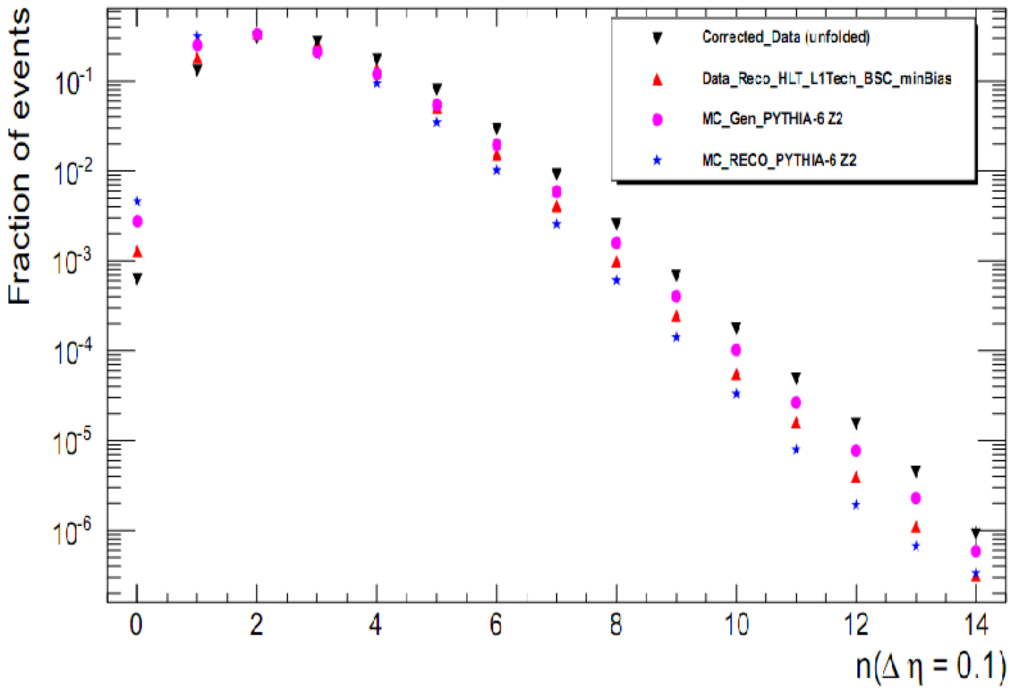

Figure (4-8): Maximum track density inside a small interval with width 0.1 w. r. t. pseudorapidity for data and MC at generator level and Reco level, and corrected data (unfolded).

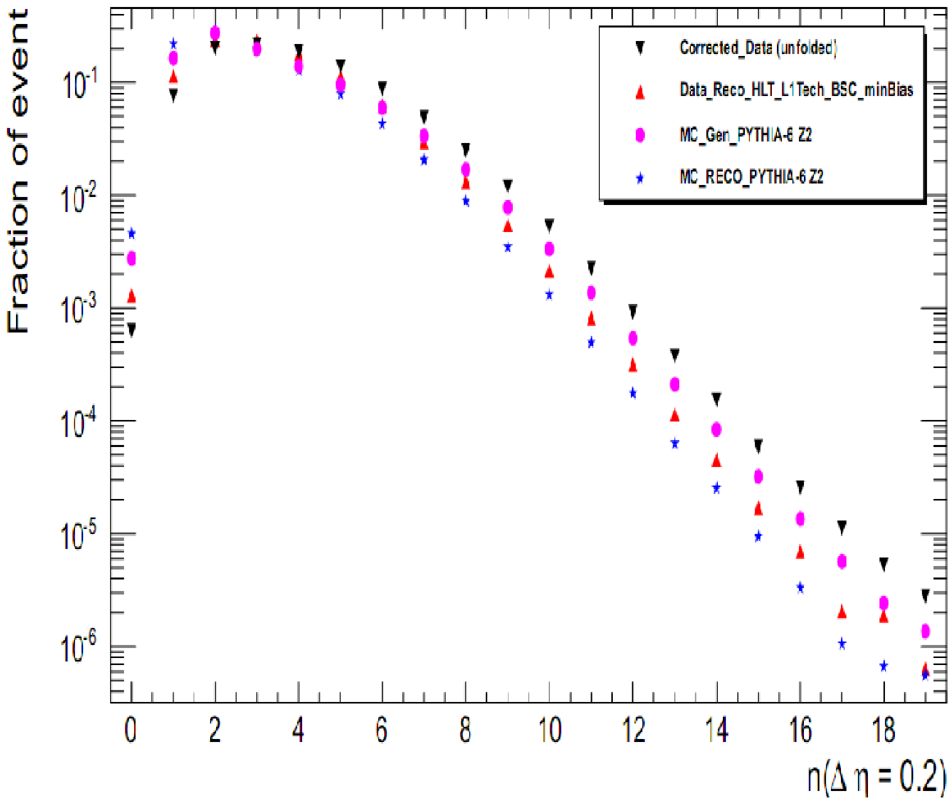

Figure (4-9): Maximum track density inside a small interval with width 0.2 w. r. t. pseudorapidity for data and MC at generator level and Reco level, and corrected data (unfolded).

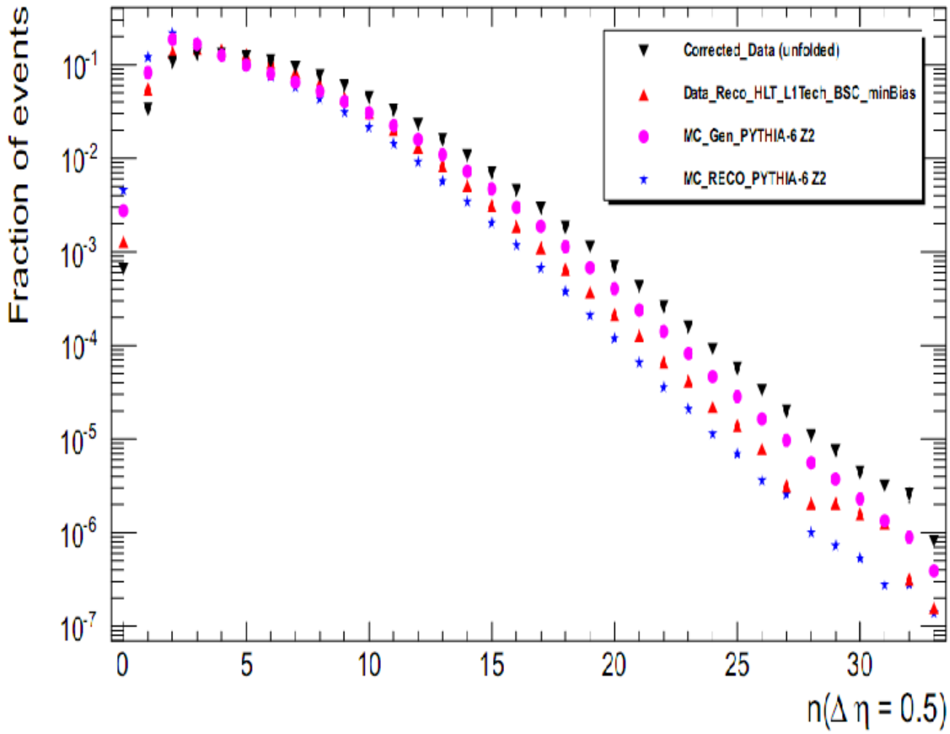

Figure (4-10): Maximum track density inside a small interval with width 0.5 w. r. t. pseudorapidity for data and MC at generator level and Reco level, and corrected data (unfolded).

Table (4.2): the values of fitting parameters a, and b in the case of studying of max. track density w. r. t pseudorapidity η

Interval width w. r. t. η	a	b	chi2/ndf
0.1	5.069e+0.8 ± 1.370e+07	1.298 ± 0.004	25.15/5
0.2	2.256e+08 ± 6.014e+0.6	0.8821 ± 0.0025	26.95/7
0.5	8.966e+07 ± 2.764e+06	0.4975 ± 0.0016	34.35/11

Table (4.3): the values of fitting parameters a, and b in the case of studying of max. track density w. r. t rapidity (y)

Interval width w. r. t. y	a	b	chi2/ndf
0.1	7.825e+0.9 ± 1.343e+08	2.475 ± 0.003	15.34/3
0.2	5.203e+08 ± 1.425e+0.7	1.305 ± 0.004	34.1/6
0.5	1.859e+08 ± 6.824e+06	0.7772 ± 0.0028	11.35/8

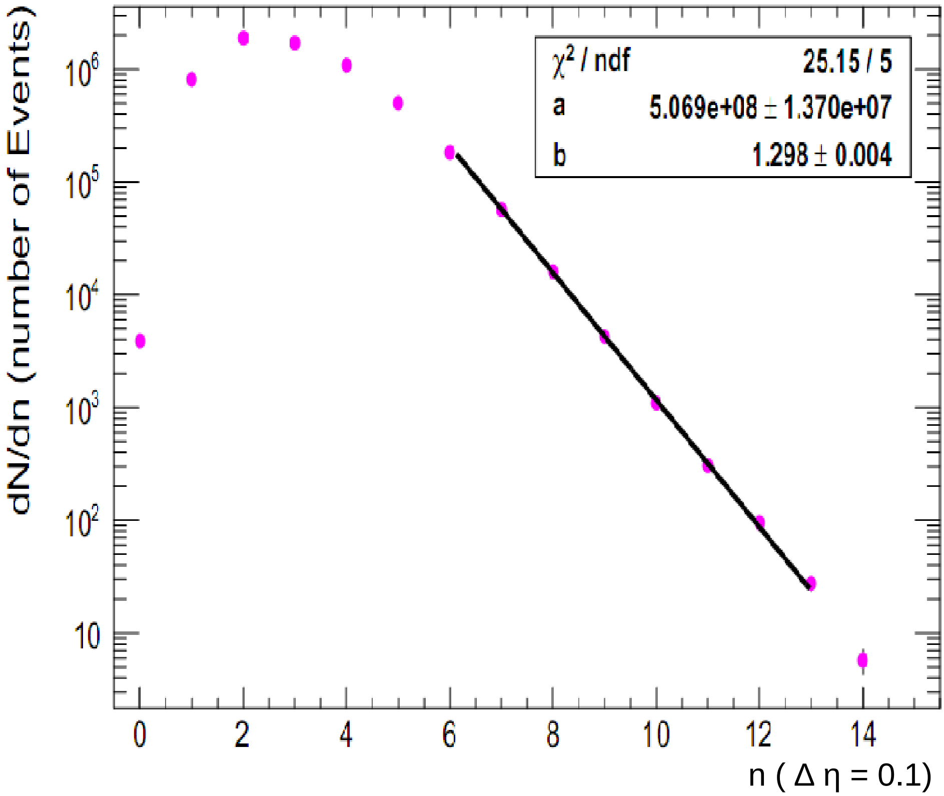

Figure (4-11): Fitting for unfolding curve with range (6.1-13) in the case of studying the max. track density inside small interval with width 0.1 w. r. t. η.

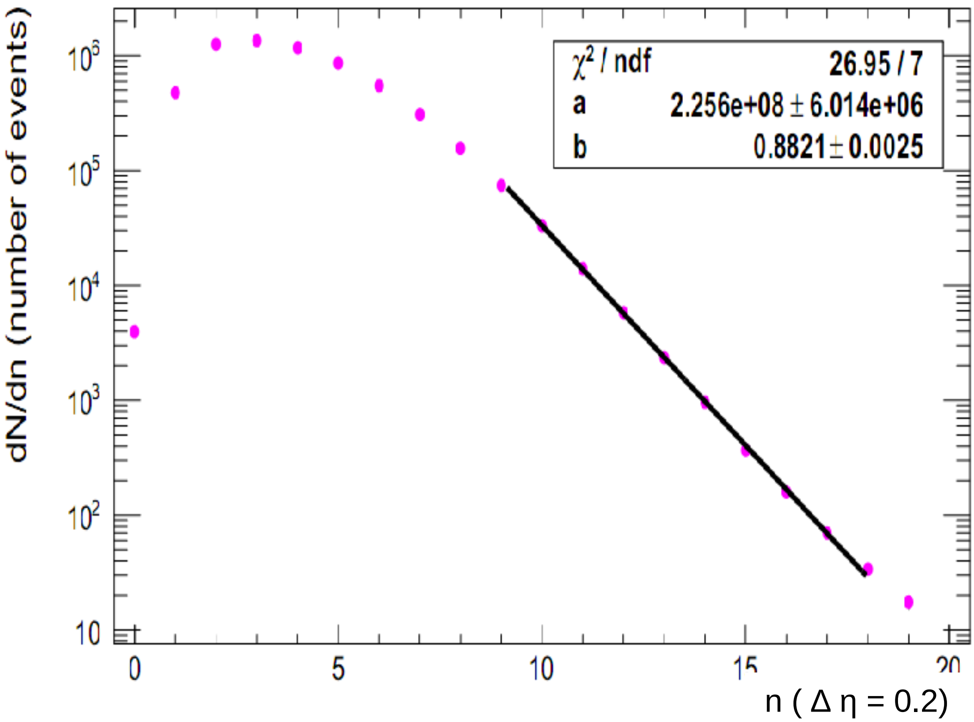

Figure (4-12): Fitting for unfolding curve with range (9.1-16) in the case of studying the max. track density inside small interval with width 0.2 w. r. t. η

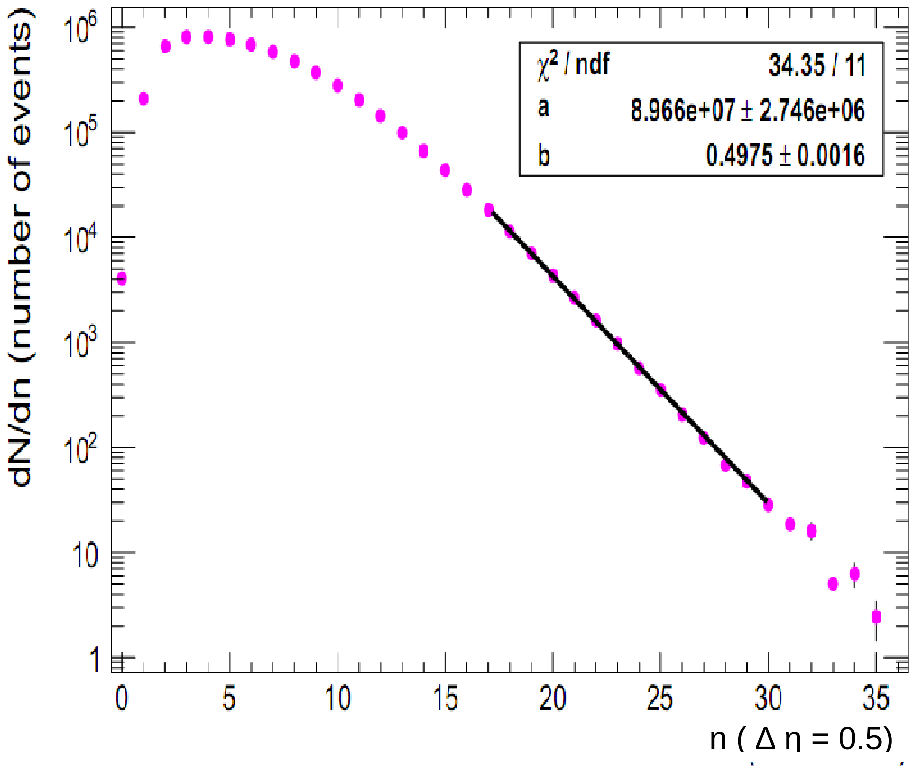

Figure (4-13): Fitting for unfolding curve with range (14-30) in the case of studying the max. track density inside small interval with width 0.5 w. r. t. η.

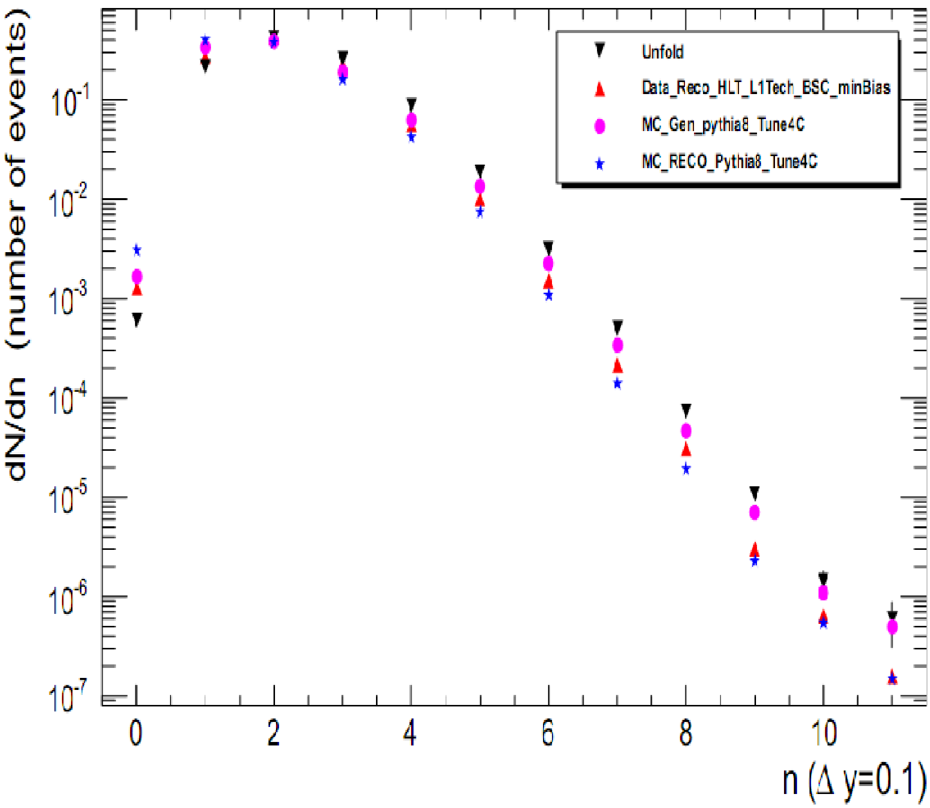

Figure (4-14): Maximum track density inside a small interval with width 0.1 w. r. t. rapidity for data and MC at generator level and Reco level, and corrected data (unfolded).

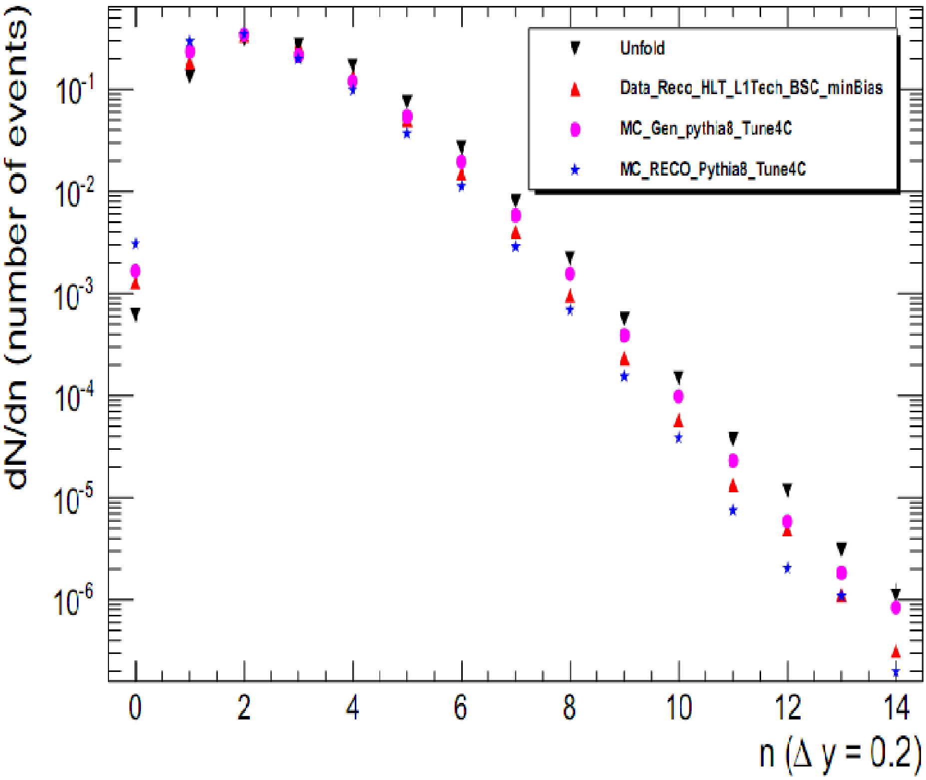

Figure (4-15): Maximum track density inside a small interval with width 0.2 w. r. t. rapidity for data and MC at generator level and Reco level, and corrected data (unfolded).

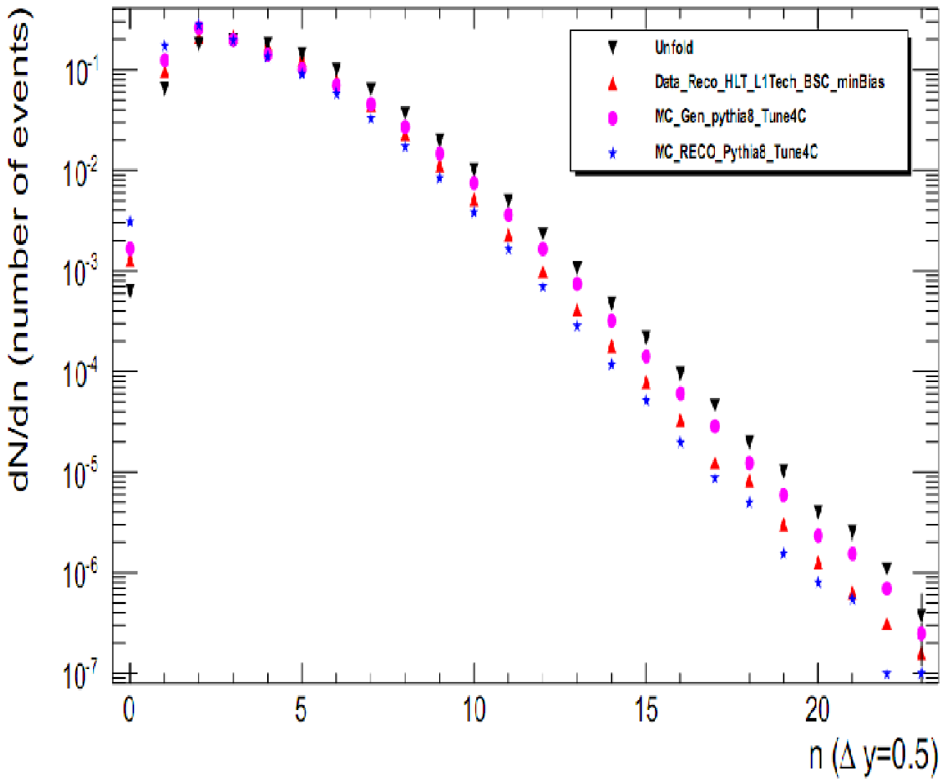

Figure (4-16): Maximum track density inside a small interval with width 0.5 w. r. t. rapidity for data and MC at generator level and Reco level, and corrected data (unfolded).

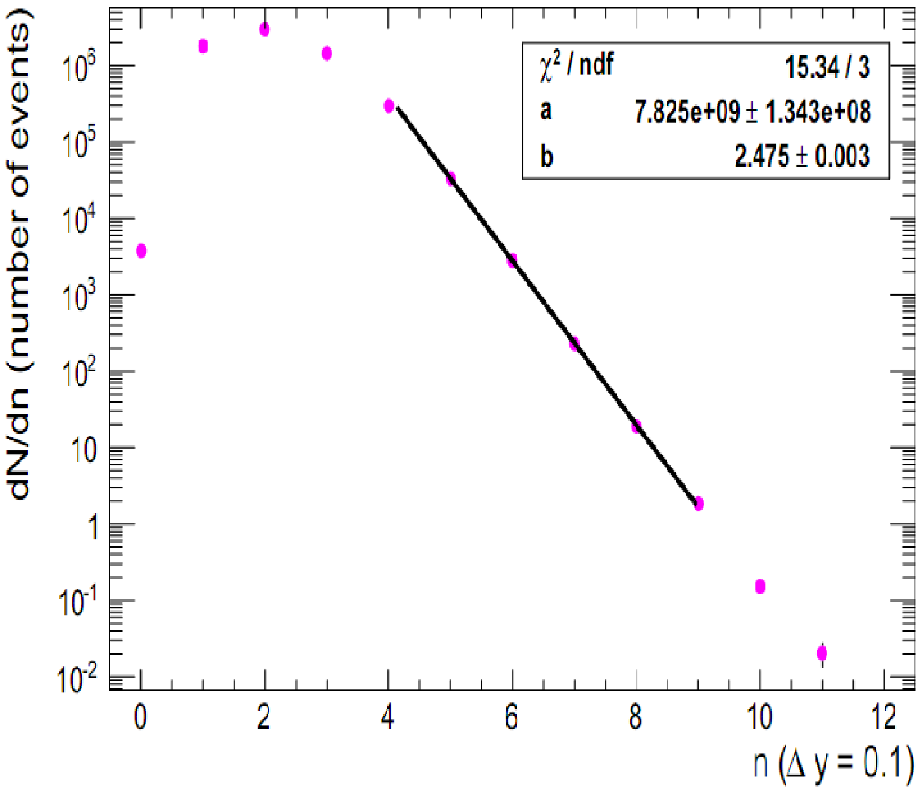

Figure (4-17): Fitting for unfolding curve with range (4-9) in the case of studying the max. track density inside small interval with width 0.1 w. r. t. y.

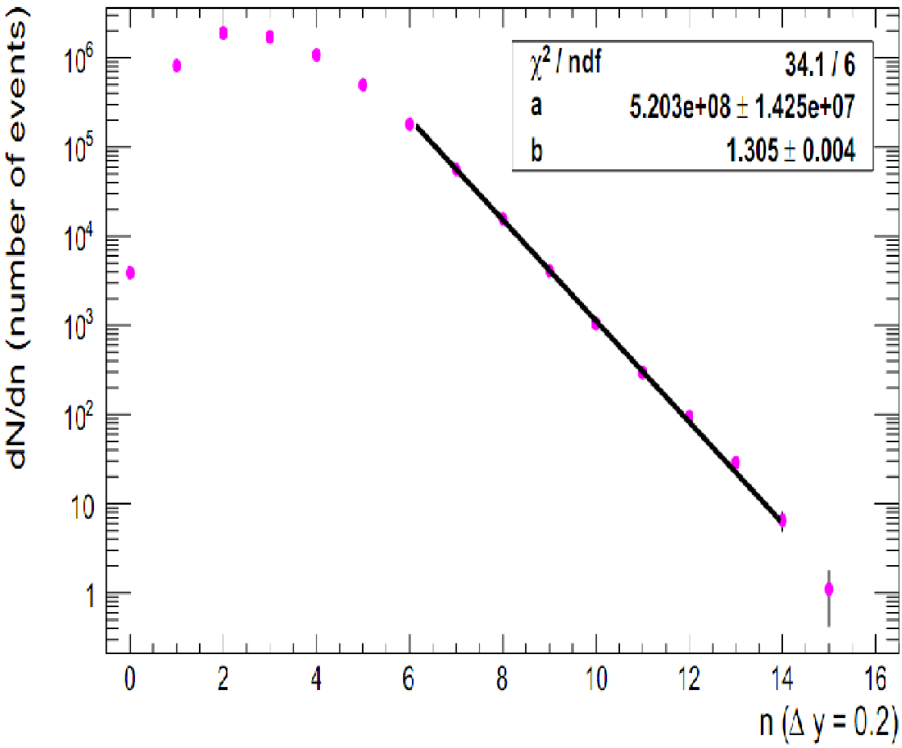

Figure (4-18): Fitting for unfolding curve with range (6.1-14) in the case of studying the max. track density inside small interval with width 0.2 w. r. t. y.

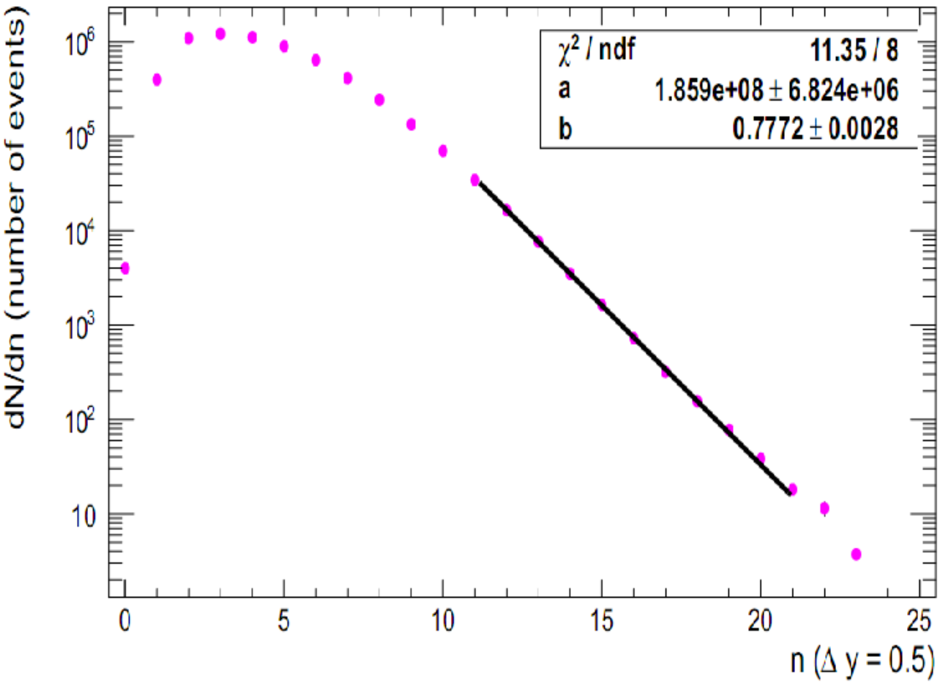

Figure (4-19): Fitting for unfolding curve with range (11-21) in the case of studying the max. track density inside small interval with width 0.5 w. r. t. y.

Figures (4-20), (4-21) and (4-22) show the maximum track density inside a certain windows with widths 0.1, 0.2 and 0.5 respectively w .r. t pseudorapidity η in the case of applying of HLT_PixelTrackMutliplicity100, this trigger passes event with minimum number of tracks 100 and all high level trigger work offline as mentioned in chapter 2 . From the figures, we see that there is a difference between generator level and reconstruction level. Also the Monte Carlo (generated with pythia 8) samples do describe the data specially the events with high track density.

Figures (4-23), (4-24) and (4-25) show the maximum tack density inside a certain windows 0.1, 0.2 and 0.5 respectively w. r. t rapidity. To work with rapidity we have to put particle mass to calculate it in the present work we put the pion mass. Miss matching between data and MC specially at high track density events.

Figures (4-26) to (4-31) show the fitting for data collected. The fit function is

$$\frac{dN}{dn} = a. e^{-b}$$

The parameter values are collected in tables (4.4) and (4.5). The main important point here we see some events after fitting line these events have very high track density. These events appear in figures of fitting.

Figures (4-32) and (4-33) show the comparison between the corrected data obtained from HLT_MinBias and HLT_PixelTrackMulti100. We show from these figures that in the case of two triggers, the number of events is increasing with increasing of the multiplicity (number of tracks) until reaching to maximum value (peak), after that the number of events decreases with increasing in multiplicity. For high maximum track density we find a tail only in the case of high multiplicity trigger.

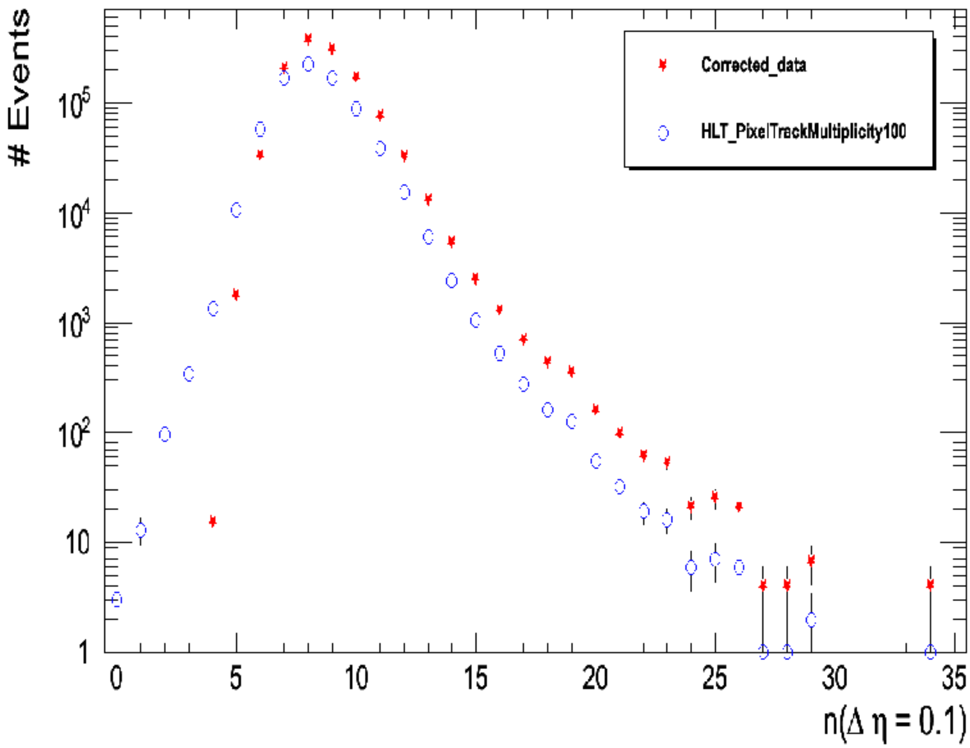

Figure (4-20): Maximum track density inside small interval with width 0.1 w. r. t η, in the case of high multiplicity trigger.

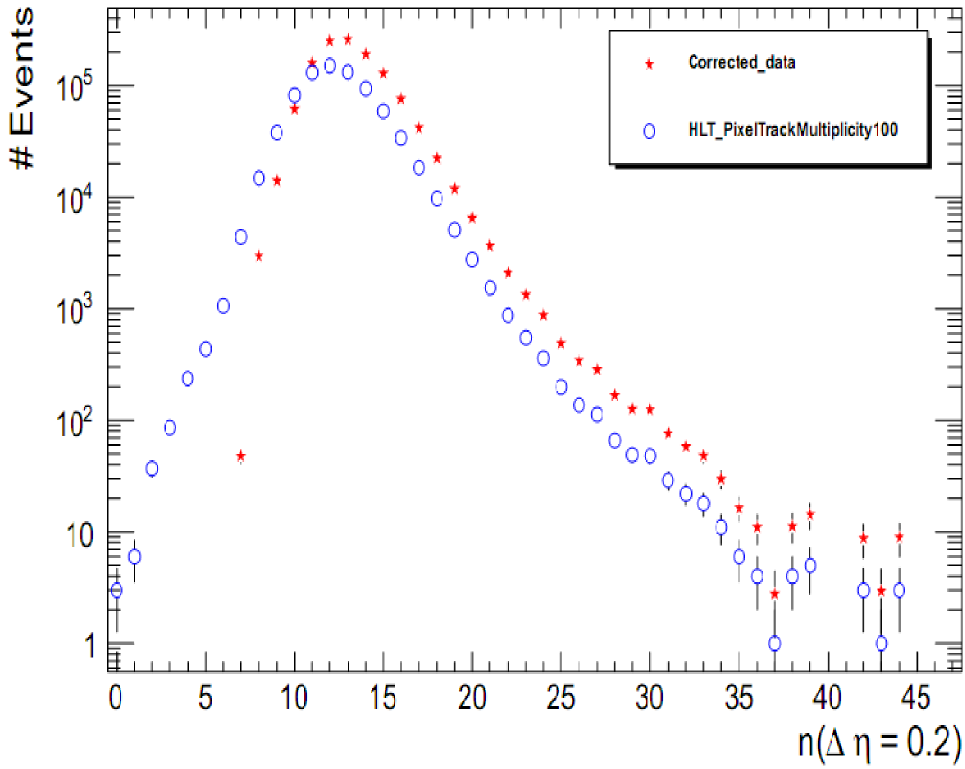

Figure (4-21): Maximum track density inside small interval with width 0.2 w. r. t η, in the case of high multiplicity trigger.

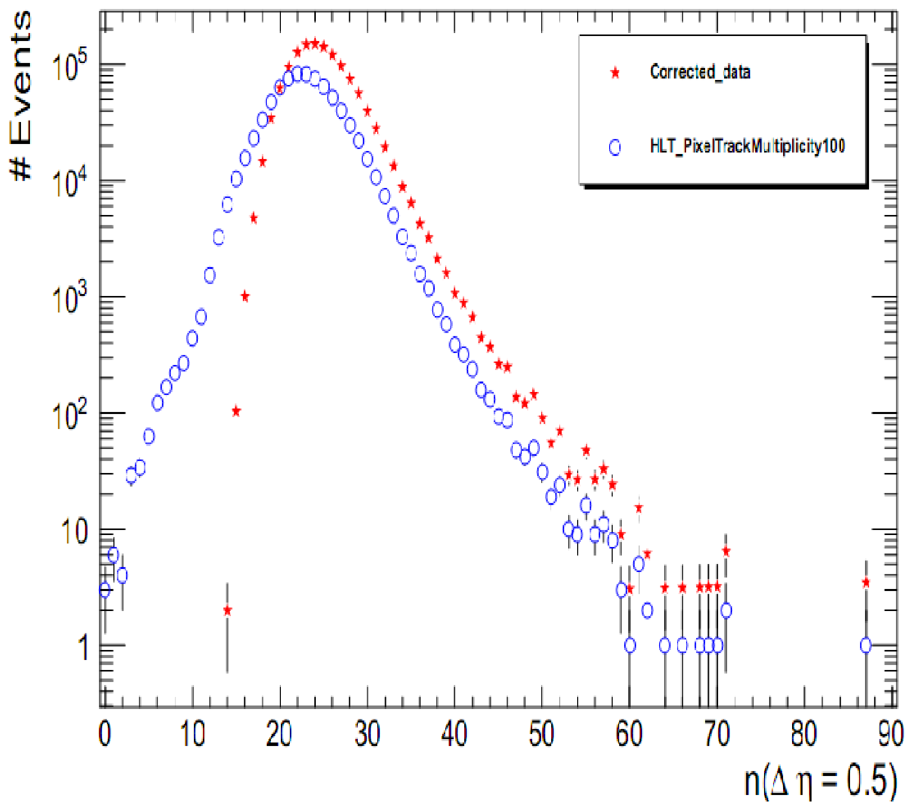

Figure (4-22): Maximum track density inside small interval with width 0.5 w. r. t η, in the case of high multiplicity trigger.

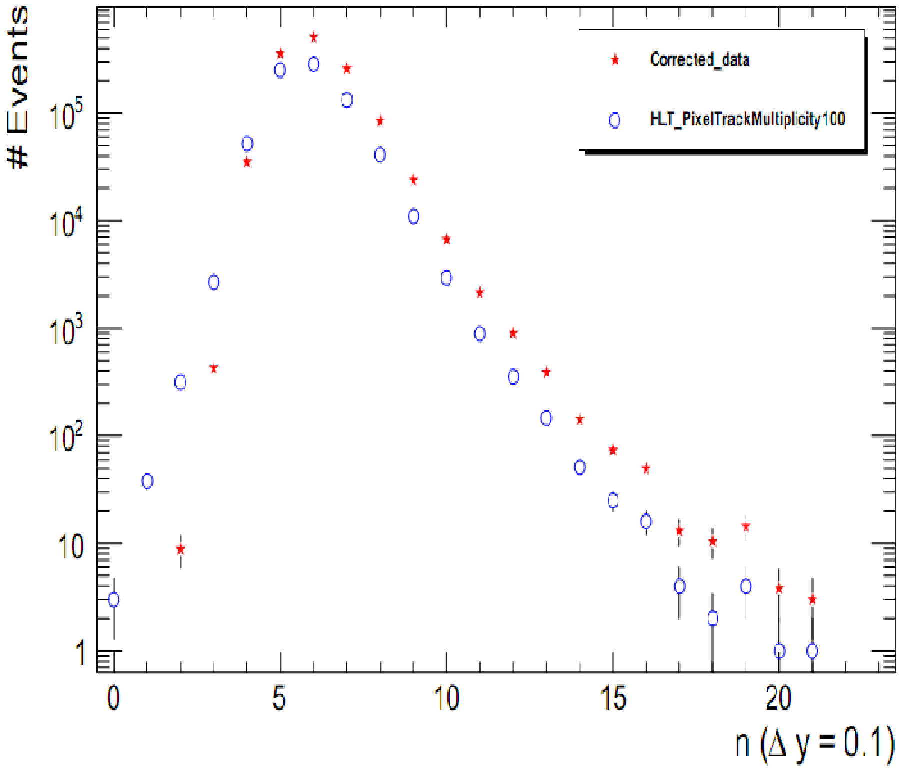

Figure (4-23): Maximum track density inside small interval with width 0.1 w. r. t rapidity (y), in the case of high multiplicity trigger.

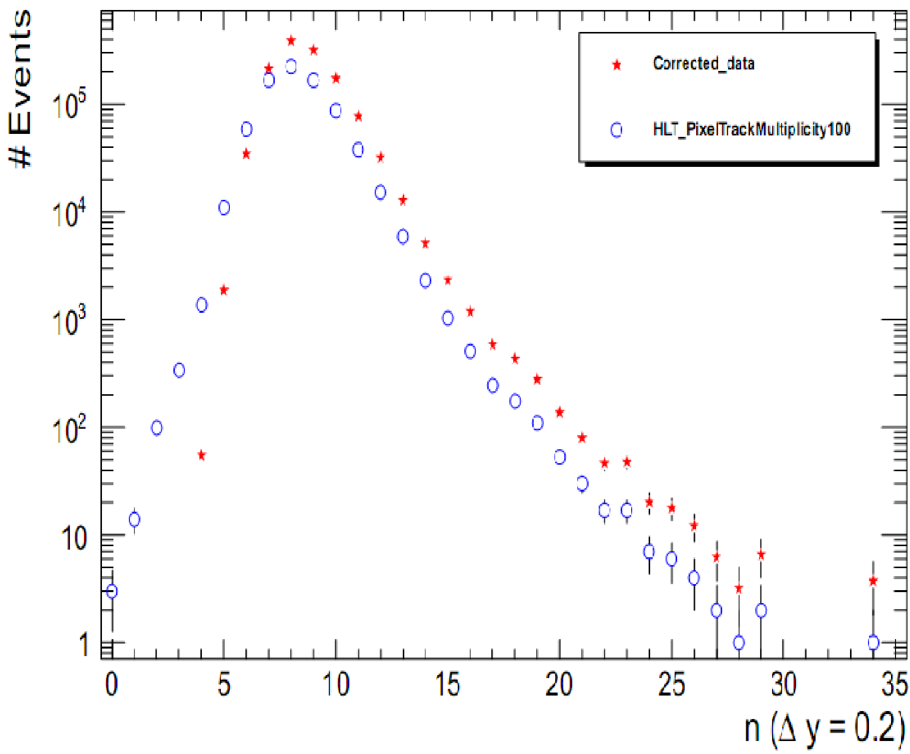

Figure (4-24): Maximum track density inside small interval with width 0.2 w. r. t y, in the case of high multiplicity trigger.

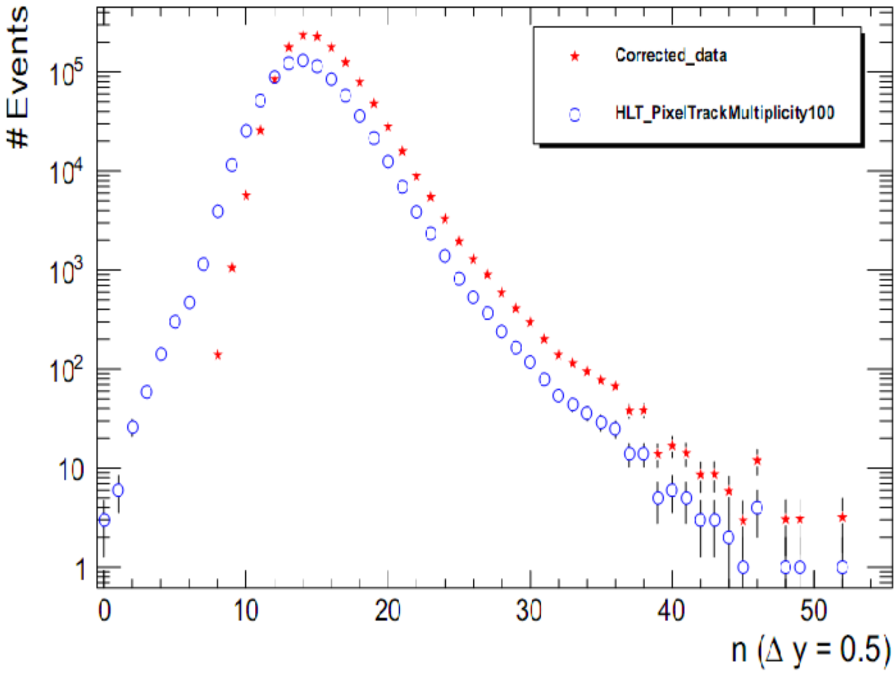

Figure (4-25): Maximum track density inside small interval with width 0.5 w. r. t y, in the case of high multiplicity trigger.

Table (4.4): the values of fitting parameters a, and b in the case of studying of max. track density w. r. t pseudorapidity in the case of HLT_PixelTrackMultiplicity100

Interval width w. r. t. η	a	b	chi2/ndf
0.1	3.937e+0.6 ± 8.101e+05	0.5028 ± 0.0118	25.17/5
0.2	5.66e+06 ± 1.30e+06	0.4017 ± 0.0095	43.38/18
0.5	2.471e+09 ± 1.3677e+08	0.3677 ± 0.015	39.35/6

Table (4.5): the values of fitting parameters a, and b in the case of studying of max. track density w. r. t rapidity HLT_PixelTrackMultiplicity100

Interval width w. r. t. y	a	b	chi2/ndf
0.1	1.927e+0.9 ± 7.123e+07	1.255 ± 0.004	21.31/2
0.2	1.457 e+09 ± 5.055e+07	0.8944 ± 0.030	23.72/3
0.5	1.588e+09 ± 7.255e+07	0.5476 ± 0.023	33.1/4

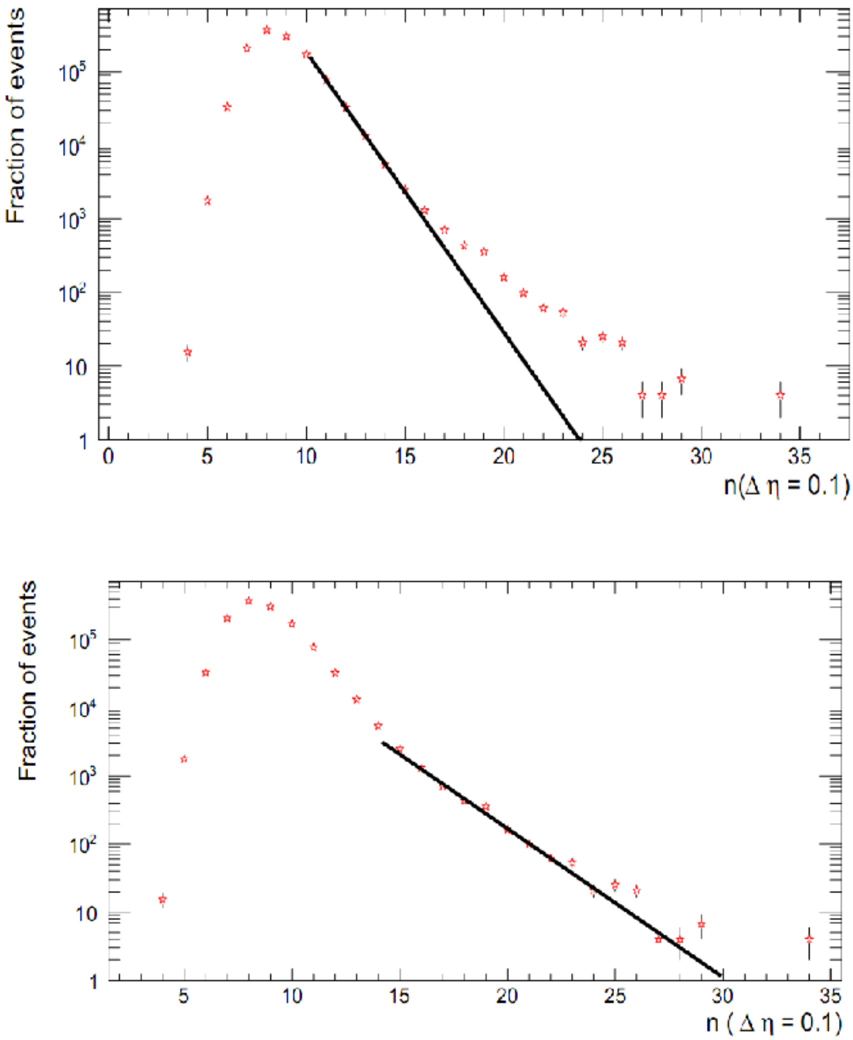

Figure (4-26): Fitting for max. track density inside window 0.1 w. r. t η.

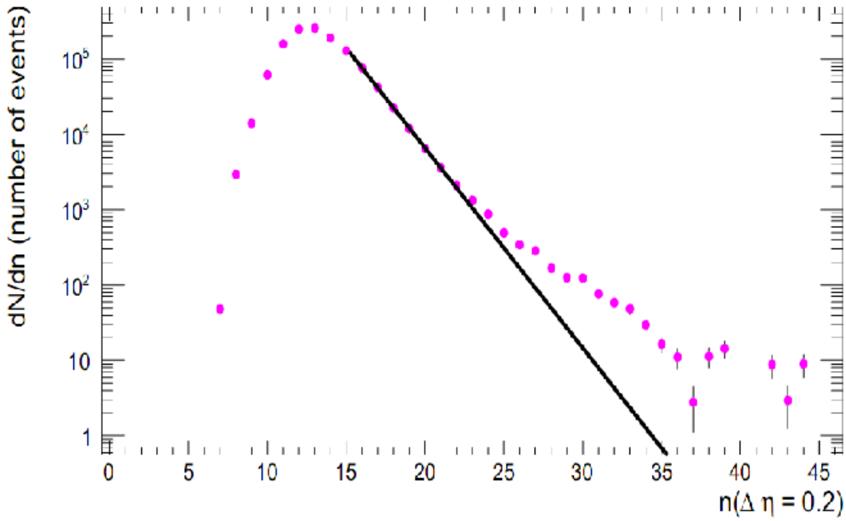

Figure (4-27): Fitting for max. track density inside window 0.2 w. r. t η.

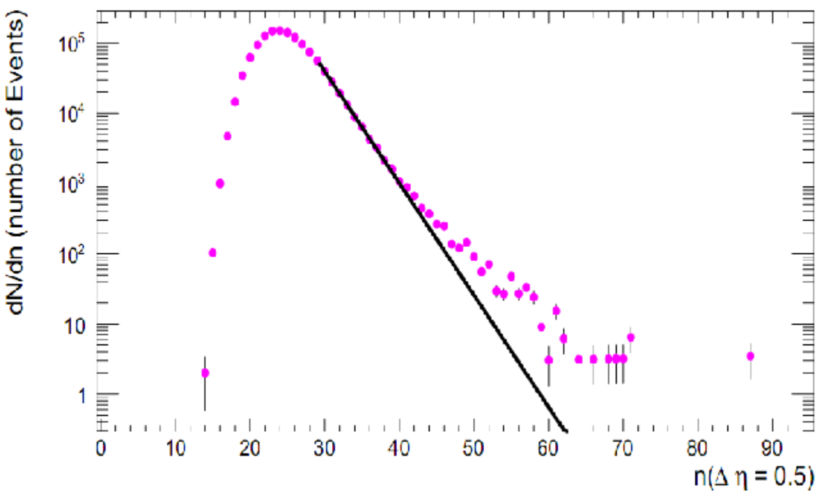

Figure (4-28): Fitting for max. track density inside window 0.5 w. r. t η.

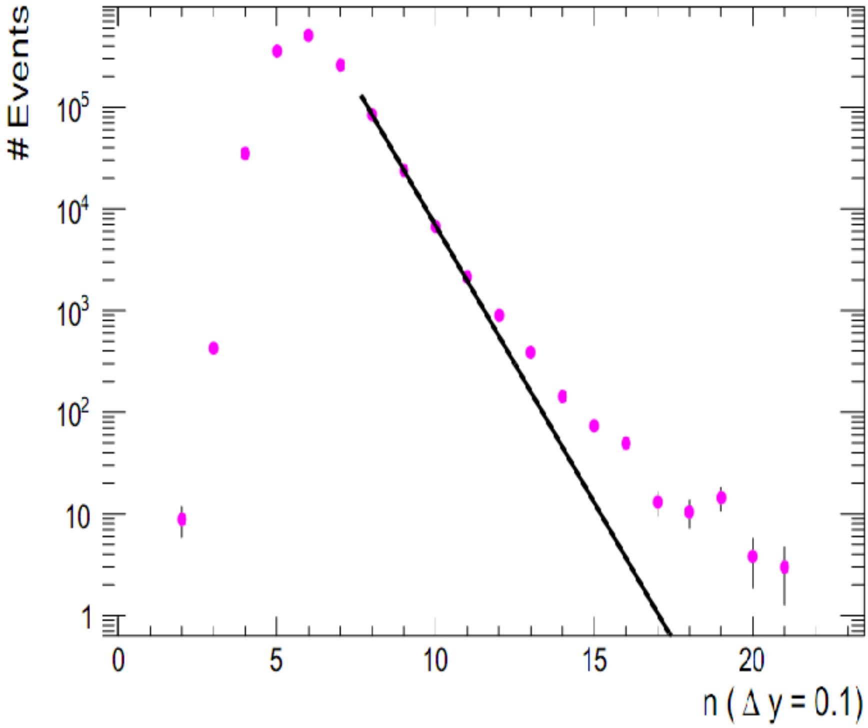

Figure (4-29): Fitting for max. track density inside window 0.1 w. r. t y.

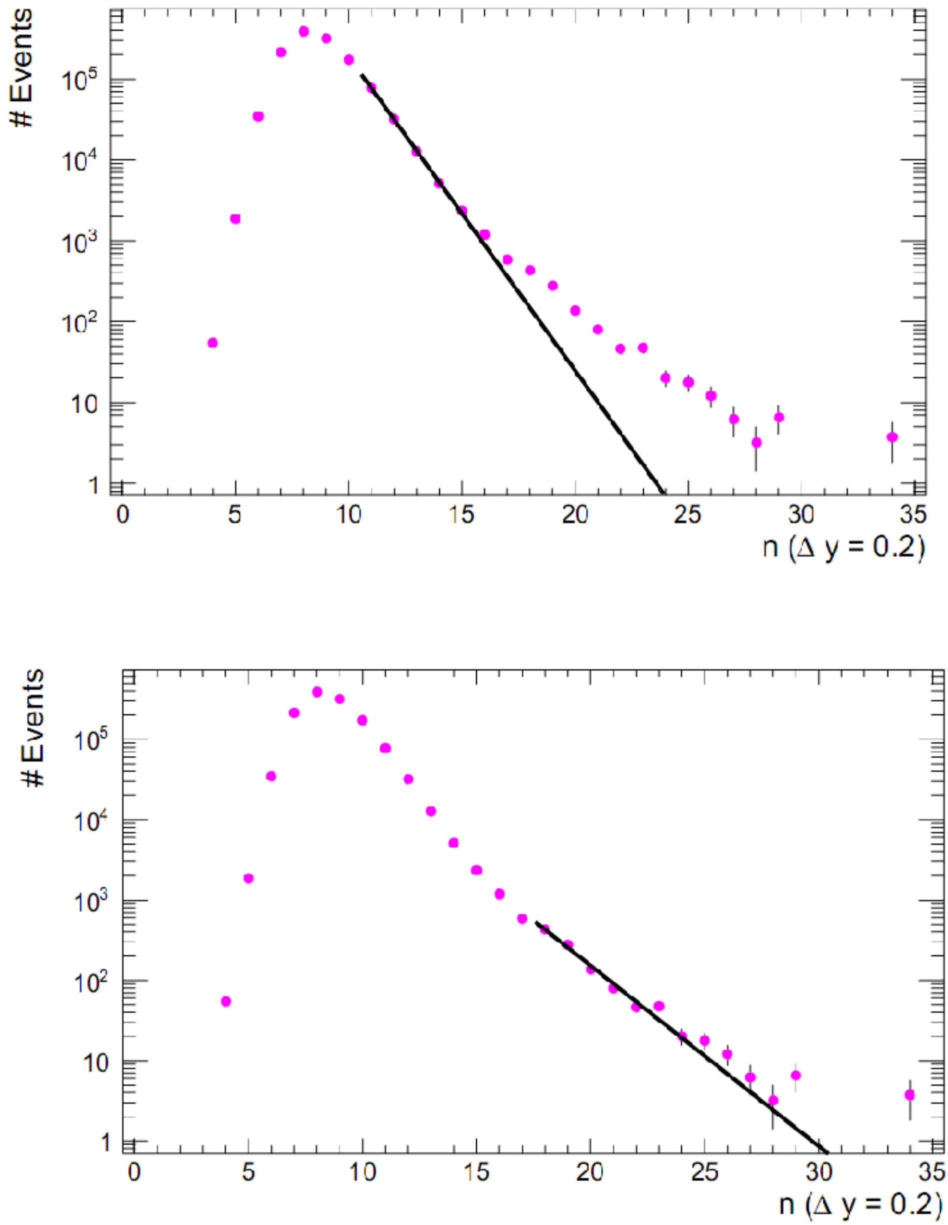

Figure (4-30): Fitting for max. track density inside window 0.2 w. r. t y.

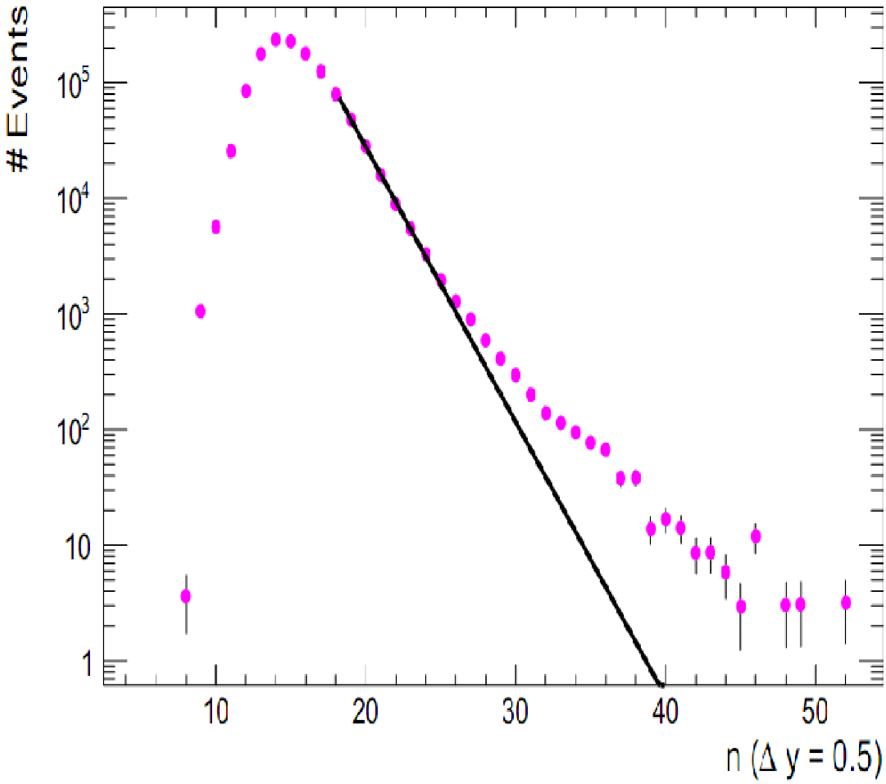

Figure (4-31): Fitting for max. track density inside window 0.5 w. r. t y.

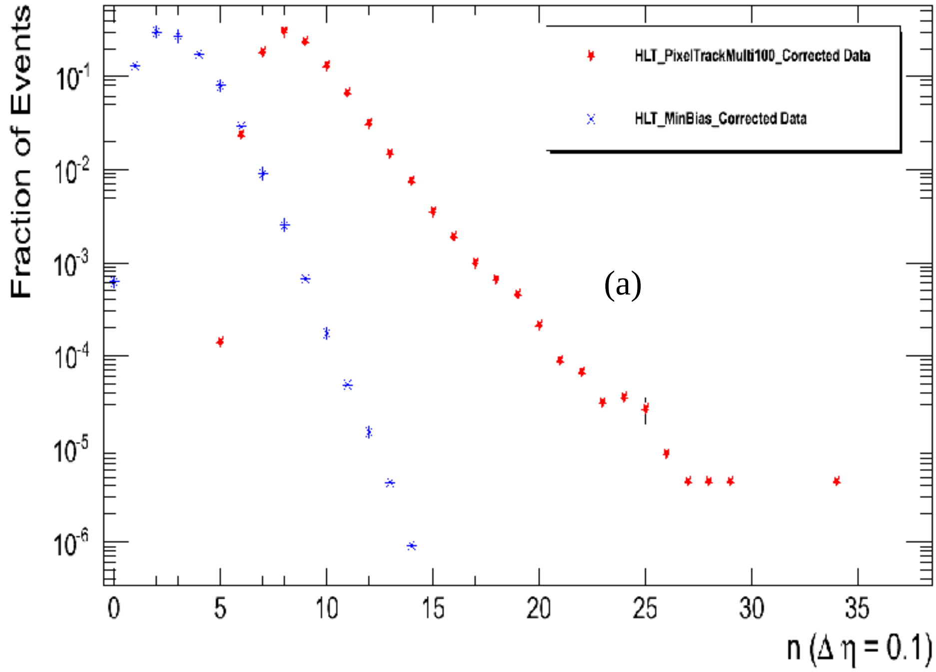
Fraction of Events
HLT_PixelTrackMulti100_Corrected Data
HLT_MinBias_Corrected Data
(a)
n (Δ η = 0.1)

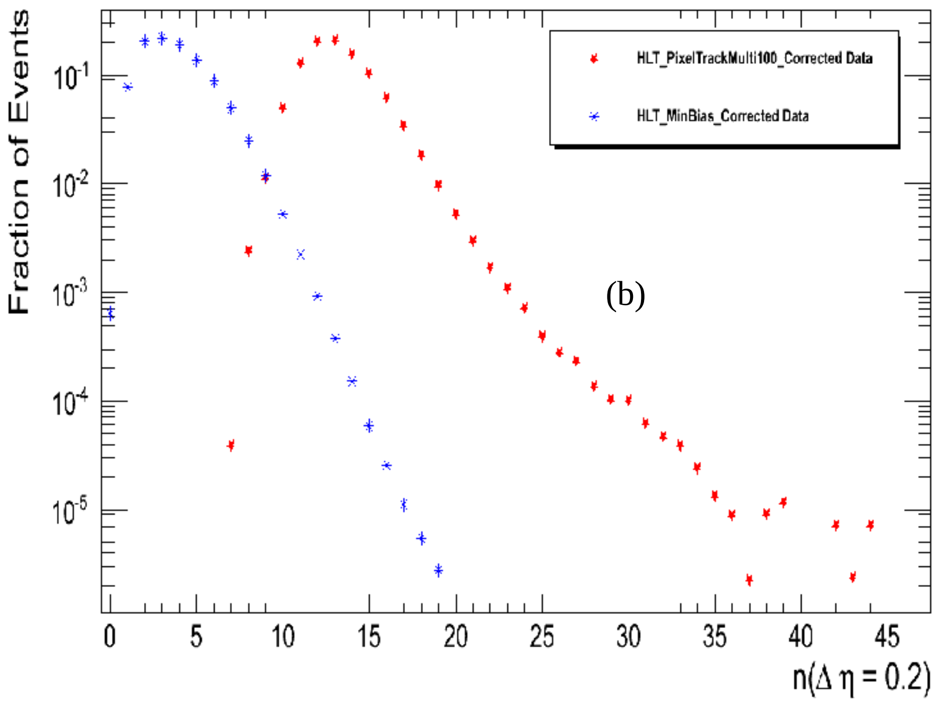
Fraction of Events
HLT_PixelTrackMulti100_Corrected Data
HLT_MinBias_Corrected Data
(b)
n(Δ η = 0.2)

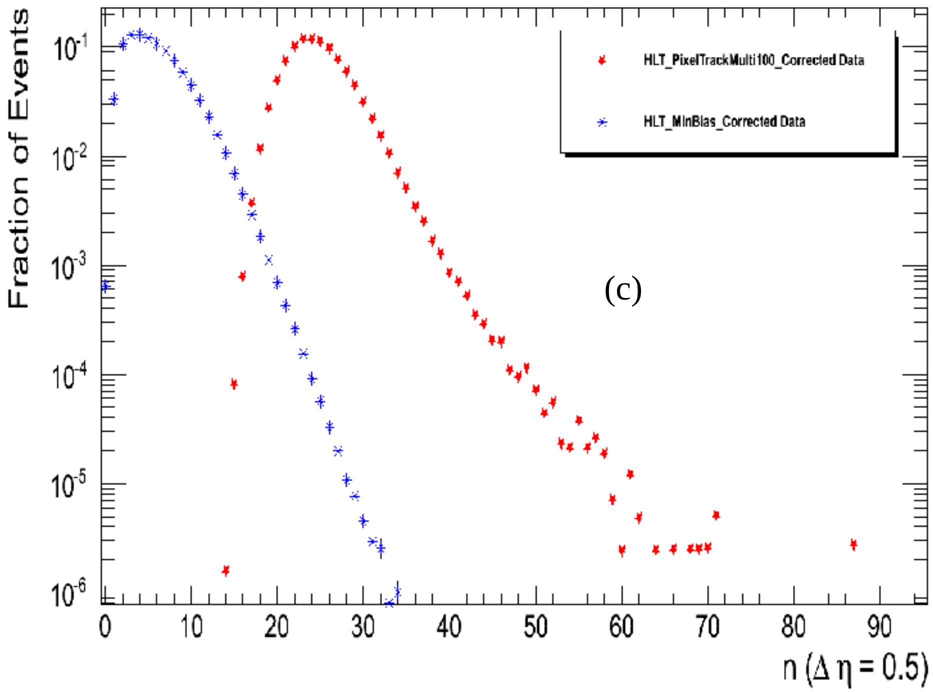

Figure (4-32): Comparison between the corrected data of max. track density inside different windows 0.1, 0.2 and 0.5 w.r.t. η from the two different triggers, HLT_MinBias and HLT_PixelTrackMulti100.

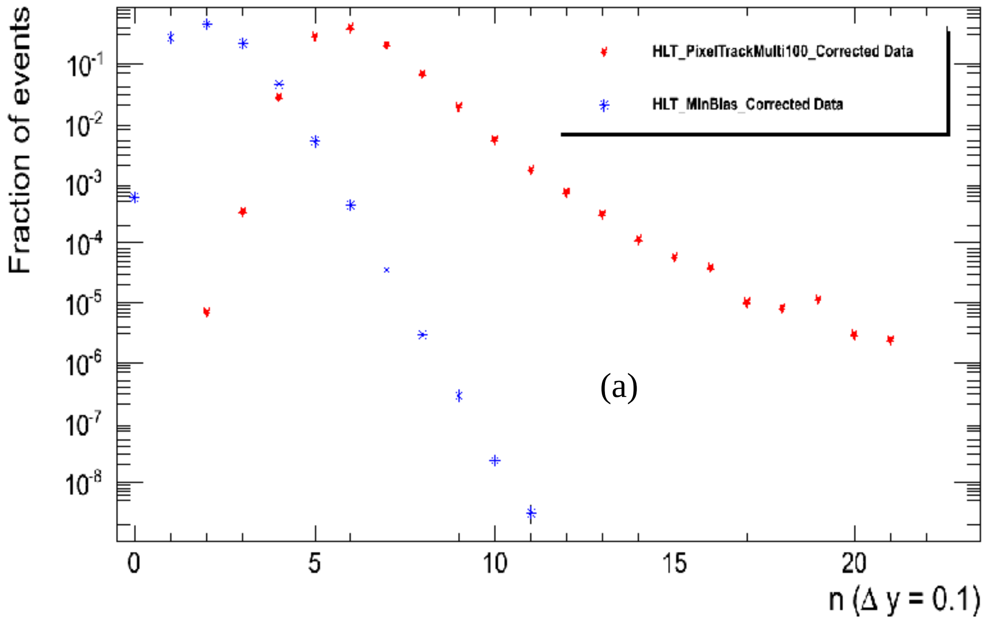

Fraction of events
HLT_PixelTrackMulti100_Corrected Data
HLT_MinBias_Corrected Data
(a)
n (Δ y = 0.1)

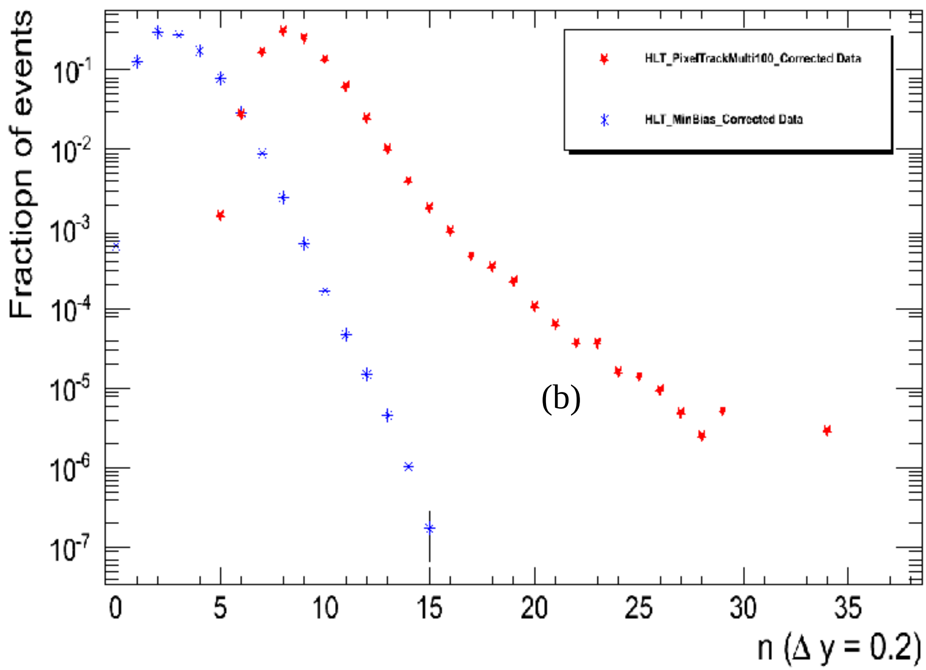

Fractiopn of events
HLT_PixelTrackMulti100_Corrected Data
HLT_MinBias_Corrected Data
(b)
n (Δ y = 0.2)

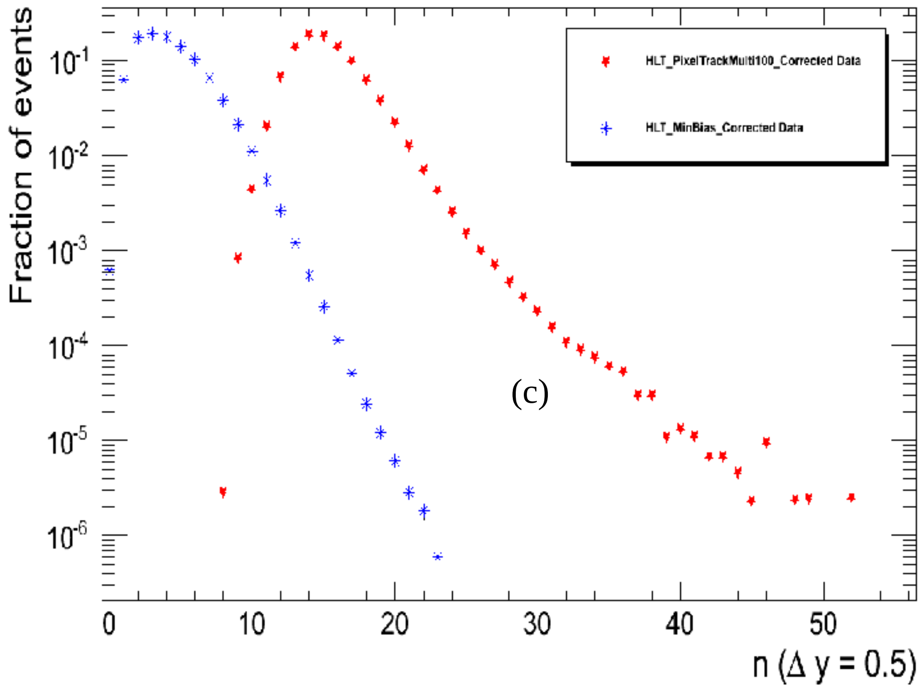

Figure (4-33): Comparison between the corrected data of max. track density inside different windows 0.1, 0.2 and 0.5 w.r.t. rapidity (y) from the two different triggers, HLT_MinBias and HLT_PixelTrackMulti100.

Chapter 5

Kaon to pion Ratio

(5-1) Historical introduction:

Quantum chromodynamics predicts that at sufficiently high temperature, strongly interacting matter will undergo a phase transition from hadronic matter to a state characterized by quark and gluon degrees of freedom, the quark-gluon plasma (QGP) [74]. This quark-gluon plasma is a highly excited state of hadronic matter that occupies a large volume compared with all characteristic length scales. Within this volume individual color charges exist and propagate in the same manner as they do inside the elementary particle. Experimentally, strongly interacting matter under extreme conditions can be created in heavy ion collisions at highly relativistic energies. One of the important signatures of the formation the quark gluon plasma (QGP) is strangeness enhancement [75-79]. Experimentally, strongly interacting matter will undergo a phase transition at extreme conditions can be created in heavy-ion collisions at highly relativistic energies.

One of the important and interesting topics of studying heavy ion collisions is kaon production. At ultra-relativistic energy collisions, it has been argued that kaons might carry the signature for quark-gluon plasma [80, 81]. The E802 experiment [82] is a collaboration of 60 scientists from 13 institutions working at the BNL AGS. The principle goal of the experiment is exploring the behavior of nuclear matter under high temperature and pressure using collisions of 14.5 A GeV/c O and Si projectiles with various nuclear targets. In 1989, the collaborators studied the $K\ /\pi$ ratio in the case of p-p, p-Pb and Si-Au collisions, figure (5-1). They found that, the K^+/π^+ ratios increase with increasing p_t reflecting, at least in part, the influence of approximate $M_\perp$ scaling, where $M_\perp$ is transverse mass andequal to $\sqrt{p_t^2 + m^2}$. However, there is an additional systematic increase in the ratios as the number of nucleons involved in the collisions increases. The Si + Au ratios are substantially larger than typical values observed in either p-p or p-Pb collisions. The ratio at low $p_\perp \equiv p_t$ is ≈ 20% which is in agreement with the integral ratio presented at QM87 [83].

The K^-/π^- ratios exhibit similar tendencies, but the overall magnitude of the ratios is reduced for all collision systems. There are large discrepancies in values of measured negative K to π ratios for p-p collisions, particularly at low $p_\perp$. The integral ratios are, of course, dominated by the values at low $p_\perp$, with mean values for p-p lying in the 2 - 4% range, and Si + Au exhibiting somewhat higher values of 5-6%. At high $p_\perp$ the heavy ion data systematically exceed typical values from p-p and p-A.

The measured ratio is about 20 % K^+/π^+ and 5 % K^-/π^- , the expected ratio for K^+/π^+ and K^-/π^- is about 5 % for proton proton and proton antiproton collisions [84]. The measured ratio is fourth times higher than expected for K^+/π^+ , this result has stimulated the speculation that a quark-gluon plasma might have been formed in the collisions.

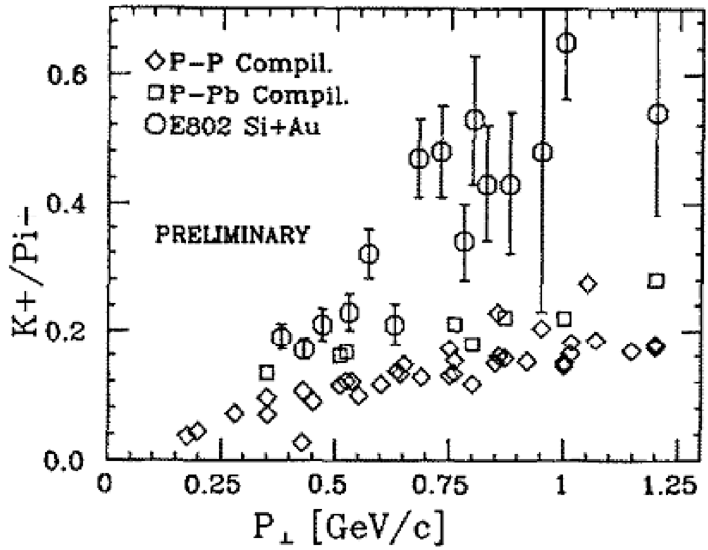

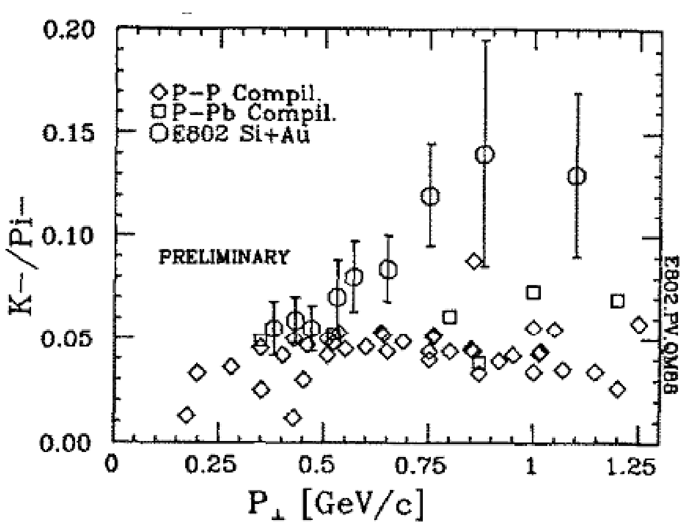

Figure (5-1): Compilation of K^{+}/π^{+} ratios vs. p_t in p-p and p-A collisions at AGS energies compared to Si- Au. [82]

First experimental results in SPS (Pb + Pb) at energy 158 GeV, and AGS (Au - Au) at energy 114 GeV, have suggested anomalies in pion and strangeness production may be located between these energies [85]. The study of this hypothesis is the motivation for a dedicated energy scan at energy SPS [86].

A. V. Afanasiev et al, (NA49 Collaboration), this experiment studies Pb - Pb collisions at 158 GeV per nucleon, studied the kaon-to-pion ratio by using particle identification dE/dx [87]. The main conclusions were: no nonstatistical fluctuations are observed and they deduce an upper limit of strength of nonstatistical fluctuations $\sigma_{non-stat}$ < 4.0 % for fluctuations occurring in every event at the 3σ level. The fluctuations are therefore very small relative to the twofold strangeness enhancement, indicating that the dynamical evolution of individual events proceeds in a very similar fashion. The fluctuations observed in Pb - Pb collisions are significantly smaller than those expected for an independent superposition of nucleon-nucleon collisions.

A. V. Afanasiev *et al.*, (NA49 Collaboration) [88], they studied the energy dependence of kaon-to-pion ratio in central Pb - Pb collisions. Figures (5-2) and (5.3), shows the midrapidity and full phase kaon to pion ratio as a function of energy $\sqrt{s_{NN}}$, respectively [75, 79-85]. As shown in the figure, the K^-/π^- ratio increase with $\sqrt{s_{NN}}$, but for K^+/π^+ ratio a very different behavior is observed: a steep increase in the low energy region

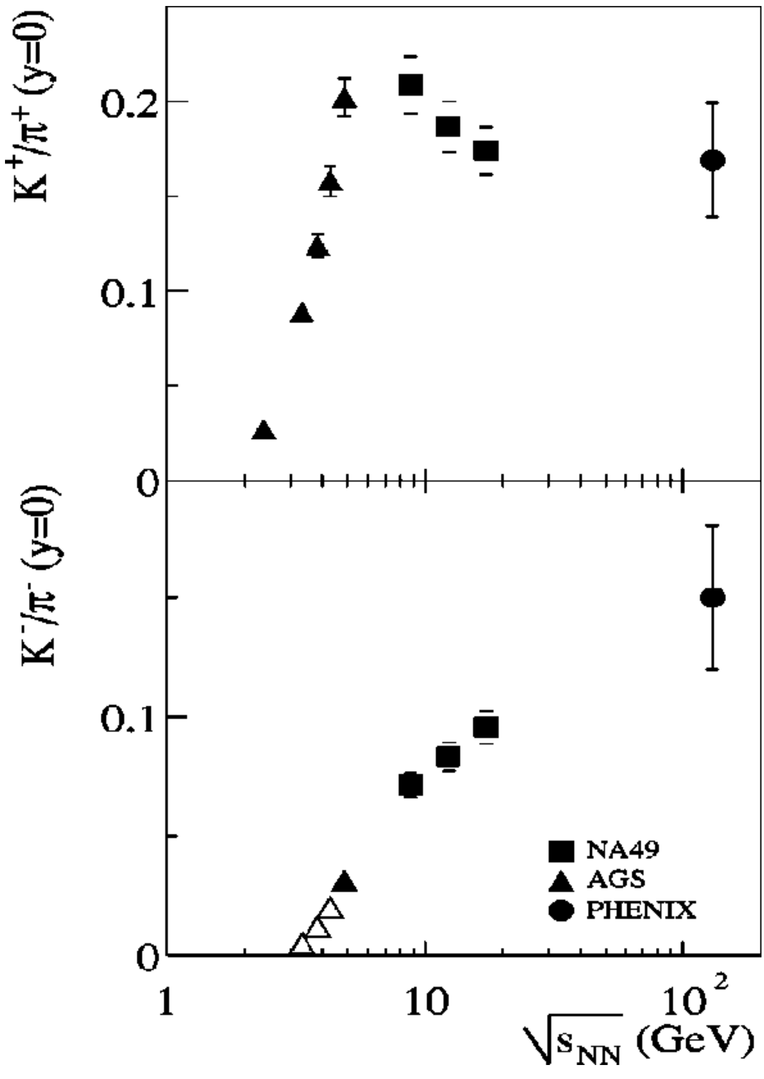

Figure (5-2): Energy dependence of the mid-rapidity K^+/π^+ and K^-/π^- ratios in central Pb-Pb and Au-Au C.

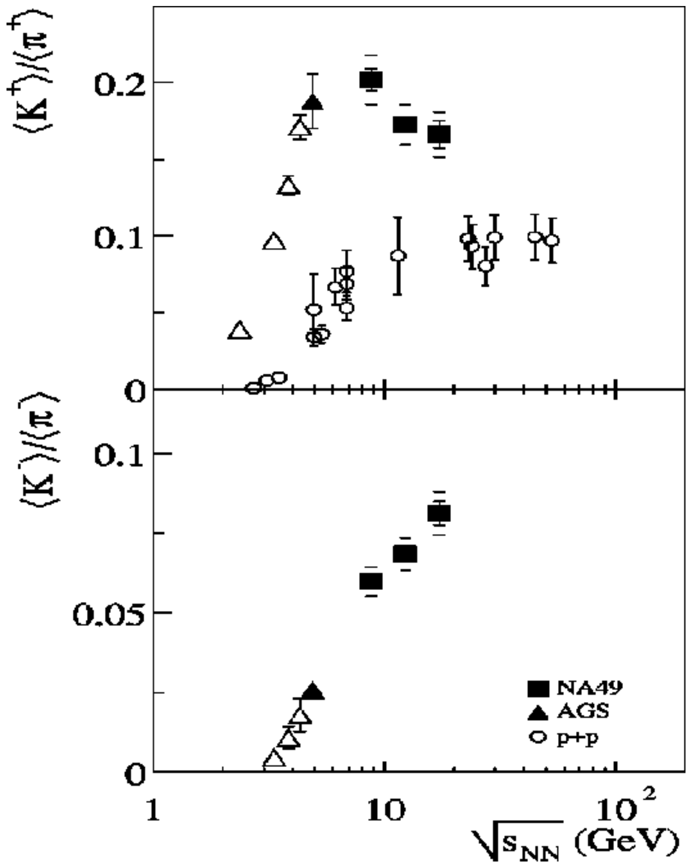

Figure (5-3): Energy dependence of full phase space $\langle K^{+}\rangle/\langle\pi^{+}\rangle$ and $\langle K^{-}\rangle/\langle\pi^{-}\rangle$ ratios in central Pb-Pb and Au-Au collisions. The data for p-p interactions are shown by open circles for comparison. Open triangles indicate the A-A results for which a substantial extrapolation was necessary [97]. The inner error bars on the NA49 points indicate the statistical uncertainty and the outer error bars the statistical and systematic uncertainty added in quadrature.

[89-93] is followed by a maximum around 40 A GeV. The measurement at RHIC indicates that the K^+/π^+ ratio stays nearly constant starting from the top SPS energy. For comparison, the results on the $\langle K^+\rangle/\langle\pi^+\rangle$ ratio in p-p interactions [85] are also shown in Figure (5-3).

Adler et al., (STAR Collaboration) [98], STAR experiment studies Au-Au collisions at $\sqrt{s_{NN}}$ = 130 GeV. The collaborators studied the K/p ratio as in Figure (5-4). This figure is a compilation of K/p results for central heavy-ion collisions. Since mid-rapidity $\pi^+/\pi^- \approx 1$ at RHIC [99], compared K^+/π^- results to K^+/π^+ collisions. The results of NA49 are indicated by squares. Open triangles indicate the A-A results for which preliminary data were used [96]. The errors on NA49 points are statistical and systematic errors are smaller than the symbol size. [88] results from lower energies. The K^-/π ratio steadily increases with $\sqrt{s_{NN}}$, while the K^+/π ratio in heavy-ion collisions sharply increases at low energies and the maximum value of K^+/π^+ occurs at $\sqrt{s_{NN}}$ ~ 10 GeV. Also, figure (5-4) showed parameterized p + p data (curves) and data from p - p [100, 101] and $\bar{p}-p$ [92] at high energies. The average of π^+ and π^- multiplicities, $\langle\pi\rangle$, used to form the ratios in order to take into account the isospin effect. The main conclusion for this work was, the measured K/p ratios at RHIC show an enhancement of about 50% over p - p and $\bar{p}-p$ collisions at similar energies.

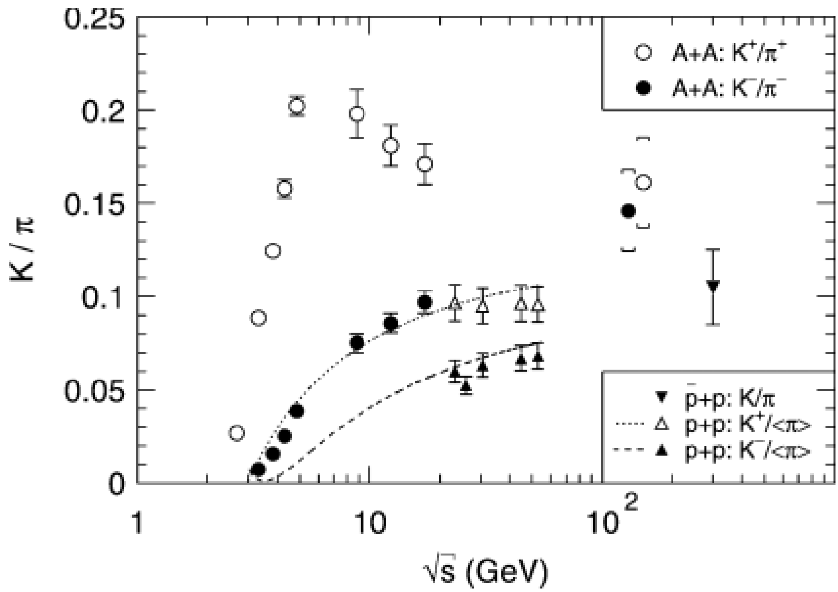

Figure (5-4): Mid- rapidity K/π ratios versus $\sqrt{s_{NN}}$. The curves are parameterization to p - p data [90, 91]. The error bars shows statistical errors. The systematic errors on the STAR data are indicated by the caps. The STAR K^{+}/π point is displaced in $\sqrt{s_{NN}}$ for clarity. [98]

B. I. Abelev et al., (STAR Collaboration) [103], studied K/π ratio with different energies $\sqrt{s_{NN}}$ = 19.6, 62.4,130 and 200 GeV. They found that the fluctuation in K/π ratio for central Au-Au collisions are of the same order as fluctuations observed in central collisions Pb-Pb collisions at $\sqrt{s_{NN}}$ = 6.3, 7.6, 8.8, 12.3, and 17.3 GeV, but the Pb-Pb results show a stronger incident energy dependence.

I.C. Arsene *et al.*, (BRAHMS Collaboration), this collaboration studies the collisions between Au-Au at energy $\sqrt{s_{NN}} = 62.4$ GeV [104]. They showed the rapidity dependence of the K/p ratio as in Figure (5-5). Because the rapidity intervals where the yields of the two species were extracted are not the same at forward rapidity, they used a linear interpolation procedure between the closest covered points to obtain the meson yields for additional points in rapidity. They checked this procedure by assuming Gaussian rapidity distributions and found very similar results. The K^+/π^+ ratio was found to be 0 .159 ± 0.011 at mid-rapidity and is almost constant as a function of rapidity. The K^-/π^- ratio has a value of 0.13 ±0.01 at mid-rapidity and shows a steep decrease for y > 2.5 with a value of ~ 0.05 at y = 3.2. The different rapidity dependence of the positive and negative K/p ratios is similar to that found in central Au + Au collisions at = 200 GeV [105] but the difference between the two ratios is three times larger at y = 3.

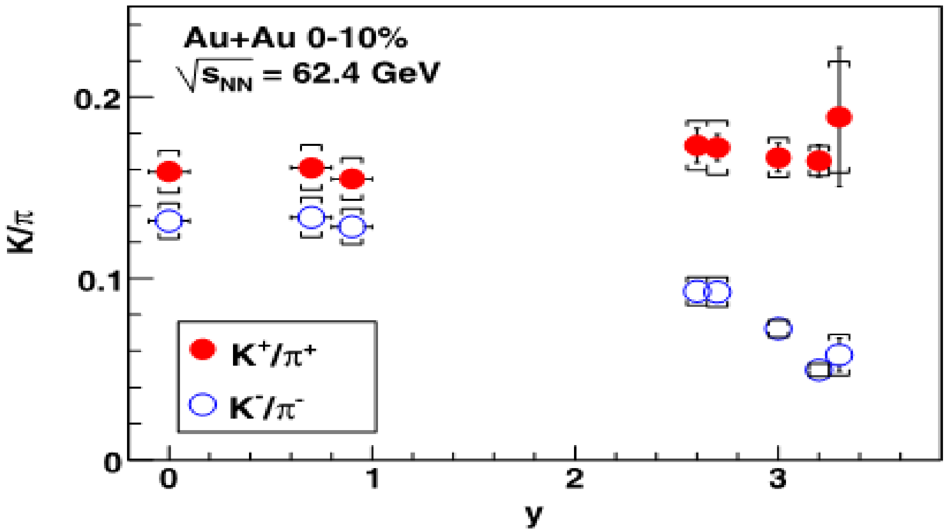

Figure (5-5): (Color online.) Rapidity dependence of the K/π ratios in 0–10% central Au + Au collisions at = 62.4 GeV. The error bars are statistical errors and the square brackets show the systematic uncertainties due to the yield extrapolation at low p_t.

K. Aamodt et al., ALICE Collaboration, this collaboration studies p-p and heavy ion collisions at different energies [106]. The collaborators studied the K/π ratio as a function of $\sqrt{s}$ both in pp (full symbols, [107, 108, 109]) and in $\bar{p}p$ (results from TEVATRON [110-112]) (open symbols) collisions. For most energies, $(K^+ + K^-)/(\pi^+ + \pi^-)$ is plotted as shown in figure (5-6), but for some cases only neutral mesons were measured and K^0/π^0 is used instead. The p_t -integrated $(K^+ + K^-)/(\pi^+ + \pi^-)$ ratio shows a slight increase from $\sqrt{s}$ = 200 GeV (K/π = 0.103 ± 0.008) to $\sqrt{s}$ = 900 GeV (K/π = 0.123 ± 0.004 ± 0.010) [111], yet consistent within the error bars. The results at 7 TeV will show whether the K/π ratio keeps rising slowly as a function of $\sqrt{s}$ or saturates.

M. Floris et al., ALICE collaboration [113], they studied the p_t-integrated K^-/π^- ratio as a function of $dN_{ch}/d\eta$ in the case of Pb-Pb collisions at energy $\sqrt{s}$ = 2.76 TeV, also compared with results obtained RHIC and to pp measurement, as shown in figure (5-7). The K^-/π^- ratio follows nicely the trend from lower energies.

In the present work, we study the kaon-to-pion ratio in proton-proton collisions, and trying to get a connection between hadron-hadron and heavy ion collisions.

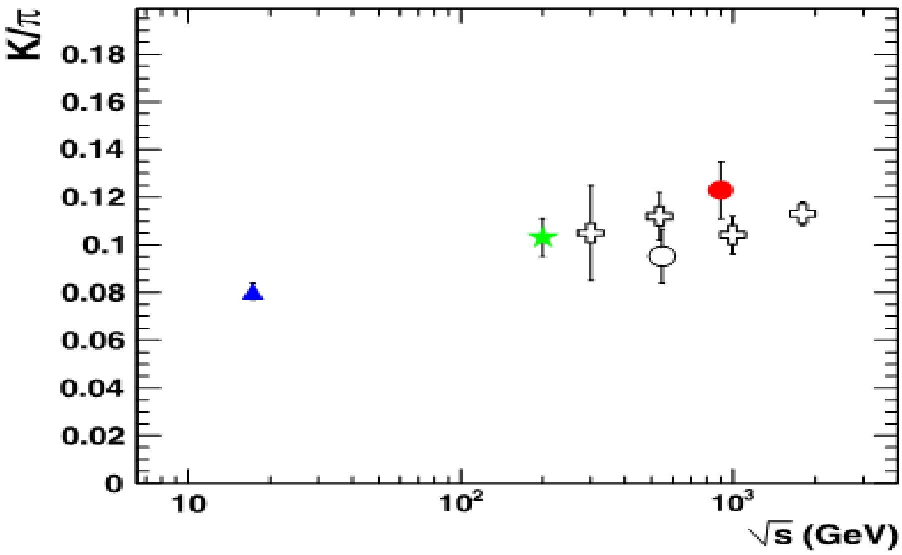

Figure (5-6): (Color online) Ratios $(K^+ + K^-)/(\pi^+ + \pi^-)$ and K^0/π as a function of $\sqrt{s}$. Data (full symbols) are from pp collisions, (at $\sqrt{s}$ = 17.9 GeV by NA49 [108, 109], at $\sqrt{s}$ = 200 GeV by STAR [107], and at $\sqrt{s}$ = 900 GeV = 900 ALICE, and (open symbols) from $\bar{\mathrm{p}}\mathrm{p}$ interaction (at $\sqrt{s}$ = 560 GeV by UA5 [111] and at the TEVATRON by E735 [110,112].

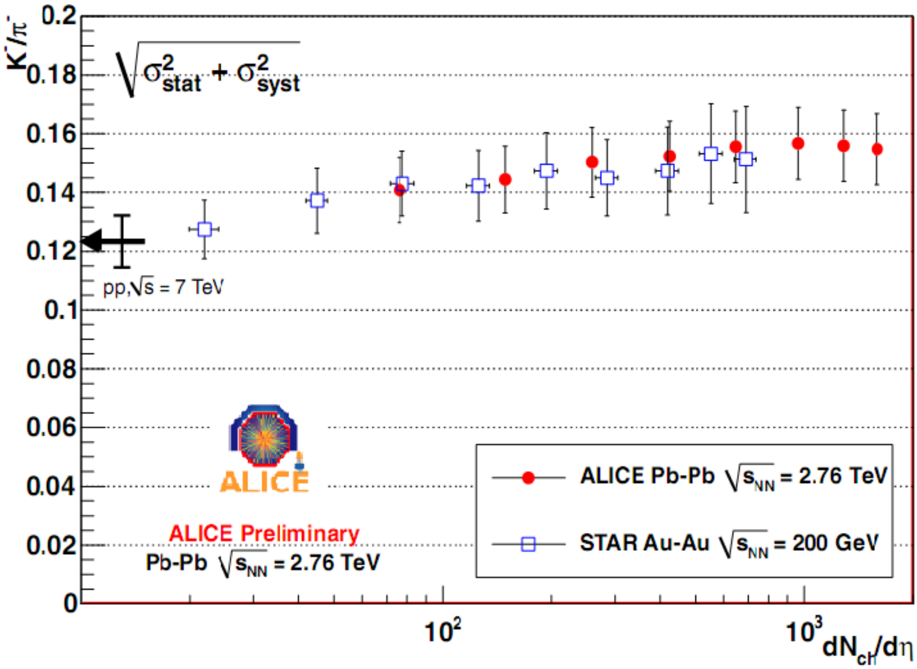

Figure (5-7): The K^- / π^- ratio as a function of $dN_{ch} / d\eta$.

(5-2) Dataset and Monte Carlo:

The dataset used in this analysis is:

/MinimumBias/Run2010B-Apr21ReReco-v1/RECO

The runs and luminosity sections used for the analysis have been certified by the corresponding JSON files:

Cert_136033-149442_7TeV_Apr21ReReco_Collisions10_JSON.txt

Monte Carlo:

For MinimumBias

- /MinBias_TuneZ2_7TeV-pythia6/Fall11-NoPileUp_START44_V9B-v2/GEN-SIM-RECODEBUG
- /MinBias_Tune4C_7TeV-pythia8/Summer11-NoPU_START42_V11-v1/GEN-SIM-RECO
- /MinBias_TuneZ2star_HFshowerLibrary_7TeV_pythia6/Summer12-LowPU2010_DR42_NoPileUp_START42_V17C-v1/GEN-SIM-RECO

For High multiplicity:

- /castor/cern.ch/user/m/mohammed/MC_HighMutli_Pythia6_Z2/MC_HighMutli_Pythia6_Z2_new/

- /castor/cern.ch/user/m/mohammed/MinBias_Tune4C_7TeV-pythia8

- /castor/cern.ch/user/m/mohammed/MC_PYTHIA8/

Track selections which used in this analysis are:

- quality mask passes high purity requirement: trk.quality(”highPurity”)
- relative pT uncertainty below 5%: trk.ptError()/trk.pt()< 0.05
- at least 5 hits on the track: trk.numberOfValidHits>= 5
- absolute impact parameter cuts: abs(trk.dz)<0.2 cm && abs(trk.d0<0.2) cm
- relative impact parameter cuts: abs(dxy/dxyerror) < 3 && abs (dz/dzerror) < 3.

where dz and dxy are calculated with respect to vertices.

(5-3) Unfolding

The unfolding method which used in the present work is summarized in the below steps:

1. Obtaining the total number of kaon and pion inside a certain region at Reco level and generator level. To get the number of kaon at reconstruction level:
    - Firstly, we plotted the relation between momentum p (GeV) and dE/dx as in figure (5-10).
    - Determine the region which the kaons concentrated in it, also another one for pion, these two regions have the same momentum boundaries.

To get the number of Kaons at generator level:

- ➢ In this case we used the code or IDs of kaon and pion according the particle data group[1]. At the same momentum regions as in the RECO level, we got the number of kaons and pions.

2. Getting the ratio between (Reco/Gen) for kaon and pion separately.
3. Multiplying the data of kaon with the ratio related to it and the same for pion.

To study if the Reco/Gen values changing with change of multiplicity, the events are divided in to 6 groups according to multiplicity. Plot two dimension histograms between the average of number of tracks and the ratio, as shown in figure (5-8) for kaon trigger and figure (5-9) for pion. From these figures, we deduce that the ratio of Reco/ Gen is almost constant in the case of pion, but it is slightly change in the case of kaon.

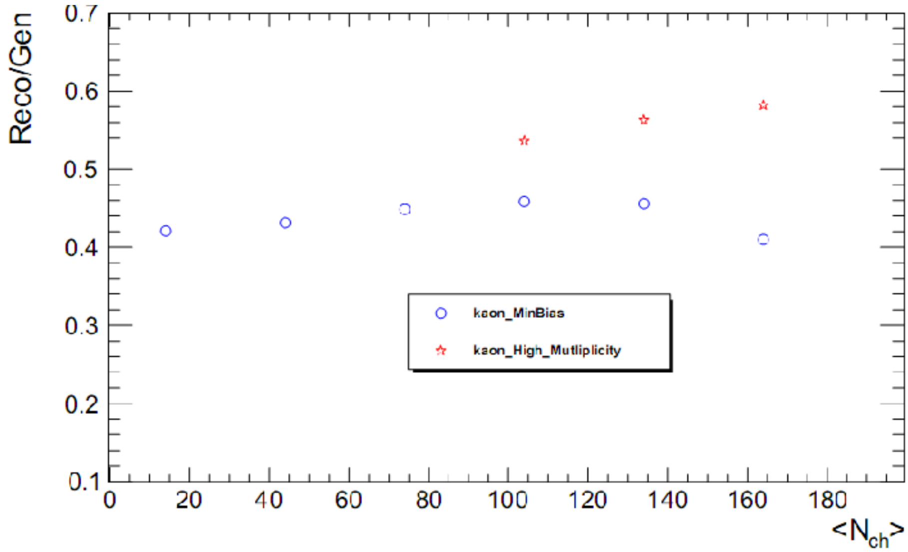

Figure (5-8): relation between average multiplicity and Reco/Gen for kaon.

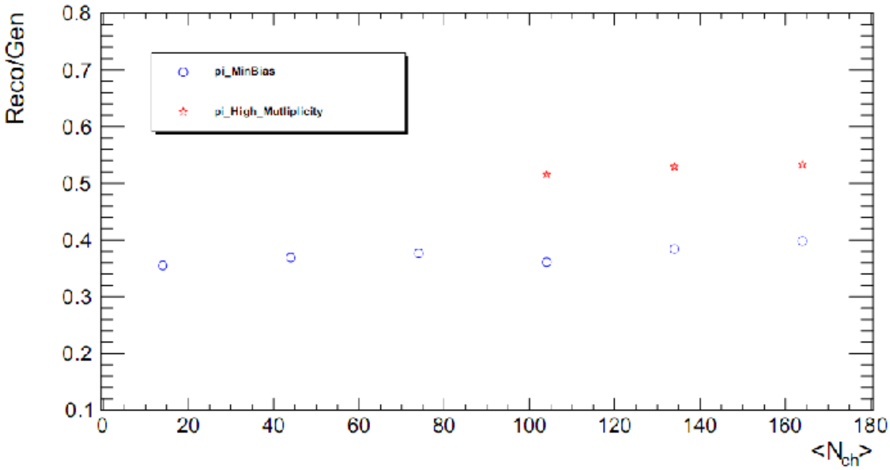

Figure (5-9): relation between average multiplicity and Reco/Gen for pion.

(5-4) Results:

In the present work, we try to study the relation between ratio (K/π) and multiplicity in pp collisions at 7 TeV. Firstly, to get this ratio we plot the relation between momentum and energy loss as in figure (5-10). Secondly, we determine the two regions of kaon and pion as shown in figure (5-10). Finally, to see the distributions of kaon and pion, we illustrate the transverse momentum (pt) distribution for pion and kaon in a certain regions in the case of MinimumBias trigger and high multiplicity trigger. Also we get the same plots for different MC samples for minimumBias and high multiplicity as shown in figures (5-11), (5-12), (5-13) and (5-14).

Figures (5-15)-(5-22), show the two dimensions praph between multiplicity (number of tracks) and number of (kaons & pions) inside a certain regions as shown in figure (5-10) for data and MC.

For getting the relation between ratio between kaon/pion and multiplicity, we have to plot the two dimension histograms between number of kaon and multiplicity as shown in figures (5-15) and (5-22) for MinimumBias trigger and high multiplicity triggers respectively and also anther plot between number of pion and multiplicity as shown in figures (5-18) and (5-21) for MinimumBias trigger and high multiplicity triggers respectively. The next step, we change these two dimension histograms for kaon and pion to one dimension histograms by getting profile with respect to x axis, figure (5-23) and (5-25). After division we get figures (5-23) for minimumBias trigger and (5-24) for high multiplicity triggers.

Figure (5-21) shows the relation between the multiplicity and the K/π ratio in the case of minimumBias trigger. We see that, at low multiplicity the ratio is almost constant, but increases at high multiplicity events.

From the figure (5-24), and (5-26), we see that the ratio of <K>/<π> is decreasing rapidly with increasing of multiplicity, and after that the behavior of ratio is almost constant. Also the ratio in real data is bigger than the ratio in MC with different PYTHIA tunes in the two cases of triggers.

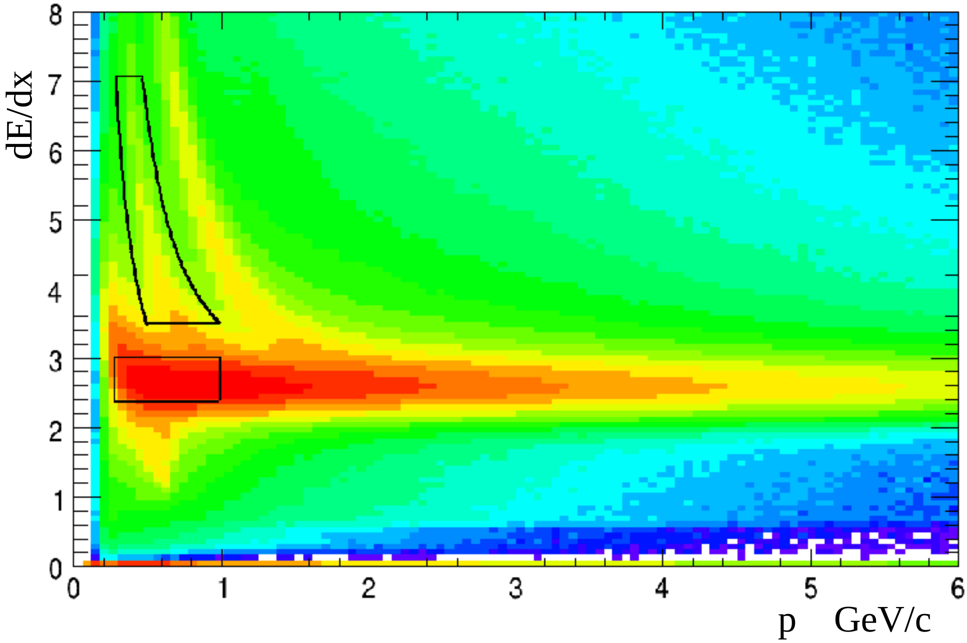

Figure (5-10): Two dimensions plot between momentum and dE/dx.

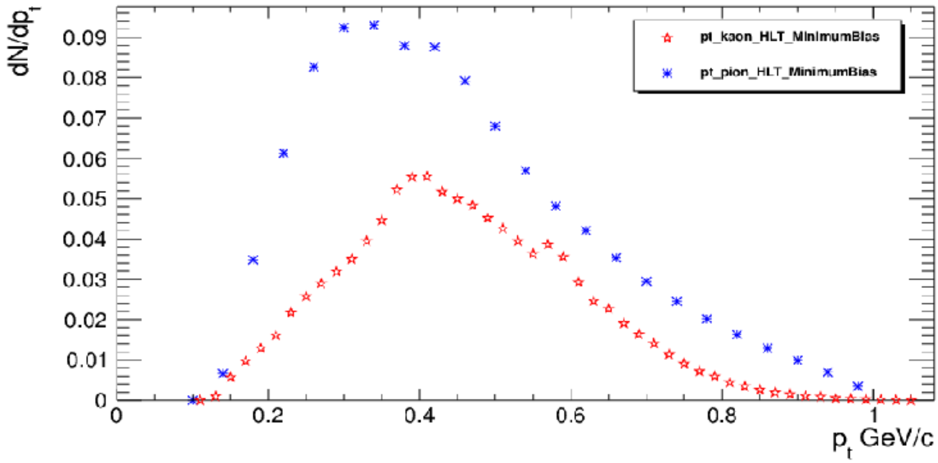

Figure (5-11): pt distributions for kaon and pion in the region indicated by black lines in figure (5-10) in the case of MinimumBias trigger.

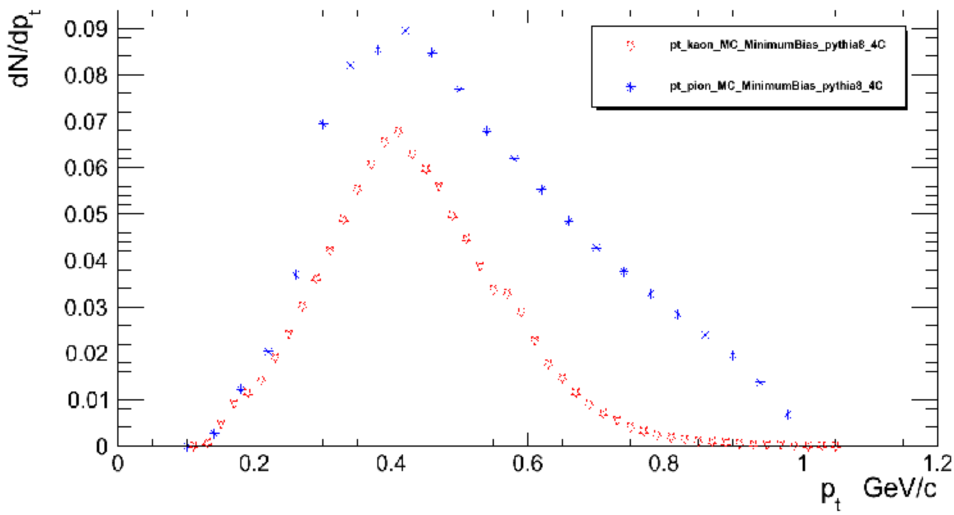

Figure (5-12): pt distributions for kaon and pion in a certain region in the case of MC MinimumBias.

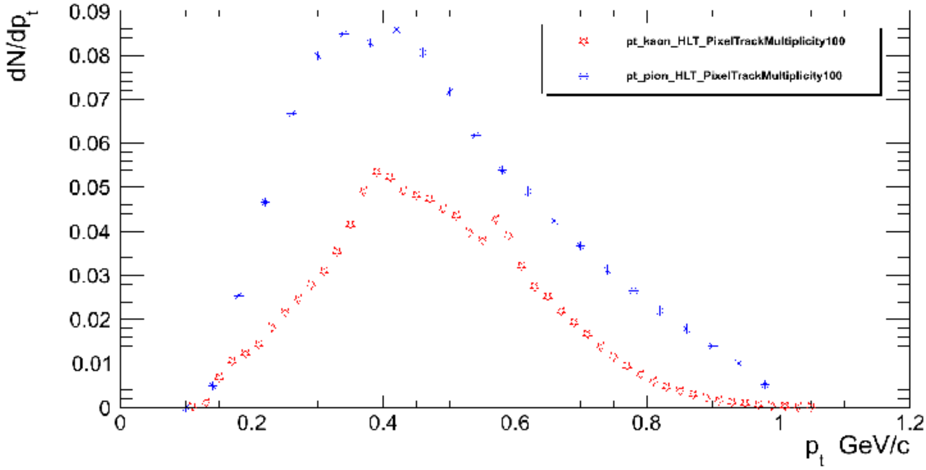

Figure (5-13): pt distributions for kaon and pion in a certain region in the case of high multiplicity trigger.

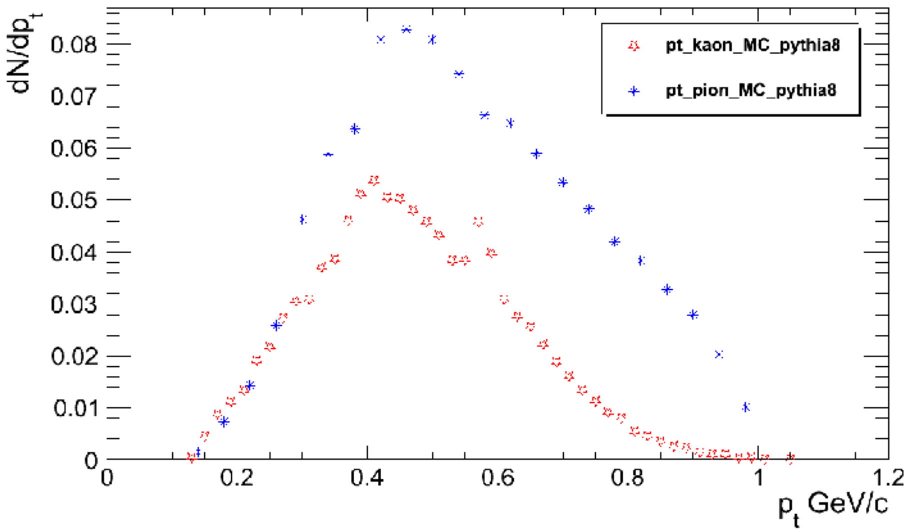

Figure (5-14): pt distributions for kaon and pion in a certain region in the case of MC for high multiplicity events.

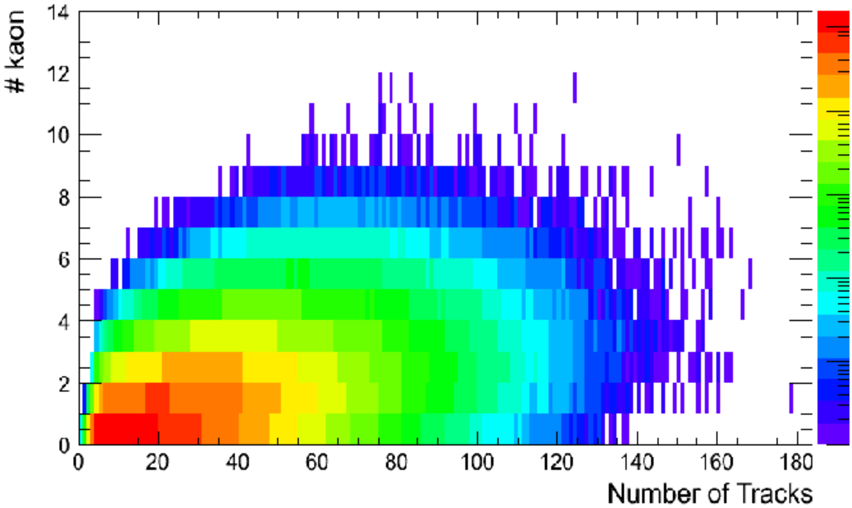

Figure (5-15): Two dimensions graph between number of tracks per event and number of kaons per event in the case of applying HLT_MinimumBias.

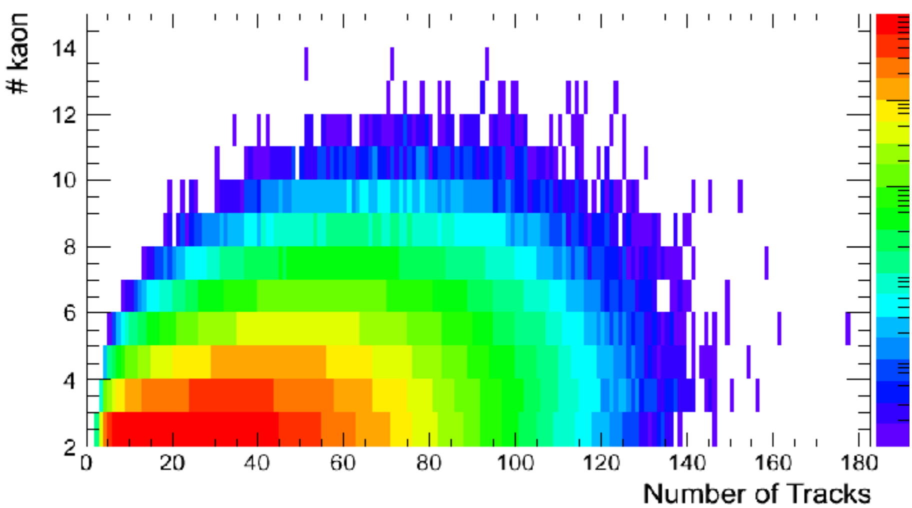

Figure (5-16): Two dimensions graph between number of tracks per event and number of kaons per event for Monte Carlo with event generator Pythia6 tune Z2.

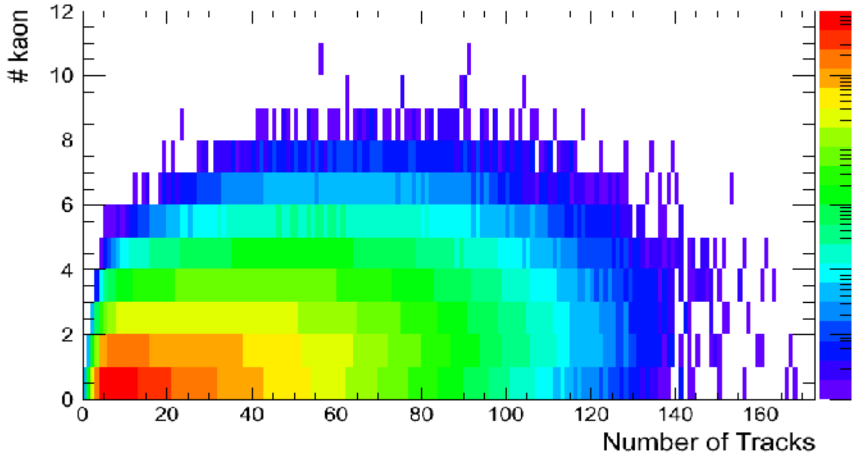

Figure (5-17): Two dimensions graph between number of tracks per event and number of kaon per event for Monte Carlo with event generator Pythia8 tune 4C.

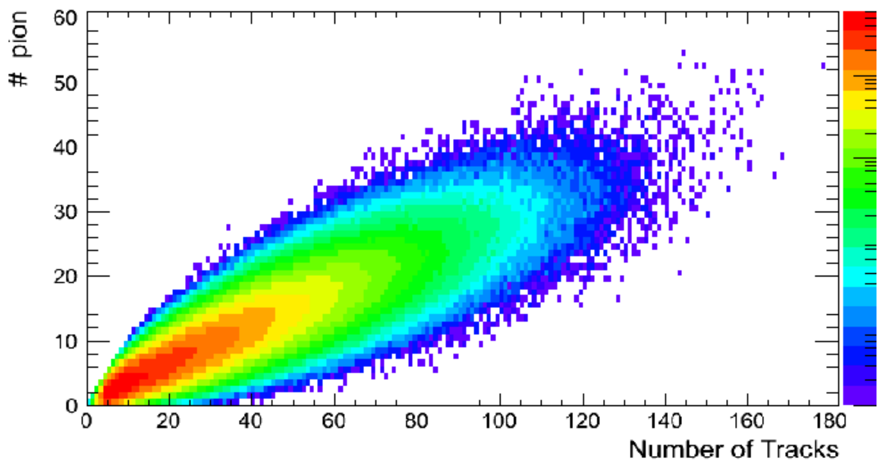

Figure (5-18): Two dimensions graph between number of tracks per event and number of pions per event in the case of applying HLT_MinimumBias.

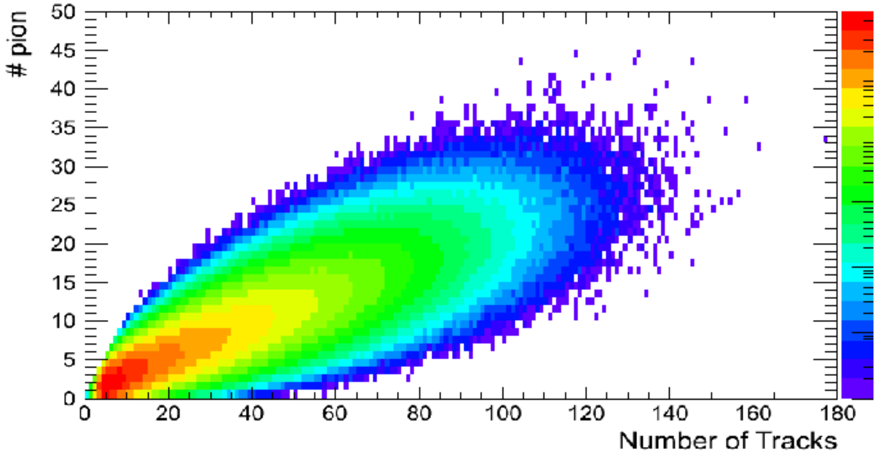

Figure (5-19): Two dimensions graph between number of tracks per event and number of pions per event for Monte Carlo with event generator Pythia6 tune Z2.

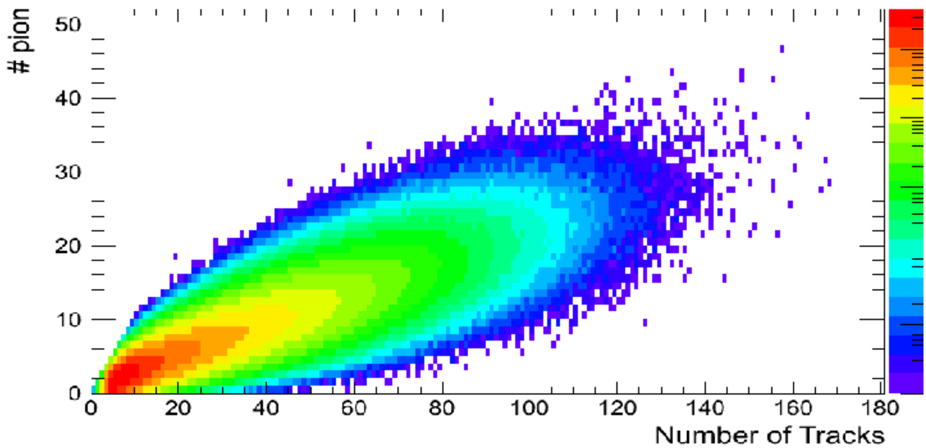

Figure (5-20): Two dimensions graph between number of tracks per event and number of pions per event for Monte Carlo with event generator Pythia8 tune 4C.

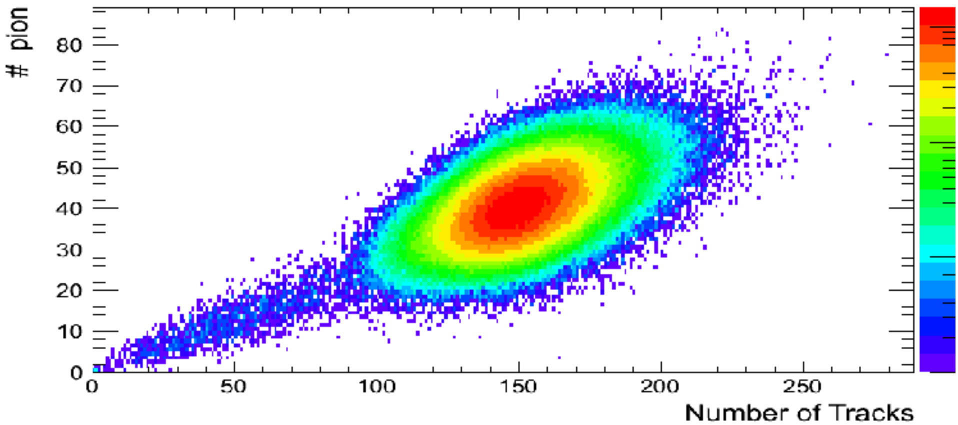

Figure (5-21): Two dimensions graph between number of tracks per event and number of pions per event for HLT_PixelTrackMultipicity100.

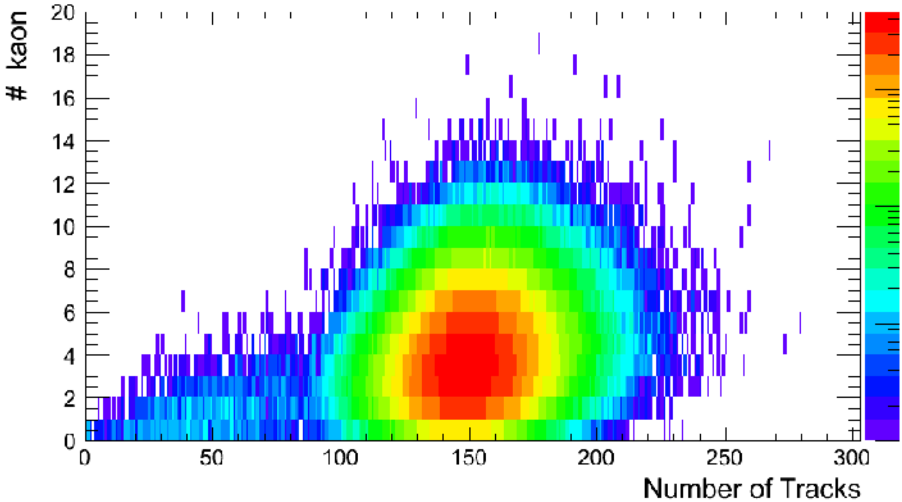

Figure (5-22): Two dimensions graph between number of tracks per event and number of kaons per event for HLT_PixelTrackMultipicity100.

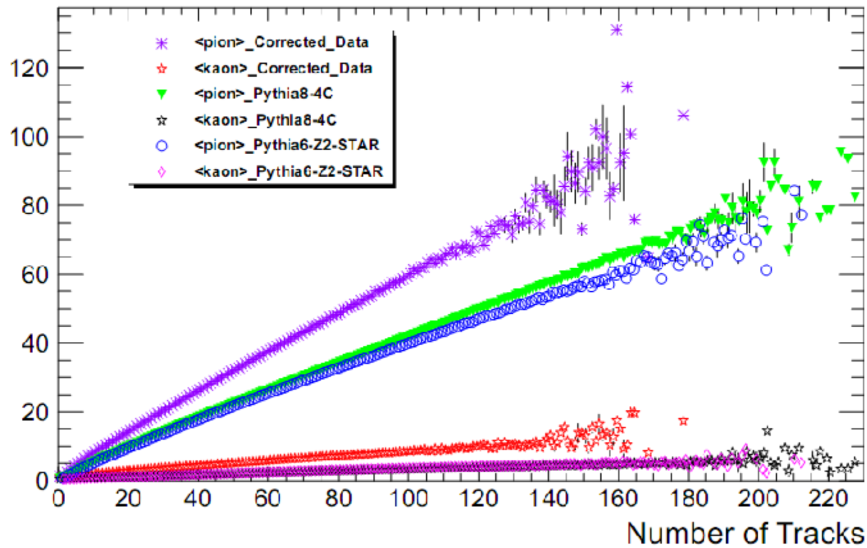

Figure (5-23): the relation between number of tracks and average number of kaons and pions per events for corrected data and different MCs, in the case of MinBias.

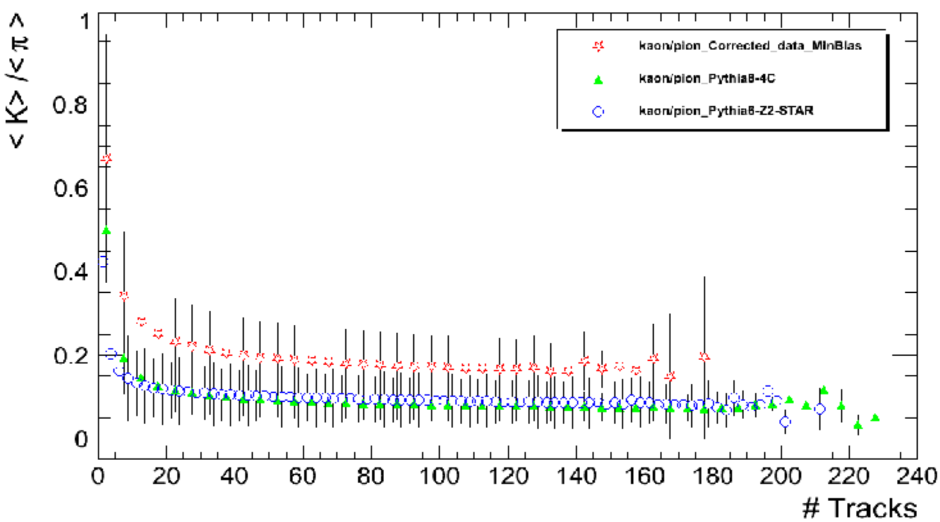

Figure (5-24): relation between multiplicity and <K>/<π> ratio in the case of HLT_MinimumBias trigger.

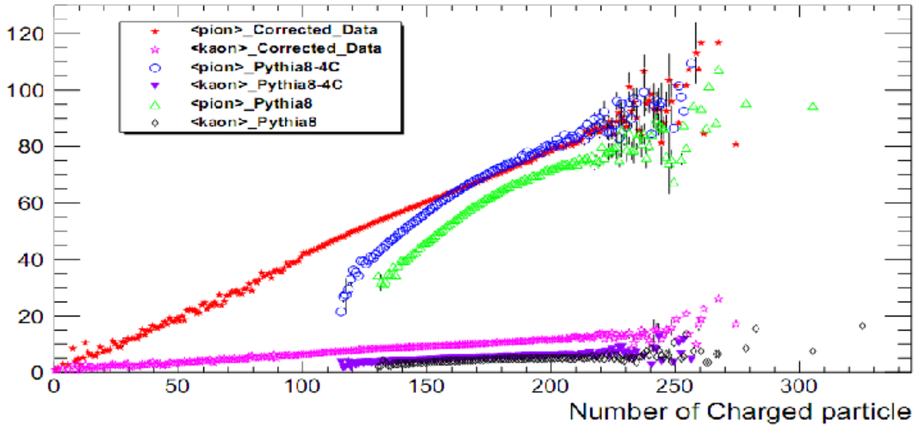

Figure (5-25): the relation between number of tracks and average kaons and pions per events for corrected data and different MCs, in the case of HLT_PixelTrackMulripliciy100 trigger.

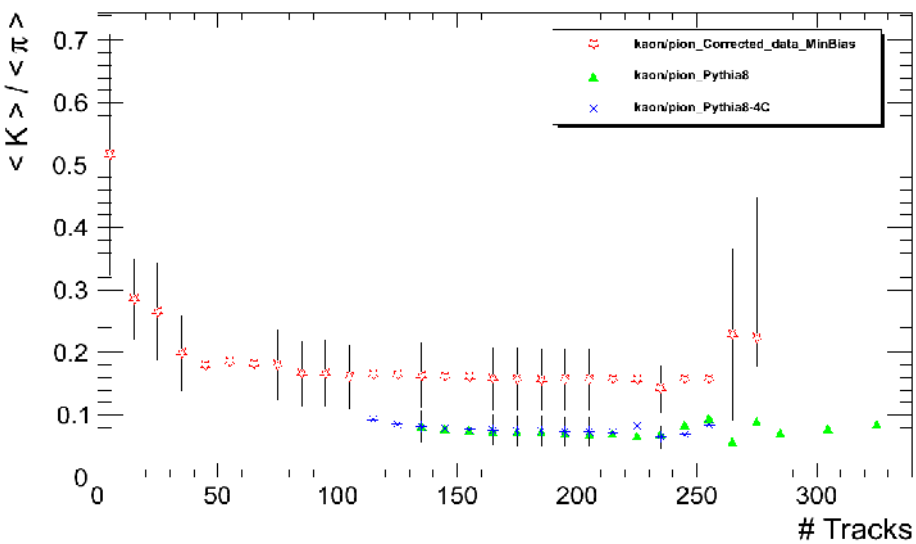

Figure (5-26): relation between multiplicity and K/π ratio in the case of HLT_PixeltrackMultipicity100 trigger.

Conclusion

Conclusions

This work is divided into two parts. The first one is studying the maximum track density inside a small interval with respect to pseudorapidity and rapidity. The main conclusions for this part are:

<u>In the case of minimumBias trigger</u>:

- The data still fitting with the same functions as previous work.
- We did not find events after exponential line…..

<u>In the case of high multiplicity trigger,</u>

- Also the data is still fitting with the same function as previous work.
- We found some events after exponential line in the case of studying the maximum track density inside widows 0.1, 0.2 and 0.5 with respect to pseudorapidity and rapidity.
- We found a lot of events with tracks more than 15 in windows 0.1 w. r. t. pseudorapidity.

The second part of the present work is studying the relation between K/π ratio and multiplicity. The main conclusions are:

- The average number of kaon $< K >$ is increasing with increase in number of track per event, in the two different triggers (minimumBias and PixelTrackMultiplicity100).

This behavior in agree with MC. But that average is slightly high in data.

- The average number of pion < π > is increasing with increase of multiplicity (number of tracks per event) in the two different triggers (minimumBias and PixelTrackMultiplicity100). This behavior in agree with MC. But that average is slightly high in data.
- The ratio between average number kaons < K> and average number of pions < π > is sharp decreasing with increasing number of tracks per events after that a plateau regions this behavior is the same in two triggers (minimumBias and PixelTrackMultiplicity100). PYTHIA with different tunes (4C and and Z2-STAR) have the same action of data.
- The ratio between average number kaons < K> and average number of pions < π > is a round 0.17 in case of triggers (minimumBias and PixelTrackMultiplicity100), and this ratio in slightly low in case of MC.

====================================

References

References

[1] K. Nakamura *et al.* (Particle Data Group), J. Phys. **G** 37, 075021 (2010) and 2011 partial update for the 2012 edition.

[2] R. K. ELLIS et al.,"QCD and Collider Physics", 1996, Cambridge University Press.

[3] S. NARISON,"QCD as a Theory of Hadrons: From Partons to Confinement", 2004, Cambridge University Press.

[4] G. Dissertori, I. G. Knowles, and M. Schmelling, High energy experiments and theory, Oxford, UK: Clarendon (2003) 538 p. 11, 16, 17.

[5] D. J. Gross and F. Wilczek, Phys. Rev. Lett. **30**, 1343 (1973).

[6] A. Giovannini and L. Van Hove, Z. Phys. **C 30**, 391 (1986) .

[7] E.A. De Wolf, I.M. Dreminb, W. Kittel, Phys. Reports **270**, 1 (1996).

[8] P. Carruthers, Phys. Rev. **A 43**, 2632 (1991).

[9] F.C. Winkelman et al., Phys. Lett. **B 56**, 101 (1975).

[10] L. FOB, Phys. Rep. **22 C**, 1 (1975).

[11] J. Whitmore, Phys. Rep. **27 C**, 187 (1976).

[12] R.E. Ansorge et al. (UA5), Z. Phys. **C 37**, 191 (1988).

[13] S.R. Amendolia et al., Nuovo Cimento **A 31**, 19 (1976).

[14] Ch. Fuglesang, Ph.D. Thesis, University of Stockholm (1987).

[15] G.J. Alner et al. (UA5), Nucl. Phys. B 291, 445 (1987).

[16] B. Andersson, G. Gustafson and B. Nilsson-Almqvist, Nucl. Phys. B 281 (1987) 289; Lund preprint LUTP 87-6.

[17] H.U. Bengtsson and T. Sjöstrand, Comput. Phys. Commun. 46, 43 (1987).

[18] J.L. Bailly et al. (NA23), Z. Phys. C 40, 13 (1988).

[19] A. Breakstone et al., Phys. Lett. 114 B, 383 (1982).

[20] B. Andersson, G. Gustafson, I. Holgersson and 0. Masson, Nucl. Phys. B 178, 242 (1981); T. Sjöstrand, Comput. Phys. Commun. 39, 347 (1986); T. Sjöstrand and M. Bengtsson, Comput. Phys. Commun. 43, 367 (1987).

[21] A. Capella, Proc. Europ. Study Conf. on Protons and Soft Hadronic Int., Erice, R.T. Van de Walle (ed.) (World Scientific, Singapore, 1982) p. 199; E.A. De Wolf, Proc. XV Int. Symp. on Multiparticle Dynamics, Lund,

Sweden 1984, eds. G. Gustafson and

C. Peterson (World Scientific, Singapore, 1984) p. 1.

[22] V.V. Aivazyan et al. (NA22), Z. Phys. C 51, 167 (1991)
.

[23] A.B. Kaidalov and K.A. Ter-Martirosyan, Sov. J. Nucl. Phys. 39, 979 (1984); ibid 40, 135 (1984); N.S. Amelin et al., Sov. J. Nucl. Phys. 51, 133 (1990); ibid 51, 535 (1990); N.S. Amelin, L.V. Bravina and L.N. Smirnova, Sov. J. Nucl. Phys**. 52**, 362 (1990).

[24] H. Satz, Rept. Prog. Phys. **63**, 1511 (2000).

[25] http://backreaction.blogspot.fr/2006/08/quark-gluon-plasma.html

[26] E. Shuryak, Nucl. Phys. **A 566**, 559c (1994).

[27] H. Satz, Phase Transition in QCD, Nucl. Phys. **A 681**, 3 (2001).

[28] S. Gottlieb, Journal of Physics: Conference Series 78, 012023 (2007).

[29] U. Heinz, The Little Bang: Searching for quark-gluon matter in relativistic heavy ion collisions, Nucl. Phys. A 685 414-431 (2001)

[30] Giacomo Ortona, PhD thesis, Universit`a degli Studi di Torino (2012).

[31] R. Baier, Y. L. Dokshitzer, A. H. Mueller, S. Peigne, and D. Schi□, "Radiative energy loss and p(T) broadening of high-energy partons in nuclei," Nucl.Phys., vol. B484, pp. 265–282, 1997.

[32] R. Baier, Y. L. Dokshitzer, A. H. Mueller, S. Peigne, and D. Schi□, Nucl.Phys., vol. B483, pp. 291–320, 1997.

[33] S. Chatrchyan et al, Phys.Rev., vol. C84, 024906 (2011).

[34] G. Aad et al., , Phys. Rev. Lett., vol. 105, 252303(2010).

[35] A. Bialas, M. Bleszynski, and W. Czyz, Nucl. Phys., vol. B111, 461 (1976).

[36] T. Matsui and H. Satz, Phys. Lett B 178, 416(1986).

[37] M. C Abreu *et al.*, Phys. Lett B410, 337 (1997).

[38] M. C Abreu *et al.*, Phys. Lett B450, 456(1999).

[39] M. C Abreu *et al.*, Phys. Lett B477, 28 (2000).

[40] ALICE Collaboration, J. Phys. G: Nucl Part. Phys. 30, 1517 (2004).

[41] J. Rafelski and J. Letessier, J. Phys. Conf. Ser. 50, 176 (2006).

[42] J. Ollitrault, Phys. Rev. **D46**, 229 (1992).

[43] J. Daniel Tapia Takaki, PhD thesis, University of

Birmingham (2007).

[44] P. Huovinen, Phys. Lett. B503, 58 (2001).

[45] P. Sorensen, J. Phys G30, S217 (2004).

[46] R. Senlling, Eur. Phys. J. C49, 87 (2007).

[47] G. Bachy et al., CERN/LEP-DI-IM-RF (1989).

[48] L. Evans and P. Bryant, JINST 3 (2008).

[49] ALICE Collaboration, The ALICE experiment at the CERN LHC, JINST 3, S08002. 34 (2008)

[50] LHCb Collaboration, The LHCb Detector at the LHC, JINST 3, S08005. 34 (2008)

[51] ATLAS Collaboration, The ATLAS Experiment at the CERN Large Hadron Collider, JINST 3, S08003. 35 (2008)

[52] CMS Collaboration, CMS Physics Technical Design Report, Volume I: Detector Performance and Software, vol. LHCC-2006-001 of Technical Design Report CMS. CERN, Geneva, 2006. 35, 144.

[53] CMS Collaboration, The CMS experiment at the CERN LHC, JINST 3, S08004. 37 (2008)

[54] T. Han, D. Rainwater, Physics Letters B 463, 93(1999).

[55] O. Bruning, P. Collier, P. Lebrun, S. Myers, R. Ostojic,J. Poole, P. Prounlock, CERN-2004-003; LHC Design Report Vol. 1, Ch. 2: Beam Parameters and Definitions. Technical report, 2004.

[56] Bayatian, 2005, CMS Computing Technical Design Report 2005-023 CERN/LHCC.

[57] K.I. Aleksejeva et al., J. Phys. Soc. Jpn 17, 409(1962).

[58] N. Arata, II Nuovo Cimento 43A, 455(1978).

[59] N.A. Marutyan et al., Sov. Nucl. Phys. 29, 804(1979).

[60] G.A. Apanasenko et al., JETP 30, 145(1979).

[61] JACEE Collaboration, T.H. Burnatt et al., Phys. Rev. Lett 50, 2062(1983).

[62] P. Carlson, Proc. 4th Topical Workshop on 15p collider physics (Bern, March 1984), CERN Report 84-09 (1984).

[63] M. Adamus et al., NA22 Collaboration, Phys. Lett. B 185, 200 (1987), CERN-EP-86-218.

[64] Franco Fabbri, paper presented at 23rd Rencontre de Moriond. Particle Physics Meeting, Les Arcs, France, 13 - 19 Mar 1988, pp.197-206, DFUB-88-20.

[65] J.B. Singh and J.M. Kohli, Phys. Lett B 261, 155(1990).

[66] N.M. Agababyan el al., EHS /NA22 Collaboration, Phys. Lett. B 389, 397 (1996).

[67] V. Khachatryan et al., CMS Collaboration, JHEP 1009, 0.91 (2010).

[68] John Adams et al., Nucl. Phys., A757, 102(2005).

[69] B. I. Abelev et al. (STAR Collaboration), Phys. Rev. C 80, 064912 (2009).

[70] A. Adare et al. (PHENIX Collaboration), Phys. Rev. Lett. 104, 252301 (2010).

[71] V. Khachatryan et al. (CMS Collaboration), Eur. Phys. J. C 70, 1165 (2010), doi:10.1140/epjc/s10052-010-1491-3.

[72] CMS Collaboration, CMS Physics Analysis Summary CMS-PAS-TRK-10-001 (2010).

[73] G. D’Agostini, Nuclear Instruments and Methods in Physics Research A, 362, 487(1995).

[74] E. V. Shuryak, Phys. Rep. **61**, 71 (1980).

[75] J. Rafelski and Muller, Phys. Rev. Lett. 48, 1066 (1982).

[76] S. Soff et al., Phys. Lett B 471, 89(1999).

[77] V. Koch, A. Majumder, and J. Randrup, Phys. Rev. C 72, 064903 (2005).

[78] V. Koch, A. Majumder, an d J. Randrup, Phys. Rev. lett. 95, 182301 (2005).

[79] M. I. Gorenstein, M. Gazdzicki, and O.S Zozulya, Phys. Lett. B 585, 237 (2004).

[80] P. Koch, B Muller, and J. Rafelski, Phys. Rep. 142, 167(1986).

[81] U. Heinz, k. S. Lee and M.J. Rhodes-Brown, Phys. Rev. Lett. 58, 2292 (1987).

[82] P. Vincent et al. , (E802 Collaboration), Nucl. Phys. A 498, 67(1989).

[83] Proceedings QM87, H. Satz, H.J. Specht, R. Stock eds., Zeit. Phys. C38(1958).

[84] A. N. Diddens et al., Nuo. Cim. 31, 962 (1962) ; K. Alpgard et al., Phys. Lett. 115B, 65 (1982), and refs. therein.

[85] M. Gaździcki and D. Röhrich, Z. Phys. C 65, 215 (1995); M. Gaździcki and D. Röhrich, Z. Phys. C 71, 55(1996), and references therein.

[86] J. Bachler et al., NA49 Collaboration, Report Nos. SPSLC/P264 and CERN/SPSC 97, 1997.

[87] S. V. Afanasiev et al., (NA49 Collaboration), Phys. Rev. Lett. 86, 1965 (2001), hep-ex/0009053.

[88] S. V. Afanasiev et al., (NA49 Collaboration), Phys. Rev. C 66, 054902 (2002).

[89] L. Ahle *et al.*, E802 Collaboration, Phys. Rev. C **57**, 466(1998); **58**, 3523 (1998); **60**, 044904 (1999);

[90] L. Ahle *et al.*, E866 and E917 Collaboration, Phys. Lett. B **476**,1(2000).

[91] L. Ahle *et al.*, E866 and E917 Collaboration, Phys. Lett. B **490**, 53(2000);

[92] J. Barrette *et al.*, E877 Collaboration, Phys. Rev. C **62**, 024901 (2000);

[93] D. Pelte *et al.*, FOPI Collaboration, Z. Phys. A **357**, 215 (1997).

[94] K. Adcox *et al.*, PHENIX Collaboration, Phys. Rev. Lett. **88**, 42301 (2002);

[95] B. B. Back *et al.*, PHOBOS Collaboration, *ibid.* **87**, 102301 (2001).

[96] J. L. Klay, E895 Collaboration, Ph.D. thesis, University of California, Davis, 2001.

[97] The ratios at low AGS energies were calculated based on the measured midrapidity ratios and assuming that the midrapidity to 4 p ratio is the same as at 10.74A GeV [15].

[98] C. Adler *et al.*, STAR Collaboration, Phys. Lett B 595, 143(2004).

[99] B.B. Back, et al., PHOBOS Collaboration, Phys. Rev. Lett. 87, 102301 (2001).

[100] A.M. Rossi, et al., Nucl. Phys. B 84, 269 (1975);

[101] J.L. Bailly, et al., NA23 Collaboration, Phys. Lett. B 195, 609 (1987).

[102] T. Alexopoulos, et al., Phys. Rev. D 48, 984 (1993).

[103] B. I. Abelev *et al.*, STAR Collaboration, Phys. Rev. Lett 103, 092301 (2009).

[104] I.C. Arsene *et al.*, BRAHMS Collaboration, Phys. Lett. B 687, 36 (2010) .

[105] I.G. Bearden, et al., BRAHMS Collaboration, Phys. Rev. Lett. 94, 162301 (2005).

[106] K. Aamodt et al., ALICE Collaboration , Eur. Phys. J. C 71, 1655 (2011).

[107] B.I. Abelev et al. (STAR Collaboration), Phys. Rev. C 79, 034909 (2009). arXiv:0808.2041.

[108] C. Alt et al. (NA49 Collaboration), Eur. Phys. J. C 45, 343 (2006).

arXiv:hep-ex/0510009.

[109] T. Anticic et al. (NA49 Collaboration), Eur. Phys. J. C 68, 1(2010). arXiv:1004.1889.

[110] T. Alexopoulos et al. (E735 Collaboration), Phys. Rev. D 48, 984 (1993).

[111] G.J. Alner et al. (UA5 Collaboration), Nucl. Phys. B 258, 505 (1985).

[112] T. Alexopoulos et al., Phys. Rev. D 46, 2773 (1992).

[113] M. Floris, ALICE collaboration, paper presented at Conference of Quark Matter 2011, Annecy, France, J. Phys. G 38, 124025 (2011).

Arabic Abstract

الملخص العربي

يعتبر المصادم الهادرونى الكبير LHC أضخم مُعجِّل جسيمات وأعلاها طاقة وسرعة على الاطلاق، حيث بدأ فى العمل فى شهر نوفمبر ٢٠٠٩. حيث يقوم هذا المصادم العملاق بتعجيل البروتونات الى طاقة ١٤ TeV او تعجيل نواة الرصاص الى 5.5 TeV لكل بيكليون بعد الوصول الى الطاقة المناسبة يسمح لها بالتصادم فى اربعة نقاط حيث يوجد بهم كواشف عملاقة لدراسة الجسيمات الناتجة من هذا التصادم و هذة الكواشف تسمى ATLAS وCMS و ALICE و LHCb .

هدف هذة الرسالة هو البحث عن فيزياء جديدة عن طريق:

1. دراسه اقصي كثافه للجسيمات المشحونه في نطاق (0.1، 0.2، and 0.5) بالنسبه الي التسارع الكاذب(rapidity and pseudorapidity). ثم مقارنة النتائج مع نتائج تجارب سابقة مهتمه بدراسة نفس الظاهرة.
2. دراسة علاقة النسبة بين (kaon/pion) و. multiplicity. و الهدف من هذة النقطة هو محاولة ربط تصادمات الهادرون مع الهادرون و تصادمات الايونات الثقيلة.

تتكون هذة الرسالة من خمس فصول الاول خاص بمقدمة نظرية عن النموذج المعيارى للجسيمات الاولية و مقدمة نظرية عن بعض التصحيحات الخاصة بدراسة كثافة الجسيمات و مقدمة عن كيفية تكوين بلازما الكواركات و الجليونات والطرق المختافة للكشف عنها. الفصل الثانى يتحدث عن المصادم الهادرونى الكبير و الكواشف الملحقة. وتناول ايضا احد اكبر الكواشف و يسمى CMS بشىء من التفصل و الكواشف الجزئية لهذا الكاشف الكبير.

اما الفصل الثالث فيحتوى على المعلومات الخاصة البيانات المستخدمة data, MC والطرق المختلفة لاختيارات التصادمات الجيدة. الفصل الرابع تناول دراسة اكبر

كثافة للجسيمات المشحونة داخل نطاق معين 0.1 و 0.2 و 0.5 وذلك بالنسبة التسارع والتسارع الكاذب . اما الفصل الخامس والاخير فيهتم بدراسة العلاقة بين النسبة بين الكايونات والنيونات الناتجة من التصادم و عدد الجسيمات المشحونة الناتجة من هذا التصادم.

دراسة انتاج الجسيمات المشحونة من تصادمات بروتون- بروتون فى المصادم الهادرونى الكبير

مقدمة من

محمد عطيه محمود محمد

للحصول علي درجة الدكتوراة في الفيزياء

الفيزياء النووية (الجسيمية)

أعضاء لجنة الإشراف العلمي :

أ.د/ محمد نبيل ياسين البكري

أستاذ الفيزياء النووية- كلية العلوم- جامعة الفيوم

د/ نجلاء راشد سيد

أستاذ الفيزياء النووية المساعد- كلية العلوم- جامعة الفيوم

د/ عمرو راضي

أستاذ الفيزياء المساعد- كلية العلوم- جامعة عين شمس

المشرف الخارجي

أ.د/ البرت دي روك

أستاذ الفيزياء الجسيميه بالمركز الاوربي للابحاث النوويه بجنيف (سيرن)- سويسرا

قسم الفيزياء

كلية العلوم

جامعة الفيوم

2012

جامعة الفيوم
كلية العلوم
قسم الفيزياء

دراسة انتاج الجسيمات المشحونة من تصادمات بروتون بروتون فى المصادم الهادرونى الكبير

رسالة مقدمة

لاستيفاء متطلبات الحصول علي درجة الدكتوراة في الفيزياء

الفيزياء النووية (الجسيمية)

من

محمد عطيه محمود محمد

المدرس المساعد بقسم الفيزياء

كلية العلوم

جامعة الفيوم

2012